

國立台灣大學理學院物理學研究所

碩士論文

Graduate Institute of Physics

College of Science

National Taiwan University

master thesis



UFFO UBAT 焦平面元件之校正與改良  
Calibration and Amelioration of UFFO UBAT  
Focal Surface Components

張硯詠

Chang, Yen-Yung

指導教授：王名儒 教授

Advisor: Wang, Min-Zu, Prof.

中華民國 103 年 4 月

April, 2014

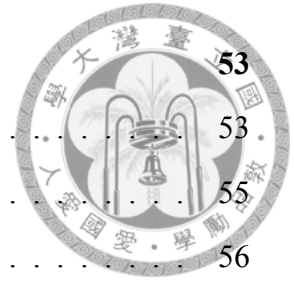


# Contents

<b>Acknowledgement</b>	<b>xi</b>
摘要	<b>xiii</b>
<b>Abstract</b>	<b>xv</b>
<b>1 GRB Physics</b>	<b>1</b>
1.1 Brief history . . . . .	1
1.2 GRB in different forms . . . . .	3
1.2.1 Prompt emission . . . . .	3
1.2.2 Afterglow . . . . .	8
1.3 Origin of GRB . . . . .	13
1.3.1 Compactness and relativicity . . . . .	13
1.3.2 Internal/External shock scenario . . . . .	15
1.3.3 Radiation mechanism of prompt emission . . . . .	18
1.3.4 Hints from the afterglow: Reverse shock, Jet and X-ray Flare . . .	22
1.3.5 Radiation mechanism of afterglow . . . . .	27
1.3.6 Progenitors . . . . .	33
1.4 Perspective physics of UFFO . . . . .	36
1.4.1 GRBs as standard candles . . . . .	37
1.4.2 Internal/External shocks unification . . . . .	40
1.4.3 Origination of Short-Hard Bursts . . . . .	41
1.4.4 Dark bursts . . . . .	42

## CONTENTS

<b>2</b>	<b>UFFO</b>	<b>53</b>
2.1	Overview . . . . .	53
2.2	Current limit of GRB observatories' responding time . . . . .	55
2.3	UBAT . . . . .	56
2.3.1	Structural design . . . . .	56
2.3.2	Readout . . . . .	58
2.4	SMT . . . . .	60
2.4.1	Slewing Mirror System (SMS) . . . . .	60
2.4.2	Richey-Chretien telescope (RCT) . . . . .	62
2.4.3	Intensified Charge-Coupled Device (ICCD) . . . . .	63
2.5	UBAT focal surface . . . . .	64
2.5.1	YSO scintillator array . . . . .	65
2.5.2	MAPMT . . . . .	66
2.5.3	Optical couplant . . . . .	68
<b>3</b>	<b>Experimental Design</b>	<b>71</b>
3.1	Preparation . . . . .	71
3.2	NuTel DAQ . . . . .	72
3.2.1	Design . . . . .	72
3.2.2	Calibration . . . . .	74
3.3	Experimental method . . . . .	75
3.4	Signal yield estimation . . . . .	77
<b>4</b>	<b>UBAT MAPMT - Hamamatsu R11265</b>	<b>81</b>
4.1	Review of conventional MAPMTs . . . . .	81
4.2	Dark current . . . . .	85
4.3	Photon counting and gain calibration . . . . .	86
<b>5</b>	<b>Calibration of UBAT FS</b>	<b>91</b>
5.1	Experimental background . . . . .	91
5.2	Energy calibration . . . . .	92



5.3	Crosstalk calibration . . . . .	94
<b>6</b>	<b>Simulation</b>	<b>99</b>
6.1	Construction of YSO scintillator array . . . . .	100
6.2	Construction of UBAT MAPMT . . . . .	104
6.3	Construction of signal recording and other components . . . . .	109
6.4	Physical process . . . . .	110
6.5	Result . . . . .	111
<b>7</b>	<b>Inverted-Conical Light Guide</b>	<b>115</b>
7.1	Motivation . . . . .	115
7.2	Review on Light Guides . . . . .	116
7.3	Test with commercial light guides . . . . .	119
7.4	Inverted-Conical Light Guide . . . . .	122
7.5	Design optimization . . . . .	124
7.6	Sample test . . . . .	128
<b>8</b>	<b>Conclusion</b>	<b>133</b>





## CONTENTS





## List of Figures

1.1	The GRB sky map of <i>BATSE</i> . . . . .	3
1.2	The distributions of the parameters of <i>Band</i> function. . . . .	4
1.3	The spectrum of GRB 911127 fitted with <i>Band</i> function. . . . .	4
1.4	$T_{90}$ and $\delta t$ of GRB prompt emissions. . . . .	5
1.5	The variable light curves of <i>BATSE</i> trigger 2228. . . . .	6
1.6	The FRED light curves of <i>BATSE</i> trigger 999. . . . .	6
1.7	The GRB hardness ratio (HR) versus $T_{90}$ . . . . .	7
1.8	The X-ray afterglow images of GRB 970228 and GRB 970303. . . . .	8
1.9	The optical afterglow images of GRB 970228. . . . .	8
1.10	The spectroscopy of GRB 980613. . . . .	9
1.11	The redshifts and the corresponding Universe ages of 260 <i>Swift</i> events. . .	9
1.12	The light curve of GRB030329. . . . .	11
1.13	The spectrum of GRB030329. . . . .	11
1.14	Selected afterglow light curves of <i>Swift-XRT</i> . . . . .	12
1.15	The general form of <i>Swift</i> afterglow light curves. . . . .	13
1.16	The illustration of the cascaded internal shocks. . . . .	15
1.17	The Monte Carlo internal shock light curves. . . . .	17
1.18	The lower-energy indices and the synchrotron Line of Death. . . . .	21
1.19	The spectral evolutions of GRB 950624 and GRB 980306 fitted with thermal emission model. . . . .	23
1.20	UV–optical light curve of GRB 130427. . . . .	24
1.21	The afterglow light curve of GRB 990510. . . . .	25

## LIST OF FIGURES

1.22	A comparison of the light curves of GRB 980329 and XRF 971019.	26
1.23	The X-ray light curves of GRB 050730 and GRB 050528.	27
1.24	The multi-bands afterglow spectrum of GRB 970508.	32
1.25	A simulation of the magnetar explosion.	35
1.26	A simulation of the NS-BH merger.	37
1.27	Categorized <i>Swift</i> - <i>UVOT</i> optical light curves.	38
1.28	An illustration of Type Ia SNe standard candles.	39
1.29	The peak luminosities of 12 <i>Swift</i> rise-type afterglows.	40
1.30	The multi-wavelength light curves of the energetic GRB 080810.	41
1.31	The collected light curve of <i>Swift</i> SHB GRB 090510.	42
1.32	Optical-X-ray flux correlations of selected <i>Swift</i> GRBs.	44
2.1	The schematics of <i>Lomonosov</i> and <i>UFFO-p</i> .	54
2.2	A statistics of <i>Swift</i> 's responding time.	56
2.3	The schematics and photos of <i>UBAT</i> .	57
2.4	An illustration to the principle of the coded mask aperture camera scheme.	58
2.5	<i>UBAT</i> readout with radioactive $\text{Am}^{241}$ .	59
2.6	The illustrations to the operation principles of <i>SMT</i> and the micro-mirror array.	61
2.7	The photos of <i>SMT</i> - <i>SMS</i> .	62
2.8	The photo of <i>SMT</i> RCT.	62
2.9	The photos and schematics of MCP.	63
2.10	The photos of the <i>UBAT</i> FS components.	64
2.11	The schematics of the YSO scintillator array.	65
2.12	The schematics of <i>UBAT</i> MAPMT.	66
2.13	Quantum Efficiency of <i>UBAT</i> MAPMT.	67
2.14	The preliminary calibration result of <i>UBAT</i> FS.	67
3.1	The one-channel layout of <i>NuTel</i> Preamp circuit.	72
3.2	The naming rule of the 64 MAPMT channels.	77



4.1	The schematics of a single channel PMT. . . . .	81
4.2	Quantum efficiencies of the commercial photocathode compounds. . . . .	82
4.3	An illustration to the dynode process and the amplification relation. . . . .	83
4.4	The gain to HV relation of MAPMTs. . . . .	84
4.5	A comparison of the signal histograms of HPD and PMT. . . . .	84
4.6	The dark current spectrum and rate map of <i>UBAT</i> MAPMT. . . . .	85
4.7	The gain calibration of <i>UBAT</i> MAPMT. . . . .	87
5.1	The YSO self scintillation spectrum. . . . .	92
5.2	The energy calibration of <i>UBAT</i> . . . . .	93
5.3	The naming rule under the collimated trigger scheme. . . . .	94
5.4	The crosstalk calibration of <i>UBAT</i> . . . . .	95
5.5	The simulated coded mask image with the crosstalk. . . . .	96
6.1	The simulation model of <i>UBAT</i> FS detection unit. . . . .	100
6.2	The YSO scintillation spectrum. . . . .	101
6.3	The reflectance of VM2000. . . . .	101
6.4	The reflectance laser profiles of VM2000 and other common reflectors. . . . .	102
6.5	An illustration to the modeling of the reflective surface. . . . .	103
6.6	The construction of the multilayer reflector. . . . .	103
6.7	The simulation snapshot of <i>UBAT</i> simulation. . . . .	105
6.8	The refractive index of Hamamatsu Bialkali. . . . .	108
6.9	The absorbance, reflectance and transmittance of <i>UBAT</i> MAPMT photo-cathode with <i>dielectric_filmMetal</i> model. . . . .	108
6.10	The transmittance of Dow-Corning Q2-3067. . . . .	110
6.11	The simulated <i>UBAT</i> crosstalk. . . . .	111
6.12	The simulated event lost rate of <i>UBAT</i> . . . . .	112
7.1	A typical deployment of the traditional light guide. . . . .	116
7.2	The scintillation lost versus the LG length. . . . .	117
7.3	The discrete scintillators and the PMT arrays. . . . .	117

## LIST OF FIGURES

7.4	The comparison of the scintillation images of continuous and discrete scintillators. . . . .	118
7.5	The schematics of the partially-reflection-partially-absorption LG. . . . .	118
7.6	The principle and the result of MLA. . . . .	120
7.7	The illustration of the concept of inverted-conical. . . . .	123
7.8	The normal-incident reflectance of polished Aluminum. . . . .	124
7.9	The cross section view of IC-LG with the parameters of optimization. . .	125
7.10	The simulated crosstalk versus the conical angle. . . . .	127
7.11	The simulated signal yield versus the thickness. . . . .	127
7.12	The schematics and the photos of the sample IC-LG. . . . .	128
7.13	The crosstalk calibration with IC-LG. . . . .	129
7.14	The simulated coded mask image with IC-LG. . . . .	130
7.15	The energy calibration with IC-LG. . . . .	130





## List of Tables

2.1	The structural specification of <i>UBAT</i> . . . . .	58
2.2	The specification of <i>UBAT</i> YSO crystal. . . . .	65
2.3	The specification of <i>UBAT</i> MAPMT. . . . .	66
5.1	The radioactive calibration sources utilized in this study. . . . .	93
6.1	The particles and physical processes enabled by the <i>UBAT</i> FS simulation. . . . .	110
7.1	The list of the mask type LG samples. . . . .	121
7.2	The list of the refractive type LG samples. . . . .	122

*LIST OF TABLES*





# ACKNOWLEDGEMENT

During the past 6 years in NTUHEP and LeCosPa, I met many respectable mentors and good friends. I have learned so much and gathered precious memories that can never be replaced.

To Prof. Wang,

You always start your comments with “I’m not sure, but is it possible.....?” When you say so, you are always right! During the past years of my apprenticeship, I’ve seen the humility and objectivity of you as a scientist. You are also a very caring teacher to all your students. Thank you.

To Prof. Ueno,

Although I didn’t really work with you in the official master-degree years. I want to tell you you inspired me to view things as an experimentalist. You taught me to analyze the problem in hand quantitatively so to get things done, in the sense of practicalness. Thank you.

To Prof. Chen, Prof. Nam and Prof. Huang,

You are so enthusiastic to students and I’ve learned so much in the Astro-particle lab. You taught me how to decompose a complicated problem, passed your experience without holding back, and helped me on my study and life. I appreciate you more than I can say.

To Prof. Shih,

You are the funnest teacher ever! working with you guarantees so much hand-on experience and laughter. Thank you.

To my friends in NTUHEP,



The memories we made together is irreplaceable. I wanted to say you all inspired me on my research, but you all know that's no comparable to all the time we wasted doing meaningless things when we were 25. I love you all, thank you.



To my family,

You are the pillars in my life and make me who I am today. You support me selflessly; you challenge my self-satisfaction; you make me brave to face life. I expect myself to be the same to you and make you all proud. I love you more than words, Thank you.

To Mom and Dad,

I hope you've found each other in Heaven now. You were the perfect parents in any respect. You always said, you didn't want us to be great men, you just wanted us to be happy. I am happy, for there's no regret living with the joy you gave us and move on. Thank you. I love you.



## 摘要

*UFFO* (Ultra-Fast Flash Observatory) 是一個由衛星搭載，以觀測 GRBs (Gamma-Ray Bursts) 為目標的探測器。拜 MEMS (Micro-Electronic-Mechanical-System) 科技所賜，*UFFO* 是史上第一個可在一分鐘內啟動可見光 (即 *afterglow*) 頻段觀測的 GRB 探測器。這可貴的早期 *afterglow* 將有助於我們推展對於 Dark Bursts、Short-Hard Bursts (SHBs) 和超新星的了解。

*UBAT* (*UFFO* Burst Alert and Trigger Telescope) 是 *UFFO* 中的 X-ray/Gamma-ray 望遠鏡，負責決定 GRB 事件的方向並交由光學望遠鏡 *SMT* (Slewing-Mirror Telescope) 做瞄準之用。由於 *UBAT* 是以 coded mask aperture camera 方法決定事件方向，編碼遮罩 (coded mask) 在焦平面上的成像品質直接決定了計算方向的精確度，以及 *SMT* 接續瞄準的成功率。*UBAT* 焦平面元件包含了 36 對的 64 通道 MAPMT 和 YSO (Yttrium Oxyorthosilicate) 閃爍體陣列的組合，稱為焦平面的觀測單元 (detection unit)。本研究的目標即是修正並改良觀測單元的性能。

在此論文中，我在第一章首先回顧了 GRB 物理，並特將與 *UFFO* 實驗相關的部分獨立於最後一節討論之。第二章介紹了 *UFFO* 實驗的硬體設計，包含整合運作與實驗計畫，以及 *UBAT* 及 *SMT* 的分項探討。在第三章中我說明了本研究的實驗設計，接著在第四章說明了各實驗儀器的性能與校正方法和結果。第五章分析了未改良前的觀測單元的校正結果，內容以其訊號強度以及成像解析度為關注焦點。根據第五章所呈現的初步結果，我建構了 *UBAT* 的蒙地卡羅電腦模擬模型。根據電腦模擬的結果，我提出了對於模糊成像的解釋。所有關於模擬的研究討論，從建構、執行到數據分析，都包含在第六章中。綜合以上，我得以提出反錐形光導 (Inverted-Conical Light Guide, ICLG) 作為可行的改良方法。我在第七章中詳細介紹了 ICLG 的發想，設計，以及電腦模擬最佳化過程。最後，我製作了一

個 ICLG 樣本並安裝於觀測單元。關於樣本的製作，以及安裝 ICLG 後觀測單元的性能都在第八章中詳細介紹。





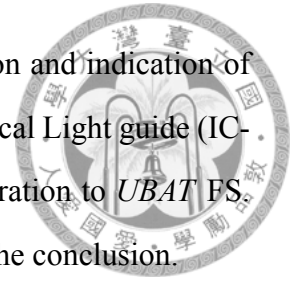
# ABSTRACT

*UFFO* (Ultra-Fast Flash Observatory) is a space-borne observatory aims to observe GRBs (Gamma-Ray Bursts) in X-ray and soft Gamma-ray. Thanks to the innovative MEMS (Micro-Electronic-Mechanical-System) technology, *UFFO* is built to be the first observatory ever capable to respond to GRBs within a minute in the optical range, i.e. afterglows. Through the observation of the sub-minute afterglows, *UFFO* will hopefully provide new perspectives to our understand toward the natures of Dark Bursts, Short-Hard Bursts (SHBs), Type-1A Supernovae, and other exciting new physics.

*UBAT* (*UFFO* Burst Alert and Trigger Telescope) is the primary telescope in *UFFO* responsible for the X-ray/ $\gamma$ -ray detection, event direction decision and the triggering of optical telescope *SMT* (Slewing-Mirror Telescope). Since *UBAT* determines the directions of GRBs in the coded mask aperture camera scheme, the coded mask image resolvability on the focal surface (FS) is crucial to the successiveness of the entire operation. The *UBAT* FS includes 36 assemblies of YSO (Yttrium Oxyorthosilicate) scintillator arrays and 64-pixels MAPMTs (Multi-Anode Photon Multiplier Tubes). The main focus of this thesis is the calibration and the amelioration of the *UBAT* FS detection assemblies.

As to begin, I give a general review on GRB physics in chapter 1 with the perspective physics of *UFFO* emphasized in the last section. The design of *UFFO* observatory is introduced in chapter 2, breaking into the *UBAT*, *SMT* sections, and a separated section dedicated to *UBAT* FS. Chapter 3 explains the experimental design and the expected result. The instrument calibration of *UBAT* MAPMT is reported in chapter 4. The calibrations of *UBAT* FS energy scale and image resolvability is elaborated in chapter 5. The result failed to match the designed performance of *UBAT*. A specialized simulation package

was then developed to further investigate the cause. The construction and indication of the simulation are discussed in chapter 6. I propose the Inverted-Conical Light guide (IC-LG) based on the simulation study in chapter 7 as a possible amelioration to *UBAT* FS. Chapter 8 summaries all the works achieved in this thesis and gives the conclusion.





## CHAPTER 1

# GRB PHYSICS

Gamma-ray bursts (GRBs) are the brightest astronomical events ever been observed by mankind. They are the Gamma-ray flashes originated in the deep Universe far from our galaxy, and have traveled for almost the whole life of Universe to Earth.

### 1.1 BRIEF HISTORY

GRBs are the  $\gamma$ -ray flashed originated in the deep Universe. They may last shortly as seconds or long as hours. The  $\gamma$ -ray photons usually arrive at Earth with energies range from 0.1 to 10 MeV, though they may also be soft as 1 keV or hard as 10 GeV.

GRBs were firstly discovered in 1960s by the U.S. *Vela* satellites. Originally the *Velas* were built to monitor USSR's orbit nuclear weapon tests. On July 2<sup>nd</sup>, 1967, *Vela III* and *Vela IV* detected the  $\gamma$ -ray signal which was later regarded as the first GRB observed in the history of mankind. Aside from its stressful connection with nuclear weapons, scientists from Los Alamos Scientific Laboratory analyzed its spectrum and direction and eventually concluded it's a new astronomical phenomenon arrived the *Vela* with a small zenith angle. Followed by more GRBs observed by *Vela IV*, *V* and *VI*, the discovery of GRBs was officialized with 16 confidential events in the paper *Observations of Gamma-Ray Bursts of Cosmic Origin* (1973) [1]. Many different theories on the origins of GRBs were proposed soon after.

The first defining spaceborne experiment, *BATSE*, was launched in 1991. With almost 3000 events collected during its nine-year mission, our understanding of the energy

## 1.1 Brief history

spectrum, temporal structure, the source distribution of the GRB  $\gamma$ -ray component, i.e. the prompt emission, as well to the origination of GRBs was largely improved.

During the mid 90s, the GRB “afterglow” was discovered in the X-ray/optical by the satellite experiment *BeppoSAX*. Since the afterglows might last for months, the GRB Co-ordinate Network (GCN) was built so many ground-based UV-radio observatories around the globe could follow up the triggers from satellites such as *BeppoSAX* and *HETE-2*, targeted to the GRB sources and kept monitoring the signals in multi-wavelength until the signals subsided. Until today, GCN is still coordinating the satellites and ground observatories. The multi-wavelength observation gave birth to the “Fireball scenario”, which people now accept as the best model of the origination of GRBs. It was also from the afterglows did scientists discover the undoubtable connection of GRBs and Supernovae around Millennium. However, limited by the designs of their optical detectors and the GCN time lag, most observations in the optical started half day after the prompt emissions.

In 2004, the *Swift* was launched. People had finally crossed the technology barrier and begun to accumulate the afterglows starting from the first minute. The fireball scenario was inspected in detail. Unprecedented data were provided toward interesting topics such as the dark bursts, the afterglows and the progenitors of Short-Hard Bursts (SHBs), the internal/external-shocks-overlapping phase. Instead of confirming the previously-known picture of GRBs, *Swift* revealed that, the nature of GRBs could be even more complicated and divert from what people had understood before. Today, the leading experiments in the field are the *Swift*(2004- ) and *Fermi*(2008- ). They both have the rapidity of optical observations a few minutes after the prompt emission triggers.

Many questions remain unanswered. Does the *Swift* observation suggest there are more classes of GRBs? What is the physics behind different GRB classes? Do GRBs exhibit universal characteristics? Is there an internal/external-shocks-overlapping phase to be observed? Can we directly determine the fireball parameters from the observation? These questions are hopefully to be put forward in the coming era with uncultivated afterglows lay in the first minute.



## 1.2 GRB IN DIFFERENT FORMS

There are two major components of a GRB: the prompt emission and the afterglow. The former indicates the  $\gamma$ -ray component which defines the GRB; the latter indicates the companion X-ray–radiowave signals follows the prompt emission. They are introduced in 1.2 from the experimental point of view, the theoretical models are discussed in 1.3.

### 1.2.1 Prompt emission

The prompt emission of a GRB indicates its major  $\gamma$ -ray emission and defines whether it is classified as a GRB event. Most of our knowledge of GRB prompt emissions was established during the *BATSE* era. There are three main properties of prompt emissions we've learned from *BATSE*: the source distribution, the hardness, and the temporal structure.

Fig. 1.1 shows the distribution of 2704 *BATSE* events. There was no repeater nor cluster found. The result indicated GRBs were transient phenomena and the sources could only be galactic or cosmological [2]. In most cases, prompt emission photons have the energies about a few hundred keV, while some events have been reported with several GeVs. In parallel to the GeV prompt emissions, there are also events with the prompt emissions in the soft  $\gamma$ -ray and X-ray. Although one might intuitively classify the X-ray components into afterglows, these events exhibit typical temporal structures of the prompt emissions. They are now classified as the X-ray Flashes (XRFs).

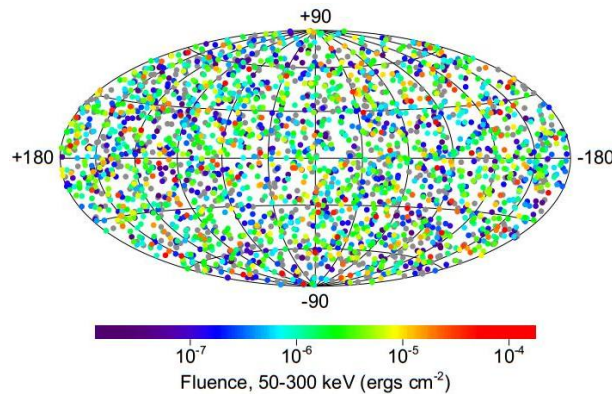


Figure 1.1: The sky map of 2704 *BATSE* events.



## 1.2 GRB in different forms

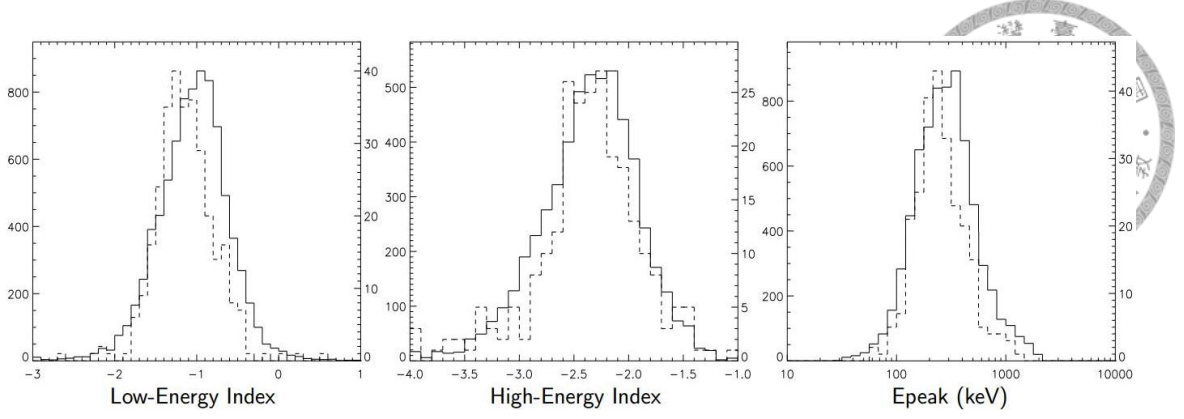


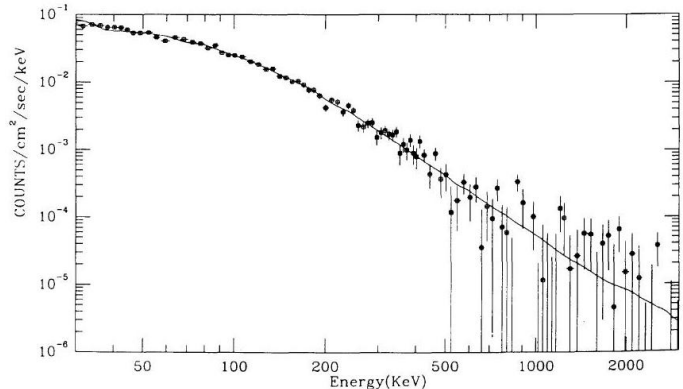
Figure 1.2: The distributions of  $\alpha$ ,  $\beta$  and the peak energy in Band function. The low energy spectra have shallower decay  $\sim -1$ , the high energy spectra have steeper decay  $\sim -2$ . The spectra break at  $\sim 300$  keV.

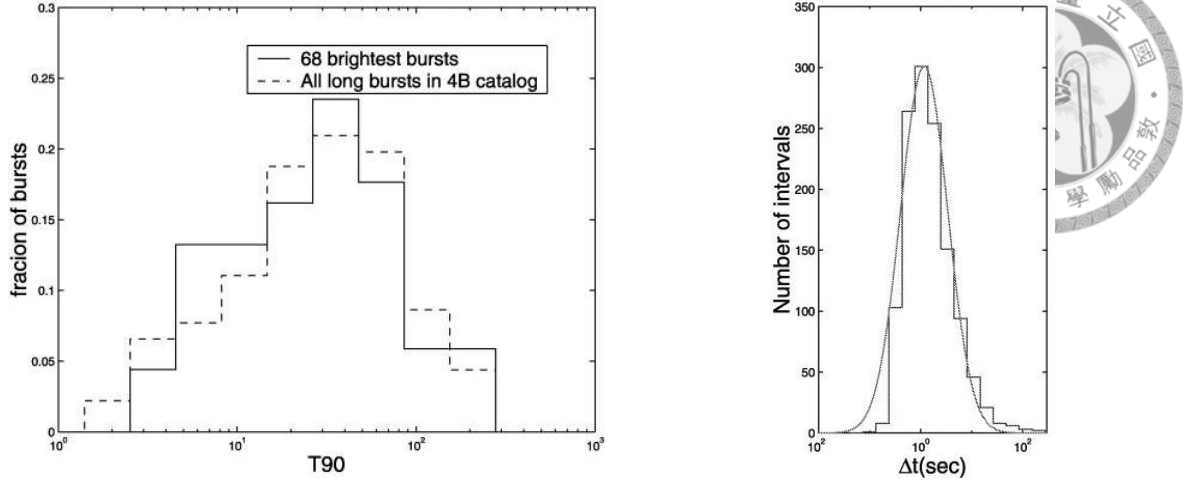
The commonly accepted description of GRB energy spectra is the so-called Band function (Eqn. 1.1), which is an empirical function firstly derived from the time-integrated energy spectra of 52 *BATSE* events [3].

$$N(\nu) = N_0 \begin{cases} (h\nu)^\alpha e^{-\frac{h\nu}{E_0}} & , h\nu \leq (\alpha - \beta)E_0 \\ (h\nu)^\beta e^{(\alpha-\beta)} [(\alpha - \beta)E_0]^{\alpha-\beta} & , h\nu > (\alpha - \beta)E_0 \end{cases} \quad (1.1)$$

Band function is also known as the power-law description. It models the spectra with two line segments of slopes  $\alpha$  and  $\beta$  in log-log plots connected smoothly by empirical terms. Fig. 1.2 shows the powers  $\alpha$ ,  $\beta$  and the peak energy [4]. It shows GRBs generally have photon energies about  $10^2$ – $10^3$  keV. Many later studies have examined the Band function with larger *BATSE* dataset, pulse spectra or other spectra outside of *BATSE*'s energy range. Band's broken power-law prescription is basically valid in all cases. Fig. 1.3 is a typical GRB spectrum fit with Band function [3].

Figure 1.3: The spectrum of *BATSE* event GRB 911127. The low-energy index is  $\alpha = -0.968 \pm 0.022$ , the high-energy index is  $\beta = -2.427 \pm 0.07$ . The spectrum breaks at  $E_0 = 149.5 \pm 2.1$ . Fitting  $\chi^2 = 121.58$  with degree of freedom 100.



Figure 1.4:  $T_{90}$  and  $\delta t$  of GRB prompt emissions.

The common measurement of GRB durations is the  $T_{90}$  (or sometimes  $T_{50}$ ), which means the time of accumulating 90% (50%)  $\gamma$ -photon counts starting from the first trigger. GRBs may have very different  $T_{90}$ s vary from  $10^{-1}$  to  $10^3$  sec. (Fig. 1.4). More than 80% GRBs exhibit the “variable” light curves<sup>1</sup>, which means the photons arrive at the detectors with highly variable fluxes. And the rest simply shows the Fast-Rise-Exponential-Decay (FRED) light curves. Examples of both kinds of the light curves are shown in Fig. 1.5 and Fig. 1.6, respectively. The variability of a GRB is defined as  $T_{90}/\delta t$ , where  $\delta t$  denotes the average width of instant fluxes, i.e. the width of the light curve peaks. It can be deduced from Fig. 1.4 the typical variabilities of GRBs may reach 1000 [6].

One of the most important discovery made by the *BATSE* was that, among almost 3000 GRBs observed by *BATSE*, there were actually two distinctive classes, the long bursts and the short bursts. Those with  $T_{90}$ s greater than 2 sec. are defined as the long bursts, and the others are defined as the short bursts. The two classes are not just distinctive in the durations, but also in the hardnesses. Fig. 1.7 explains the short-hard/long-soft relation [7]. It can be seen from the figure, the long bursts are 10–100 times longer than the short bursts and about half in hardness. Despite the difference between the two classes, most GRBs pose a general hard-to-soft trend in both the variable and FRED light curves. It can be qualitatively understood from Fig. 1.5 and Fig. 1.6, and a strict proof is provided in [8].

<sup>1</sup>energy-integrated photon count v.s. time

## 1.2 GRB in different forms

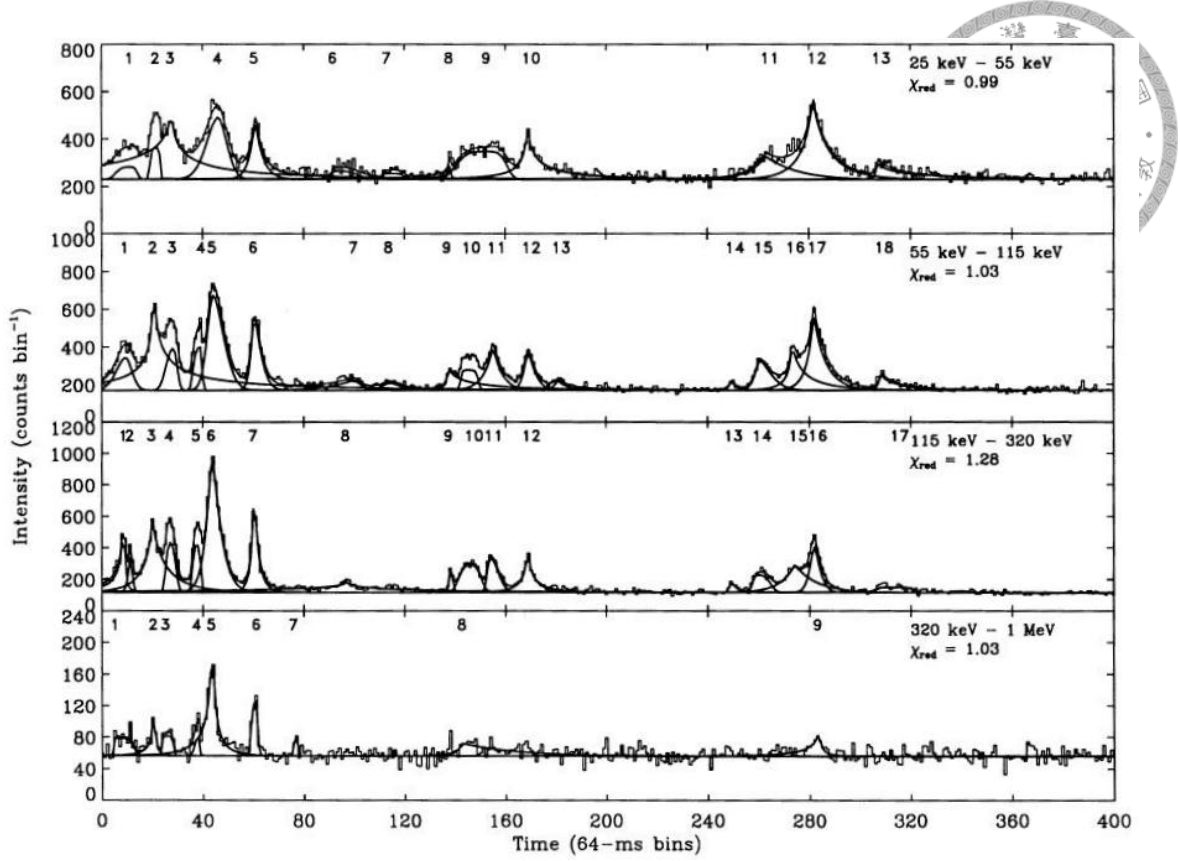


Figure 1.5: The variable light curves of *BATSE* trigger 2228. The panels shown from top to bottom are in 25–55 keV, 55–115 keV, 115–320 keV and 320–1000 keV.

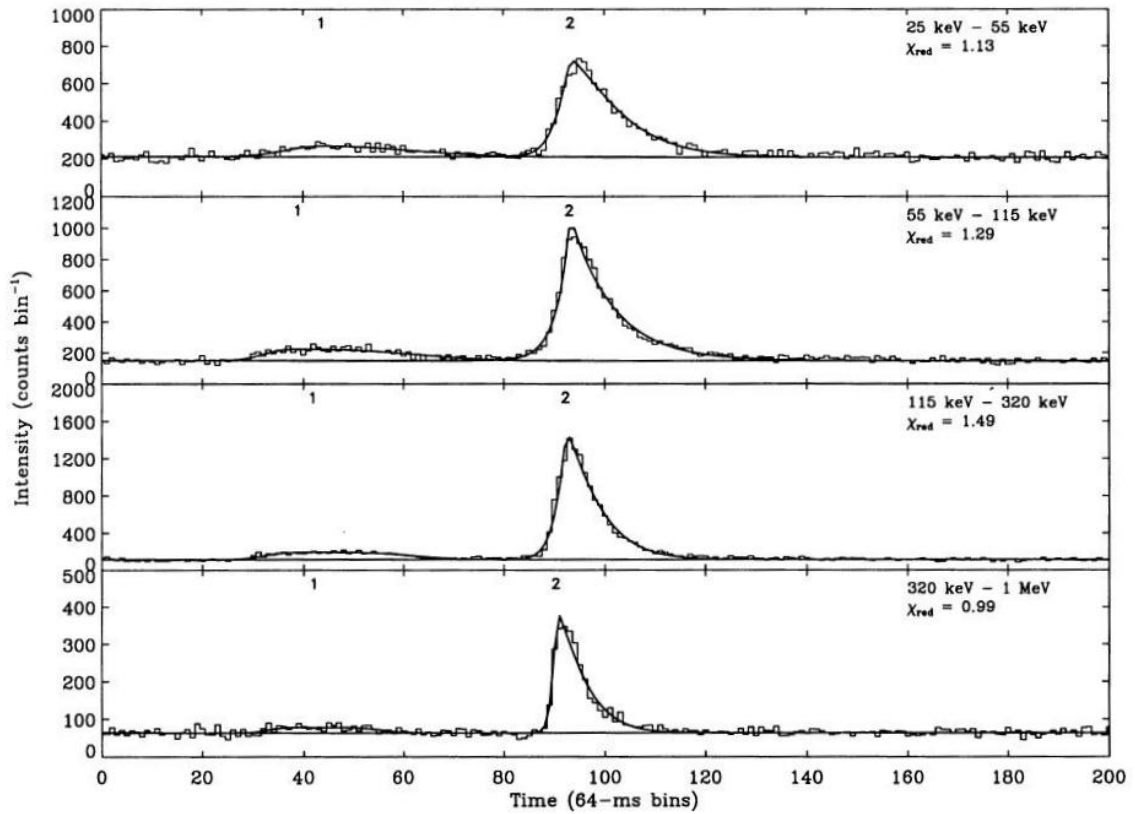


Figure 1.6: The FRED light curves of *BATSE* trigger 999. The panels shown from top to bottom are in 25–55 keV, 55–115 keV, 115–320 keV and 320–1000 keV.

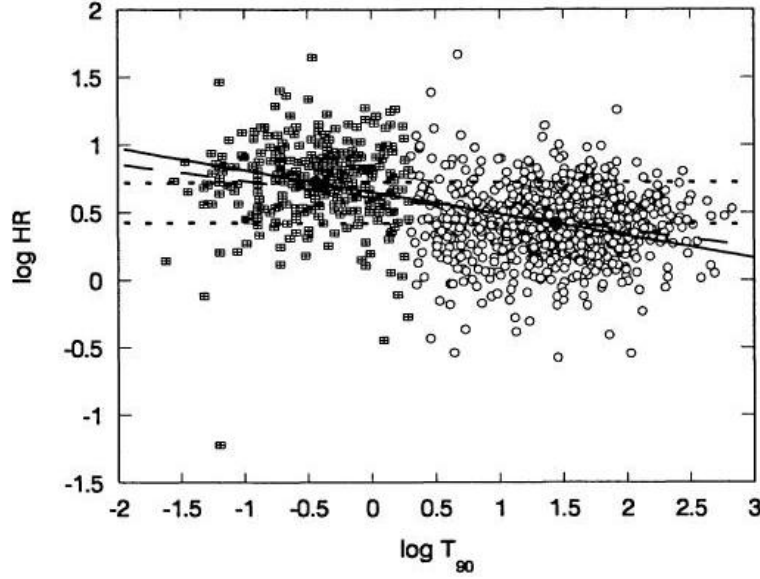


Figure 1.7: The log-log plot of hardness ratio (HR) versus  $T_{90}$ . The hardness ratio is the ratio of photon counts in 115–320 keV to which in 55–115 keV. The squares and circles represent the short and long bursts, respectively. The solid line is the regression line for all the bursts, while the dot lines are for different burst classes.

There was one famous paradox emerged from the total energy and the variability—the compactness problem [9]. It argued that, the total energy of a prompt emission emitted in the first few seconds (roughly the first variable peak) was about  $10^{51}$ – $10^{53}$  erg, if one took the variable time scale  $\delta t$  to be the “one slice” of the source material ( $\delta t \times c$ ), the energy density was so high that all the photons underwent  $e^\pm$  pair productions. It led to the conclusion that no such Gamma-ray events should had ever been seen. It was not until scientists discovered the afterglows did the paradox was solved. The compactness problem will be mentioned again in next subsection and throughly explained in 1.3.1.

## 1.2 GRB in different forms

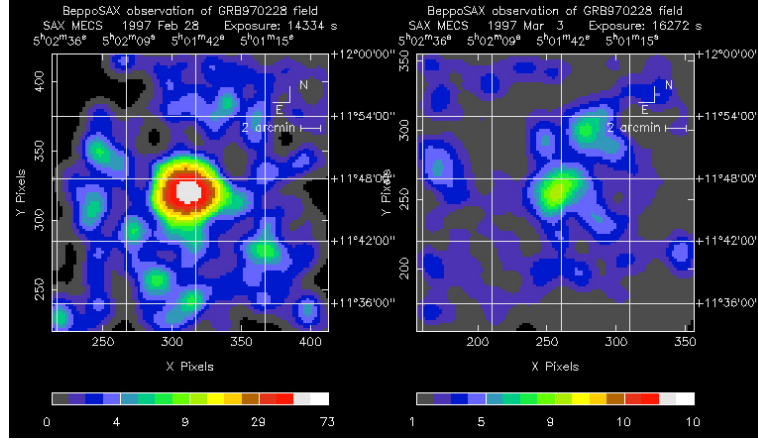


Figure 1.8: The X-ray afterglow images of GRB 970228 and GRB 970303 taken by *BeppoSAX*.

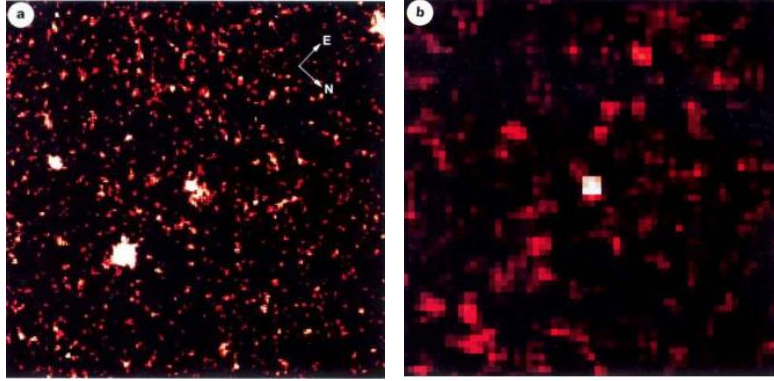


Figure 1.9: The optical afterglow images of GRB 970228 taken by *HST* on (a) Mar. 26<sup>th</sup> and (b) Apr. 7<sup>th</sup>.

### 1.2.2 Afterglow

The afterglows indicate the components of GRBs lay in the wide X-ray–microwave range. It is called because when the afterglow was firstly discovered, the signal lasted many days after its prompt emission had ended.

The hints of the afterglows were firstly seen by c from GRB 970111<sup>2</sup> and later confirmed by GRB 970228, two previously unknown 2–10 keV X-ray sources showed in the *BeppoSAX*'s error box 8 hours after the prompt emission triggers. It was soon proven by GRB 970303 the X-ray source, which was decaying quickly about 400 times/day, was indeed GRB-associated [10]. Fig. 1.8 and Fig. 1.9 show the X-ray afterglows of GRB

<sup>2</sup>The conventional naming rule of GRBs, eq. GRB 970111 means the GRB observed on Jan. 11<sup>th</sup>, 1997

970228 and GRB 970303 taken by *BeppoSAX* and the optical image of GRB 970228 taken by Hubble Space Telescope (HST) on Mar. 26<sup>th</sup> and Apr. 7<sup>th</sup>. With the help of GCN, satellite optical telescopes such as William Herschel Telescope (WHT), Issac Newton Telescope (INT) and HST could follow up the GRB triggers in about one day and subsequently found Nebulosities on the source directions [11].

With the X-ray/optical signals obtained, the spectroscopic analysis was performed the first time on GRB 970508 and later on many others (Fig. 1.10). It is now known that GRBs are extremely distant cosmological phenomena and may have (observable) redshifts high as 9, which traces back to the earliest 5% of the age of present Universe (Fig. 1.11) [12, 13].

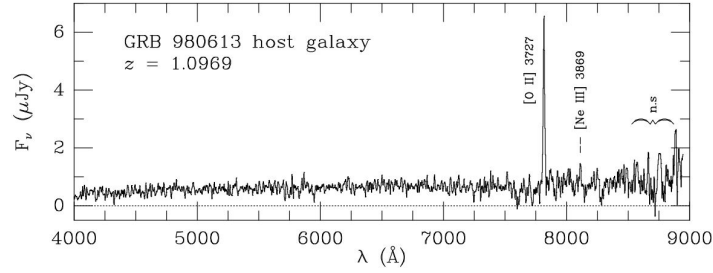


Figure 1.10: The spectroscopy of GRB 980613 produced by *Keck II* telescope in optical-IR. Clear signals of [O II] 3727 and [Ne III] 3869 were obtained. [12] points out a massive activity of star formation was identified at the forming site of GRB 980613's.

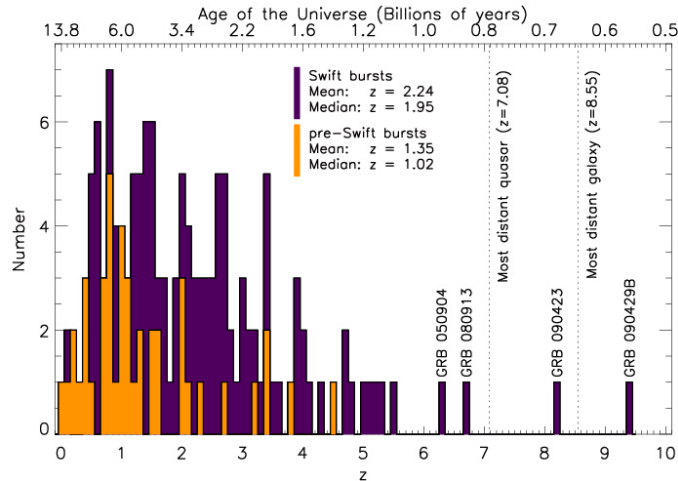


Figure 1.11: The redshifts and the corresponding Universe ages of 260 *Swift* events. Note that since it's usually challenging observing the highly red-shifted signals, distributions of redshifts may vary significantly from one experiment to another. Also the distributions don't reflect the real population of GRBs.

## 1.2 GRB in different forms

To adjust for such a gigantic energy emission in a few seconds, theories began to relate GRBs to violent star formations, e.g. supernovae, neutron star/black hole collisions...etc., around the 90s. In this case, the transiency, source compactness, and the Nebulosity could be fulfilled altogether. In 2002, Bloom et al. examined the displacements of 20 long GRBs from their corresponding Nebulosity centers with the afterglows. The study confirmed the GRBs were emitted from the centers. Further more, all the Nebulosities were either irregular or spiral, i.e. the signatures of newly born galaxies. In parallel with the displacement approach, the X-ray spectroscopy also revealed the host galaxies had typical hydrogen density of newly born galaxies [14, 15, 16, 17].

Following the triumph of *BeppoSAX*, *HETE-2* satellite was launched in Oct., 2000. It was built to be the first GRB satellite capable to process the trigger information and determine the event direction on-board. The trigger information was then transmitted to the nearest relay station on the equator and distributed through GCN. This mechanism shortened the time lag of the follow-up optical observations from half day in the *BeppoSAX* age to a few hours. The breakthrough largely boosted the field of GRB with regard to the progenitors.

Among all the discoveries made by *HETE-2*, the most dramatic event occurred on Mar. 29<sup>th</sup>, 2003. GRB 030329 was a rather close ( $z=0.167$ ) event. It was very bright and the *HETE-2* (also other GCN-follow-ups) was able to monitor the evolution of the afterglow from the first hour for many months. Fig. 1.12 and Fig. 1.13 show both the afterglow's light curve and spectrum fell from typical power-law shapes in to the identical shape of Supernova (SN) SN2003dh observed on the same day [18, 19]<sup>3</sup> Reader may see a clear SN spectrum emerged in the afterglow one month after GRB 030329. SN2003dh was later classified to be a Type Ic SN like SN1998bw, which was also a long-GRB-associated SN. GRB 030329/SN2003dh provided an indisputable first evidence that GRBs were generated by SNe.<sup>4</sup>

<sup>3</sup>People often compare this GRB/SN event with SN1998bw, for it's in fact the first SN aroused the idea of GRB-SN connection. But back that time, the proposition was regarded flawed. People new usually take GRB030329/SN2003dh to be the first direct evidence to the GRB-SN connection. Reader may find interesting stories about the discovery of GRB-SN connection in 1.3.6.

<sup>4</sup>So far only the long bursts have been observed with evidence of SNe being the progenitors. For the short bursts, none of the theoretical models is directly supported by any experimental data. However, the



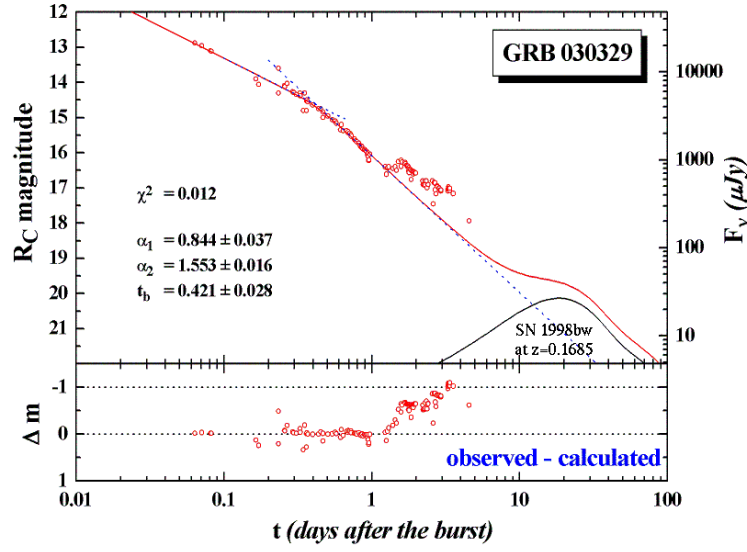


Figure 1.12: The light curve of GRB030329 fell to SN 1998bw after 10 days.

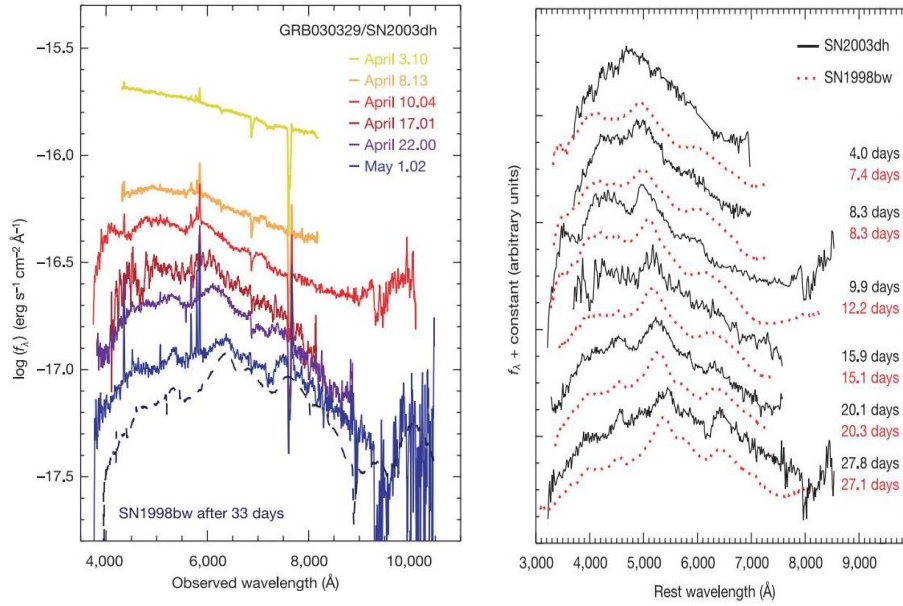


Figure 1.13: The spectrum of GRB030329 fell to SN 1998bw after a month.

As *Swift* and *Fermi* launched in 2004 and 2008, the general light curve of afterglows people understand today has been established. Fig. 1.14 and Fig. 1.15 presents the examples from *Swift* and a cartoon illustrates the features [20][21]<sup>5</sup>. The light curve can be broken down into several lower-law segments. In Fig. 1.15, following the tail of the softer prompt emission (0), the light curve starts the steep decay of index  $\sim -3$  in the first few

observations also set high limits to SN not being the progenitors of short bursts. Further reading can be found in 1.3.6.

<sup>5</sup>p. 80 and the references cited therein.



## 1.2 GRB in different forms

minutes (I). Then it enters the common power-law decay phase seen before the time of *Swift* (III). The monotonic decay poses a index  $\sim -1$ , lasts for days to months, and usually fades away. It was discovered by *HETE-2* sometimes intermittent X-ray flares<sup>6</sup> occur during the early time of phase III (V). *Swift* found that about 1/3 of its events show the plateau before entering the common decay (II). The plateau, if seen, usually persists a few hours with index  $\sim -0.5$  as a prolonged luminous. In some rather clear and bright events, instead of decaying into a undetectable dimness, a clear turning might appear at about 1 day into phase III. The turning is called the “jet break” (IV), which is now regarded as the evidence of the collimation of GRB SN outflows. The jet-break events consist  $\sim 10\%$  of the *Swift* events.

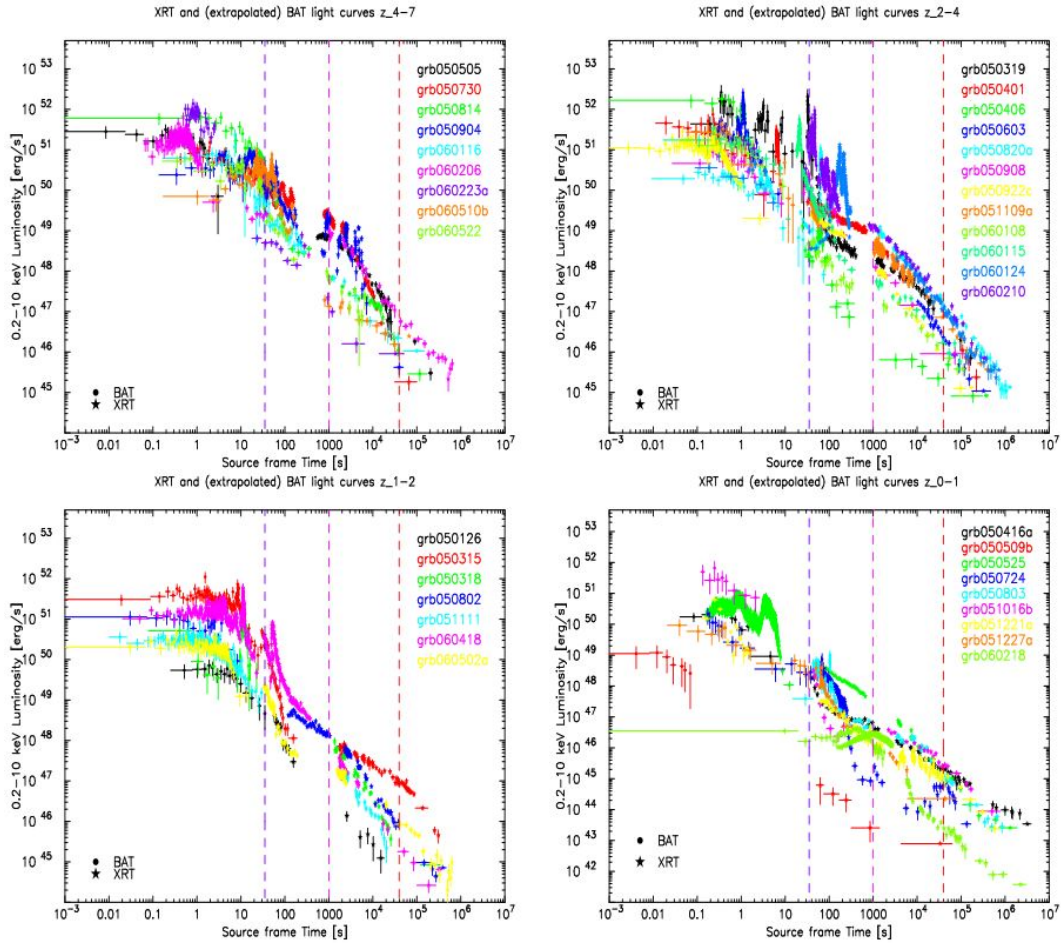


Figure 1.14: 37 selected afterglow light curves of *Swift-XRT*. The light curves are classified by  $z = 4-7, 2-4, 1-2, 0-1$ , arranged top-left, top-right, bottom-left, bottom-right, reflectively.

<sup>6</sup>Sudden high flux of X-ray. More discussion is provided in 1.3.4

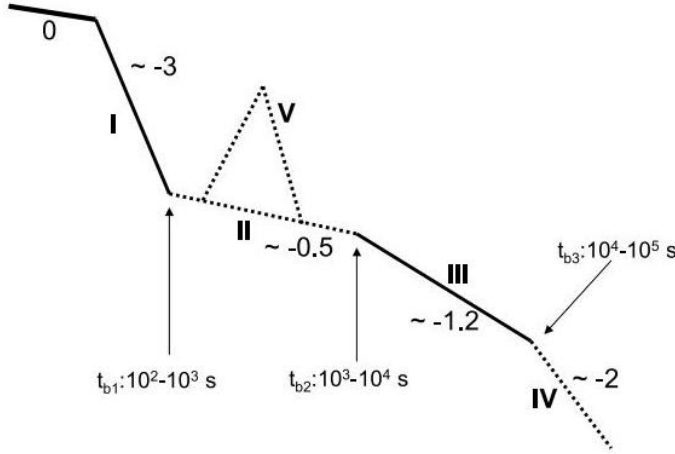


Figure 1.15: A general form of afterglow light curves includes all the features observed so far. It is plotted in the log-log scale, with the vertical and horizontal axes being the luminosity and the time after trigger, respectively.

### 1.3 ORIGIN OF GRB

The origin of GRBs is now understood as the Fireball scenario. It was firstly proposed by Rees et al. in 1992 based on the observation of the prompt emission [22], and later modified in intricate details to adjust for the clues given by the afterglow.

In the following section, I first introduce the oldest topic in the theory of GRB—the compactness and relativicity. It is the central idea that holds the original fireball model. The major mechanism allows the duality of prompt emission-afterglow, the Internal/External shock scenario, is then discussed in 1.3.2. In 1.3.3, the possible dynamics gives rise to the radiation of the prompt emission is reviewed. Then I turn to the afterglow, with the theoretical implications from the observations of the afterglow enumerated in 1.3.4 and discuss the possible radiation dynamics in 1.3.5. All the effort finally condenses to the modeling of GRB progenitors in 1.3.6.

#### 1.3.1 Compactness and relativicity

As discussed in the end of 1.2.1, one of the famous question arose from the prompt emission was the compactness problem. It can be understood conceptually as follow:

GRB shows a non-thermal, i.e. non-blackbody, spectrum with a significant portion in the high energy. It implies the radiation must be observed directly from the primary emission mechanism, not from the consecutive thermal equilibrium or any collective phenom-

### 1.3 Origin of GRB

ena, e.q. scattering. The active duration of the emission can be set by the variable time  $\delta t$ , so the size of the active region is limited by  $c \times \delta t$ . A simple example pictures a this . spheric shell of thickness  $\sim c\delta t$ , a galactic distance  $D$  from Earth, the observed flux  $F$ , the typical GRB photon energy  $E_\gamma$ ; the photon density  $n_\gamma$  in the active region is estimated by

$$n_\gamma \approx \frac{4\pi D^2 \times F \delta t}{(c\delta t)^3 \times E_\gamma} \quad (1.2)$$

. Considering the Gamma photons undertake  $\gamma\gamma \rightarrow e^+e^-$  productions, the optical depth  $\tau_{ee}$ <sup>7</sup> is roughly

$$\tau_{ee} \approx \sigma_{ee} \times c\delta t \times n_{gamma} \approx 10^{15} \quad (1.3)$$

, where  $\sigma_{ee}$  is the pair production cross-section<sup>8</sup>. In other word, the spectrum should have been a massively-scattered thermal spectrum.

The fireball model solves this paradox by stating that the active region is actually highly relativistic with respect to the Earth frame. The Lorentz factor  $\Gamma$  replaces  $E_\gamma$ ,  $c\delta t$  and  $F$  with  $\frac{E_\gamma}{\Gamma}$ ,  $\Gamma^2 c\delta t$  and  $\frac{F}{\Gamma}$ , respectively. The relativicity gives an overall  $\Gamma^6$  reduction to the optical depth. So to acquire a reasonable optical depth less than unity, i.e.

$$\Gamma^6 \gtrsim 10^{15} \quad , \quad \Gamma \gtrsim 300 \quad (1.4)$$

With more and more GRBs observed with accurate redshifts and very high MeV/GeV energies, some lower limits of  $\Gamma$ 's can be set. [24] presents a sophisticated calculation based on the idea of compactness and argues that some strong *Fermi* events have  $\Gamma$ 's over 1000.

The result of compactness was later supported by the observation of afterglows, which is another impressive approach to GRB relativicity. Although it is now known GRB poses a optical-thin spectrum because the emitting jets are highly relativistic, recent studies suggest the thermal evolution of the central engine may be determined from the spectrum of early afterglow. The physics of the afterglow is in 1.3.4 and 1.3.5.

---

<sup>7</sup> $\frac{I(x)}{I_0} = e^{\frac{-x}{x_0}}$ ,  $\tau \equiv -\ln(\frac{I(x)}{I_0}) = \frac{x}{x_0}$

<sup>8</sup>Sophisticate derivations involve QED cross-section calculation considering the distribution of the photon energy can be found in [23]

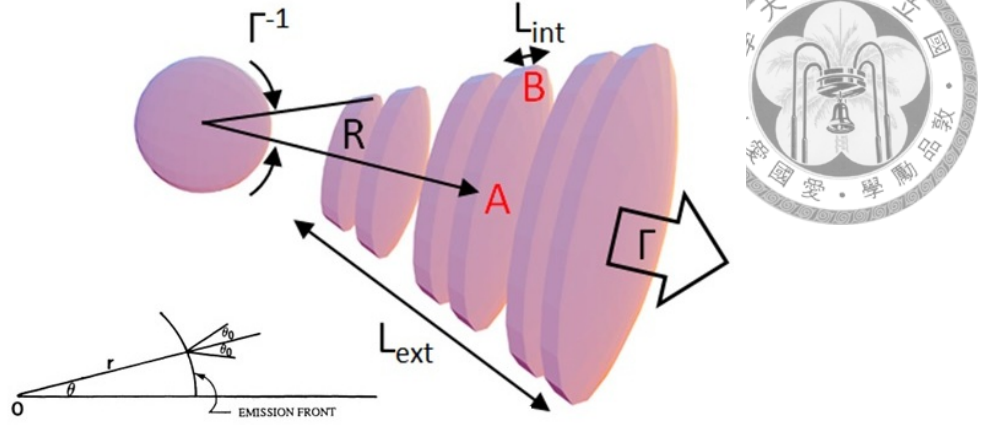


Figure 1.16: An cartoon illustrates the cascaded internal shocks.

### 1.3.2 Internal/External shock scenario

The prompt emission and the afterglow are very distinct in nature. The prompt emissions are highly variable, short in durations, and pose obvious strong-to-soft transitions; while the afterglows decay smoothly, last for months, and exhibit achromatic spectral decays<sup>9</sup>, i.e. decay evenly in all wavelengths.

It can be induced from the prompt emission's variability the active region(s) is likely to be cascaded. In fact, it was proven rigorously a continuous outflow thrust into the interstellar medium (ISM) analogous to the SN remnant ejecta could only produce a continuous light curve but the variable structure [25, 26] (see the next paragraph). To cope with the prompt emission-afterglow duality, the Internal/External shock model proposes GRBs are generated by SNe under special conditions. Analogous to other SNe, the magnificent explosions make ejecta that thrust into ISM. The ejecta are named the external shocks. As the external shock continuously plows into ISM particles, it generates the afterglow. It's then straightforward to have a continuously and achromatically decreasing light curve from the continuous expansion and cooling. The Internal/External shock model states that, what was distinct from the non-GRB-progenitor-SNe is the GRB ejecta must be much more energetic than the normal SN ejecta, so the Lorentz factor may be high as  $10^{2-3}$ . The ejecta is so violent that the it bursts out at the speed much faster than the speed of the sound

<sup>9</sup>except a peculiar class of GRBs called the dark bursts. The dark bursts is discussed in 1.4.4.

### 1.3 Origin of GRB

and generates the cascaded shock waves inside the ejecta. It is when these shock waves are generated the Gamma photons burst out and produce the variable light curves of the prompt emissions. The shock waves inside the ejecta are named the internal shocks.

Fig. 1.16 illustrates the Internal/External shocks scenario [26, 28]. Since the ejecta moves much faster than the speed of sound, each layer of the outflow is treated to have its own speed. The bulk and local Lorentz factors are denoted by  $\Gamma$  and  $\gamma$ , respectively. The GRB emission (shock wave) starts when a faster layer catches up a slower layer from behind. I denote the thickness of the active region, i.e. the faster layer, by  $L$ , the position by  $R$ . The active time viewing along the radial direction is

$$T_{radi} \cong \frac{L}{\gamma^2 c} \quad (1.5)$$

Assuming the central engine creates a spherical burst in the ejecta's inertia frame, the outflow is seen concentrated to an angle  $\theta \sim \Gamma^{-1}$  in the Earth frame<sup>10</sup>. The spherical emissions generated by the shock wave along the emission front are also seen concentrated to  $\theta_0 \sim \gamma^{-1}$ . Seeing along the radial direction, the photon from the center of the ejecta cone arrives earlier than which from the edge (the center and the edge of the disc in Fig. 1.16) due to its shorter light path. The angular time lag is

$$T_{ang} \cong \frac{R\theta^2}{c} = \frac{R}{\Gamma^2 c} \quad (1.6)$$

If the composition of the active region (the disc) changes smoothly and continuously, each pulse generated by the shock wave must be smoothened by the minimal time scale  $T_{ang}$  as viewing from Earth.

Apply this observability argument to the Internal/External shock scenario, one finds the observation of afterglows is easily satisfied by the ejecta-ISM interaction, i.e. the external shock, while the variable prompt emissions can only be produced by the constantly catching-ups shock waves in the internal shocks. In the case of the external shocks, the

<sup>10</sup>Hereafter, if not mentioned, all the calculation is done in Earth frame.

ejecta plows into the ISM as a whole, so  $L \sim R$ ,  $\gamma \sim \Gamma$ , and gives

$$T_{radi} \sim T_{ang} \quad (\text{afterglow}) \quad (1.7)$$

The result is nothing but the smooth light curves as seen from the afterglows. On the contrary, the prompt-emission variability requires

$$\begin{cases} T_{radi} \ll T_{ang} \approx \delta t \\ T_{90} \approx \text{time of central engine operation} \end{cases} \quad (\text{prompt emission}) \quad (1.8)$$

Fig. 1.17 shows an example of Monte Carlo simulation of the internal shocks producing variable light curves based on the relativistic flow dynamics. The result implies that the evolution of the light curve is seen only when  $L \leq T_{ang}c$ , and the high variability is achieved by large  $\gamma$  fluctuation. Though it demonstrates the “realistic” light curves may be reproduced with proper combinations of parameters, limited by the current computational ability, it’s still impossible to deduce the real conditions from the observed data [27].

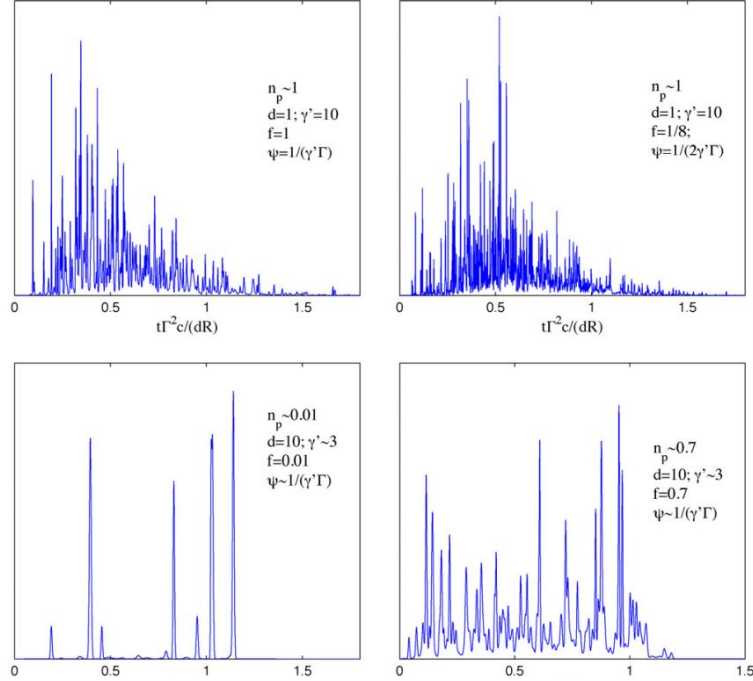


Figure 1.17: The Monte Carlo simulations of the internal-shock-generated variable light curves.  $d = \frac{L}{R/\Gamma^2}$  is the ratio of the thickness to  $T_{ang}c$ .  $n_p$  is the time of the “catching-ups” in  $\delta t$ . The time is scaled by  $T_{radi}$  for better comparison.

### 1.3.3 Radiation mechanism of prompt emission

At present, no consensus on the radiation mechanism of GRB is reached yet. Some possible candidates are discussed in this section. Some of them only explain the observation partially, and most of them are just lacking of complete data supporting due to the incompatibilities of experiments.



### Synchrotron radiation

Synchrotron radiation was the firstly-proposed, and until now, the most intuitive candidate of both the prompt emission and the afterglow. It arises when a charged current moves in an magnetic field either external or self-produced. In order for the radiation to be observed, the current is usually highly relativistic. In the modeling of GRB spectra, there are two important parameters to be considered: the minimal energy and the hydrodynamic cooling energy of the charge particles in the current. Usually people take electrons as being most lightest free particle in this energy regime. The derivation introduced in this subsection follows [21]<sup>11</sup>[29].

The typical synchrotron photon energy is given by:

$$(h\nu_{syn})_{obs} = \frac{\hbar q_e B}{m_e c} \gamma_e^2 \Gamma \quad (1.9)$$

, which depends on the magnetic field strength  $B$ , local (the electron's) Lorentz factor  $\gamma_e$  and is boosted into the Earth frame by  $\Gamma$ . The radiation power in the local frame is:

$$P_{syn} = \frac{4}{3} \sigma_T c U_B \gamma_e^2 \quad (1.10)$$

, where  $U_B = B^2/8\pi$  is magnetic field energy density and  $\sigma_T$  is the Thomson cross-section. Since the electron carries the energy  $\gamma_e m_e c^2$ , it's radiation-cooling time scale

$$(t_{syn}(\gamma_e))_{obs} = \frac{\gamma_e m_e c^2}{P \Gamma} = \frac{3 m_e c}{4 \sigma_T U_B \gamma_e \Gamma} \quad (1.11)$$

---

<sup>11</sup>p. 137–146

Note that it is boosted in to the Earth frame. Combining Eqn. 1.9 and Eqn. 1.11,

$$(t_{syn}(\nu))_{obs} = \frac{3}{\sigma_T} \sqrt{\frac{2\pi cm_e q_e}{B^3 \Gamma}} \nu^{-1/2} \quad (1.12)$$



This result implies the spectrum of radiation-cooled electron should obey

$$F(\nu)_{syn} \propto (t_{syn}(\nu))_{obs} \propto \nu^{-1/2} \quad (1.13)$$

For the low energy electrons, one consider the instantaneous synchrotron radiation because it's unlikely they are cooled at the finite-long radiation-cooling time scale and being observed as an accumulated photon flux. The instantaneous spectrum follows

$$F(\nu)_{inst} \propto \nu^{1/3} \quad (1.14)$$

up to where the radiation-cooling is valid, i.e.  $\nu(\gamma_{syn})$ . Note that in practice, the index 1/3 should be regarded as the upper limit of the low-energy index because its derived from the pure instantaneous situation. It approaches  $-1/2$  when the energy raises [30]. Since the typical Lorentz factor distribution is governed by  $N(\gamma_e) \sim \gamma_e^{-p}$ , where  $p$  is proportional to the radiation power, one usually considers the minimal (non-instantaneously-emitting) local Lorentz factor as the typical synchrotron Lorentz factor, i.e.  $\nu_m \equiv \nu_{syn}(\gamma_{e,min})$ .  $\nu_m$  separates the instantaneous and the synchrotron radiation-cooling regimes [31].

The upper cutoff, on the other hand, yields the maximal energy for synchrotron emission. The “too” energetic electron is cooled rapidly ( $t \propto P^{-1}$ ) and can be approximated by emitting all its energy  $\gamma_e m_e c^2$  at its synchrotron frequency  $\nu_{syn} \propto \gamma_e^2$ . Providing  $N(\gamma_e) \sim \gamma_e^{-p}$ , the electron exceeds the maximal energy threshold poses

$$F(\nu)_{hyd} \propto \gamma^{-p} \propto \nu^{-p/2} \quad (1.15)$$

The parameter divides the slow (synchrotron) cooling and the fast cooling is set by the current's hydrodynamic time scale  $t_{hyd}$  which depends on its composition. Substituting



### 1.3 Origin of GRB

$t_{hyd}$  in to Eqn. 1.11 yields the cooling Lorentz factor

$$\gamma_{e,c} = \frac{3m_e c}{4\sigma_T U_B \Gamma t_{hyd}} \quad (1.16)$$



The spectral parameters are then derived from the typical and cooling Lorentz factors. The typical synchrotron and hydrodynamic cooling frequencies are defined by

$$\begin{aligned} \nu_m &\equiv \nu_{syn}(\gamma_{e,min}) \\ \nu_{e,c} &\equiv \nu_{syn}(\gamma_{e,c}) \end{aligned} \quad (1.17)$$

It is pointed out in [29], if the ejecta flows in the fast cooling regime, i.e.  $\nu_m > \nu_c$ , the current may radiate efficiently in  $\gamma$ -ray. So to sum up, the spectrum considering solely the current behavior is in the form of broken power-law: (the single particle modification is also noted by  $\rightarrow$ )

$$F(\nu) \propto F_{\nu,max} \times \begin{cases} \left(\frac{\nu}{\nu_c}\right)^{\frac{1}{3} \rightarrow \frac{-2}{3}} & , \nu < \nu_c \\ \left(\frac{\nu}{\nu_c}\right)^{\frac{-1}{2}} & , \nu_c < \nu < \nu_m \\ \left(\frac{\nu_m}{\nu_c}\right)^{\frac{-1}{2}} \left(\frac{\nu}{\nu_m}\right)^{\frac{-p}{2}} & , \nu_m < \nu \end{cases} \quad (1.18)$$

The equation is normalized in respect of  $F_{\nu,max} = F(\nu_c)$ . The model provides a satisfiable description in  $\nu > \nu_c$  fast cooling regime for its simply a rearrangement of the Band function (Eqn. 1.1).

Synchrotron radiation encounters its major difficulty in the low energy, namely  $\nu < \nu_c$ . The index  $\leq 1/3$  is obviously in disagreement with the data [32]. Fig. 1.18 (also see Fig. 1.2) presents the Band fit low-energy indices  $\alpha$ s of 137 *BATSE* events which scatter in  $-3/2$ – $-1$ . The issue is even serious when [33, 34] point out the low energy particles should behave more like isolated particles in the current instead of a bulk flow. In the single particle picture, the optical depth grows when the energy rises, so the observable radiation is reduced as  $\nu$  approaches  $\nu_c$ . As a consequence, the modification lowers the low-energy index from  $1/3$  to  $-2/3$ .  $-2/3$  is called the “Synchrotron Line of Death” which rejects 30%–50% *BATSE* events with  $\alpha > -2/3$ . The  $-3/2$  line in Fig. 1.18 is

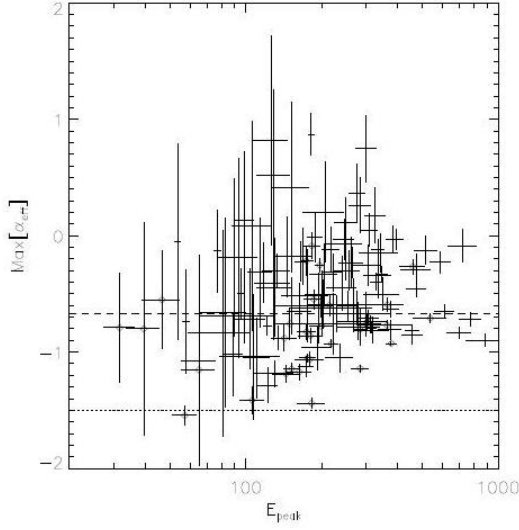


Figure 1.18: The lower-energy index  $\alpha$  to  $E_{\text{peak}}$  plot of 137 *BATSE* events. It shows  $\alpha$ s are roughly proportional to  $\log E_{\text{peak}}$ s and are mostly in the range  $-3/2$ – $1$ . The dashed line is the “Synchrotron Line of Death” which bounds the synchrotron-acceptable region below  $-2/3$ . The dotted line bounds the cooling-acceptable region above  $-2$ . There are 60 events above the line of death and 1 event below the cooling-acceptable line.

the lower limit of the fast-cooling regime considering the cooling inhomogeneity [29]. Together they confined the synchrotron allowable region

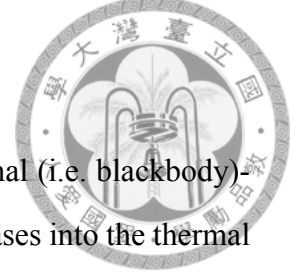
$$\frac{-3}{2} < \alpha < \frac{-2}{3} \quad (\text{synchrotron radiation}) \quad (1.19)$$

which contradicts more than 50% *BATSE* observation.

## Inverse Compton scattering

One possible remedy to the Line of Death issue is the Inverse Compton (IC) scattering [35]. It naturally occurs in the internal shocks since the electrons are so energetic in the outflows. [36, 37] derive the spectrum analytically and state the result may steeper the synchrotron model in the low energy as soft photons being struck into the undetectable GeV–TeV region.

While the modification allows the larger  $\alpha$ s and fits to the data flexibly in the low energy, it confronts the “energy crisis” in the high energy. The *EGERT* (Energetic Gamma-Ray Experiment Telescope) and *Fermi* satellites have the abilities to observe GeV GRBs and were able to set the energy upper limits to the GRB prompt emission. It turned out the simple IC model elevated 10 times more the soft photons into the GeV region than what was observed by *EGERT* and *Fermi* [38].



## Photospheric thermal emission

Another perspective toward the low-energy emission is the thermal (i.e. blackbody)-emission. [39] proposes the amount of energy the central engine releases into the thermal component may be comparable or even larger than which into the internal shock. While models focus on the optically-thin characteristic of the internal shock emission, the paper suggests a thermal component directly come from the photosphere should be observed in parallel. It should be rather bright and dominates the synchrotron radiation in the first few seconds. It's been demonstrated in some cases, the thermal emissions existed with high dominances in the first 10 sec., and the model can reasonably determines the temperature evolutions of the photospheres (Fig. 1.19) [40, 41, 42].

### 1.3.4 Hints from the afterglow: Reverse shock, Jet and X-ray Flare

#### Reverse shock

As stated in 1.3.2, the shock scenario is analogous to SN but at much higher relativicity. It is then, according to the flow dynamics, one expects the forward shocks and the reverse shocks take place simultaneously once the SN explosions occur [43]. The forward shock is which I introduce in 1.3.2. Because the reverse shock is in principle less energetic than the forward shock, due the the Lorentz boost, it is predicted to be observed in the soft X-ray to optical shortly after the tailing of the prompt emission.

The distinctive difference between the reverse shock and the external shock-ISM interaction is the reverse shock is basically the product within the intense relativistic flow. Unlike the external shock is cooled slowly by colliding into the dilute ISM, the reverse shock cools rapidly. The cooling timescale is set by  $\Gamma^{-2}$  similar to the forward shock in 1.3.2. But since it has a smaller  $\Gamma$ , it may lasts  $\sim 10^{2-3}$  seconds longer than the forward-shock-produced prompt emission and be observed. Theories predict the reverse shocks to generate fast decaying light curves of index  $-2 \sim -3$  due to it's fast cooling<sup>12</sup>. The obser-

<sup>12</sup>It's  $-2$  in a stationary region and may be close to  $-3$  in a winded/moving region. Since the shock is in the middle of the violent flow, the index is more likely to be  $-3$  but not  $-3$ .

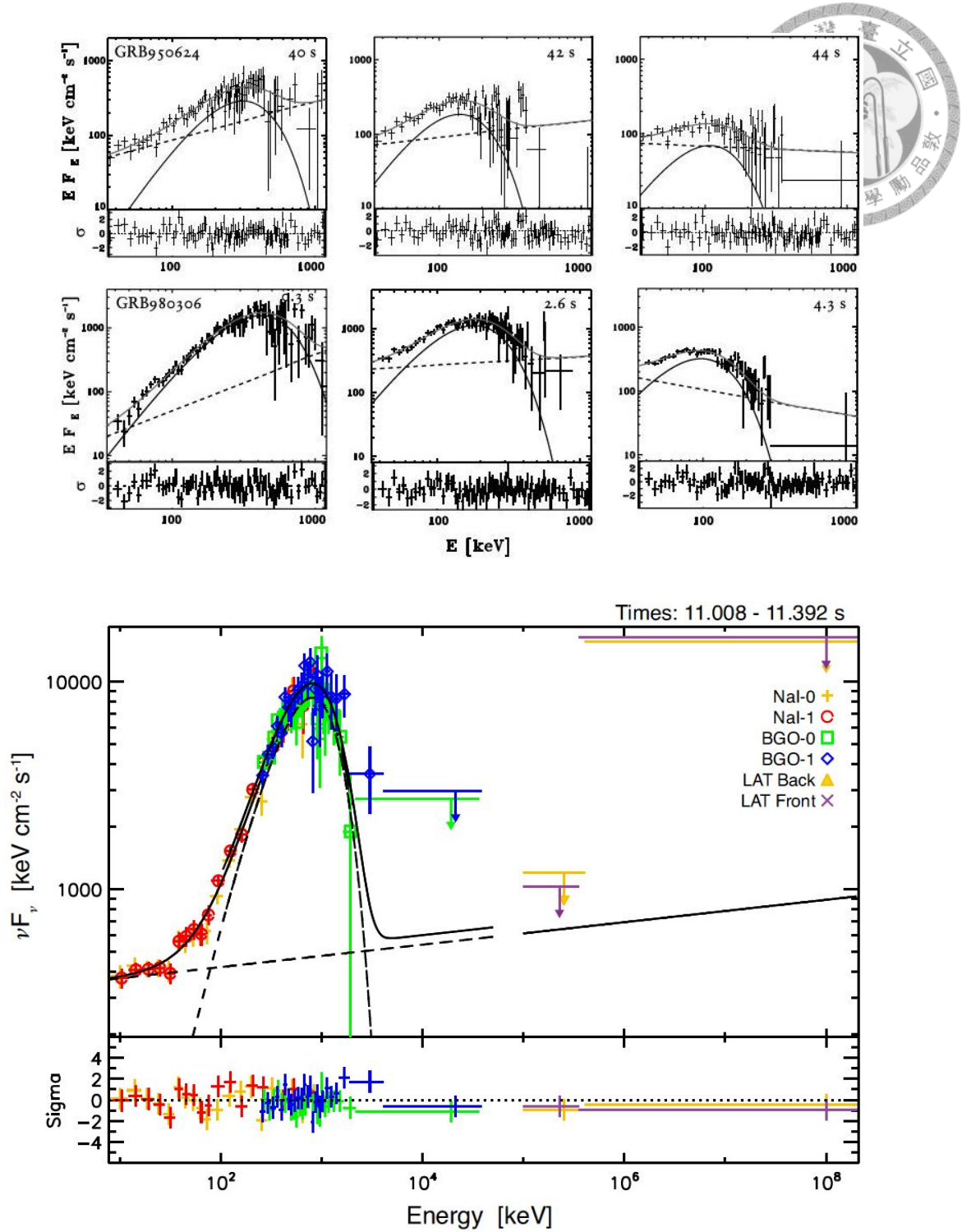


Figure 1.19: The model used in the figure is the thermal-plus-synchrotron model. The dotted lines are the power-law components, the solid lines are the thermal emissions. Plots show only the low energy parts. The upper panel shows the light curve evolutions of GRB 950624 and GRB 980306 in the first 5 sec taken by textitBATSE. Note that GRB 950624 started at 39.8 s. The lower panel shows the indisputable evidence of the thermal emission of GRB 090902B taken by *Fermi* at 11 sec.

### 1.3 Origin of GRB

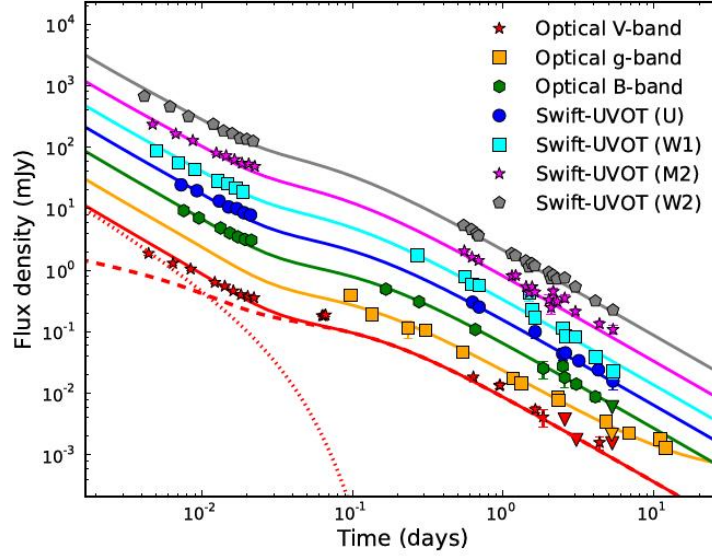


Figure 1.20: UV-optical light curve of GRB 130427 taken by *Swift*-UVOT and other ground-based observatories. The dotted line and the dashed line represent the reverse shock and the forward shock components, respectively.

variations of the reverse shocks in the beginnings of afterglows were reported in the events such as GRB 990123, GRB 021211 and GRB 060111 [44, 45, 46]. Fig. 1.20 presents the evidence of the reverse shock in *Swift* GRB 130427. The fast decay of index  $-3$  is clearly identified in the first 10 minutes [47].

## Jet

The collimated outflow picture was firstly proposed to solve the total energy problem [48]. It was known the total energy that SN converted into photo-emission was  $10^{51-53}$  erg. If one assumed the isotropic emission, GRB 9712124, at a redshift  $z = 3.42$ , was estimated to emit  $\sim 3 \times 10^{53}$  erg in its prompt emission alone [49]. Later GRB 990123 was estimated to have more than  $10^{54}$  erg [50]. If the outflow is collimated by an angle  $\theta$ , the energy budget is decreased by  $\sim \theta^2$ . One can easily estimate the collimated angle  $\theta \sim 10^\circ$ , about one order of magnitude (OM) larger than the relativistic collimation  $\Gamma^{-1}$ . In this case, the opening angle should be  $\Gamma^{-1}$  when the jet is in the relativistic regime and  $\sim \theta$  when it cools to sub-relativistic. A significant drop in flux, called the “jet break”, must be observed in the form of a turning “knee” in the light curve when the jet turns

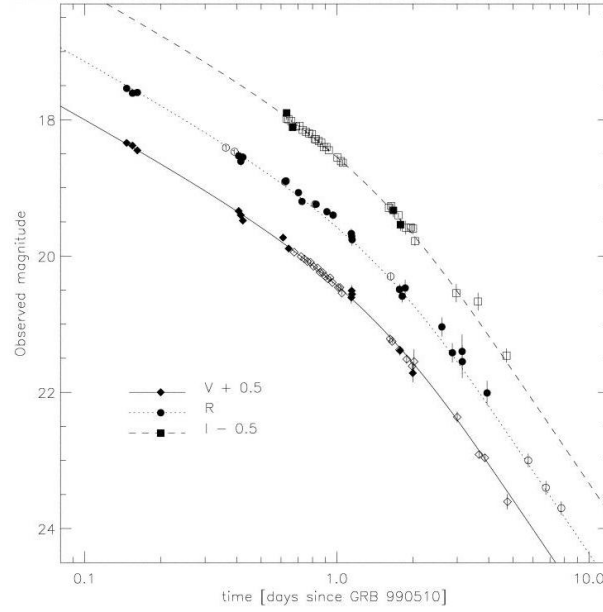


Figure 1.21: The afterglow light curves of the bright *BeppoSAX* event GRB 990510. The clear jet break appears equally in optical (diamond), IR (cube) and radio (circle) about one day after the prompt trigger. The solid and hollow symbols mark the data of *BeppoSAX* and *OGLE*, respectively.

from relativistic to sub-relativistic.

The jet break should be achromatic since it's nothing but a change in the opening angle. The ratio of the relativistic collimation and the jet angle, namely  $\Gamma^{-1}/\theta$  can also be deduced from the change of flux. As long as the Lorentz factor is given, e.g. through the compactness approach, the jet angle can be determined. Fig. 1.21 shows the first observation of the jet break in multiple bands one day after GRB 990510. The jet break is an evidence of the relativity and the jet collimation of GRB [51].

Fig. 1.22 presents a comparison of a normal GRB and an X-ray flash (XRF)<sup>13</sup> [21]<sup>14</sup>. Although exhibiting the similar characteristics of GRBs, XRFs are like “GRBs without the Gamma-ray”. So far the best explanation is XRFs are the off-axis GRBs. When Earth is not on (but somewhat close) the axes of collimation, this kind of events are not detectable until they cool down to X-ray and widen the collimated angles. The off-axis scenario is

<sup>13</sup>Reader should be careful not to confound the X-ray flashes and the X-ray flares. An X-ray *Flash* indicates the event which exhibits prompt-emission-like characteristics in X-ray; an X-ray *Flare* indicates the intermediate strong X-ray emission during the afterglow phase. An X-ray flare has a definite corresponding GRB but an X-ray flash doesn't.

<sup>14</sup>p. 55 and the references cited therein.

### 1.3 Origin of GRB

supported by XRFs distribute isotropically in the sky and pose comparable durations of GRBs [52]. XRFs can be regarded as another evidence of the collimated jets.

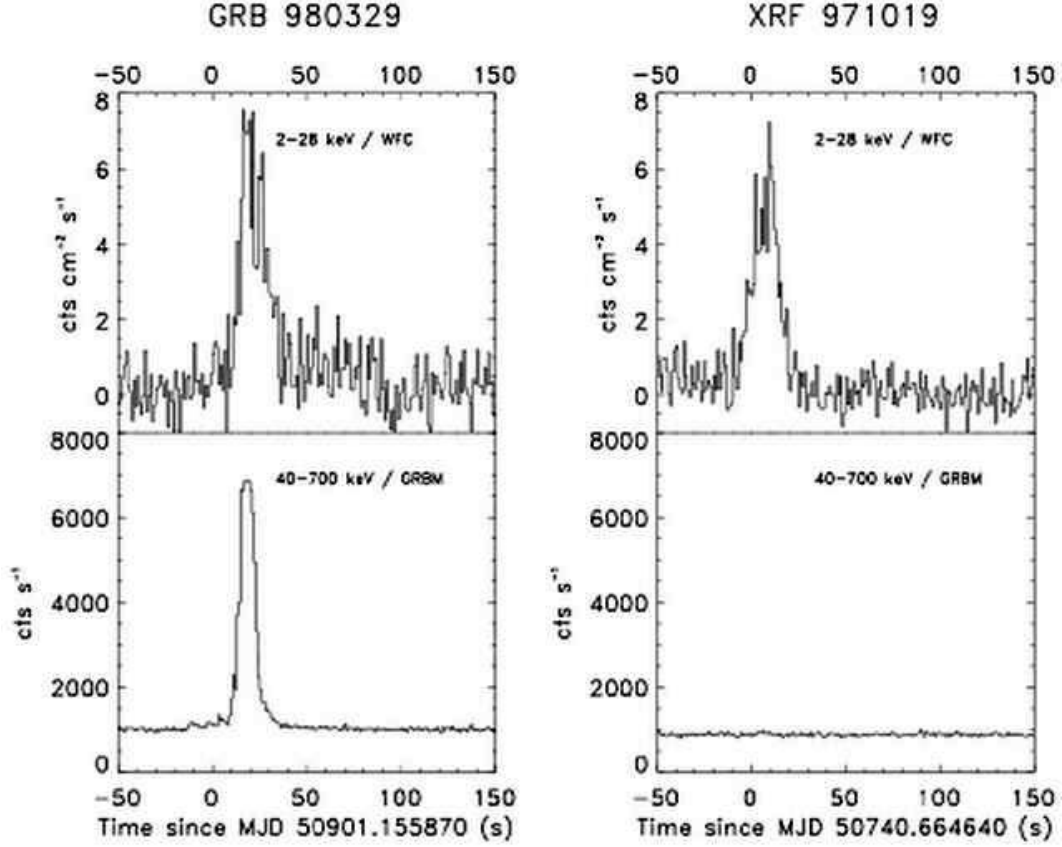


Figure 1.22: A comparison of GRB 980329 (left) and XRF 971019's (right) X-ray (top) and  $\gamma$ -ray (bottom) light curves. Both events were observed by *BeppoSAX*.

### X-ray Flare

Sometimes X-ray flares occur during the afterglow phases. Similar to XRFs, X-ray flares are the sudden high fluxes appear only in the X-ray but not in any other bands. The X-ray flares may last for minutes to a few hours. Examples from GRB 050528 and GRB 050730 are shown in Fig. 1.23 [53, 54]. The X-ray flares obviously follow the decay of the afterglows and may appear after  $> 10^4$  sec. The fact suggests the X-ray flares are more probable being produced by the mechanism in related to the afterglows than which to the prompt emissions. As the exceptionally bright X-ray flare observed with its corresponding GRB 050528, there's actually little room for the off-axis scenario be valid on X-ray flares. Theorists are trying to model the X-ray flares with delayed reverse shocks, prolonged

activity of the central engine [55], the ISM inhomogeneity [56], magneto-hydrodynamic (MHD) turbulence[57]...etc. None of the hypotheses has been strongly supported yet. .  
More discussion

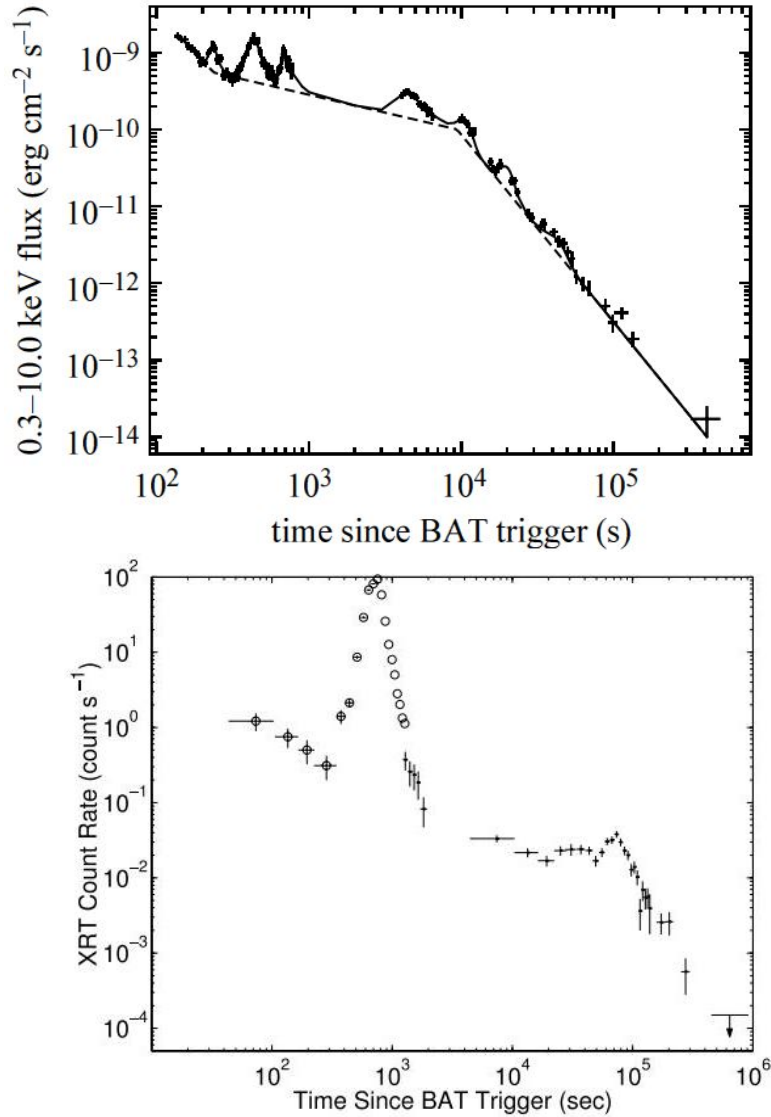


Figure 1.23: The X-ray light curves of GRB 050730 (top) and GRB 050528 (bottom) taken by *Swift*-XRT. They demonstrate the X-ray flares may appear frequently, follow the decays of the afterglows, and be gigantic as  $\sim 10^2$  times increase in rate.

### 1.3.5 Radiation mechanism of afterglow

Modes of the theoretical expectations of the afterglow models introduced in this section are somewhat in discrepancies with the observations discussed in 1.2.2. It's because these theories were mostly developed during the late 90's based on the primitive afterglow



### 1.3 Origin of GRB

observations provided by *BeppoSAX*, *HETE-2* and other 1<sup>st</sup> generation afterglow observatories. While the latest general picture of the afterglow introduced in 1.2.2 is a largely improved and modified version by *Swift* and *Fermi*. The significant progression proves the research of the afterglow is still an intensively ongoing field. People are expecting more data to unify the inconstancies of the old theories as well as develop new ones.

In this subsection, I review the theoretical implications from the afterglow's light curve and spectrum separately. Plus the lesson learned from the prompt emission, they eventually converge to the modeling of the GRB progenitors, which is discussed in 1.3.6.

#### Light curve

The general picture of the afterglow emission is illustrated by the relativistic flow dynamics, which is mostly independent of the progenitor models [22, 43]. In the context of the flow dynamical model, a GRB releases total energy  $E_0 \sim 10^{51-53}$  erg in the time  $t_b \sim T_{90}$ , and the energy is imparted as the ejecta mass  $M_{ej}$ , whose bulk Lorentz factor is  $\Gamma_0 \sim E_0/M_{ej}c^2$ .

It's expected the fireball expands fast at the beginning and starts to decelerate at the radius  $r_{dec}$  at the time  $t_{dec}$ .  $r_{dec}$  can be approximated by where the bulk Lorentz factor has dropped to half the initial value. Assuming the surrounding ISM is mostly hydrogen atoms of mass  $m_p$  and number density  $n_{ext}$ , the swept-up-mass-energy conservation gives

$$\frac{E_0}{(\Gamma_0/2)^2} \sim \frac{4\pi r_{dec}^3}{3} \times n_{ext} \times m_p c^2 \quad (1.20)$$

With some rearrangement and substitute in the realistic numbers, one has

$$r_{dec} \sim 8 \times 10^{17} \times \left(\frac{E_0}{n_{ext}}\right)^{\frac{1}{3}} \times \Gamma_0^{-\frac{2}{3}} \quad (\text{cm}) \quad (1.21)$$

The time in Earth frame is then

$$t_{dec} \sim \frac{r_{dec}}{2c(\Gamma_0/2)^2} \sim \times \left(\frac{E_0}{n_{ext}}\right)^{\frac{1}{3}} \times \Gamma_0^{-\frac{3}{8}} \quad (1.22)$$

Before the expansion reaches  $r_{dec}$ , the outflow keeps sweeping up ISM particles and converts more energy into the radiation.

[22] predicts the luminosity should grow at

$$L \propto t^2 \quad (\text{perfect radiation conversion}) \quad (1.23)$$

It can be understood easily as follow: the material swept up per unit time is proportional to the swept volume, which is  $4\pi r^2$ ; since the outflow has not yet started dissipating the accumulated energy, its Lorentz factor, i.e. expanding velocity, stays roughly constant. So one has the relation  $L \propto r^2 \propto t^2$ . However, if the swept-up energy is all accumulated but not converted into the radiation, i.e. totally inefficient, the energy is proportional to the total volume swept, which is  $\frac{4}{3}\pi r^3$ . So the luminosity is now

$$L \propto t^3 \quad (\text{totally inefficient radiation conversion}) \quad (1.24)$$

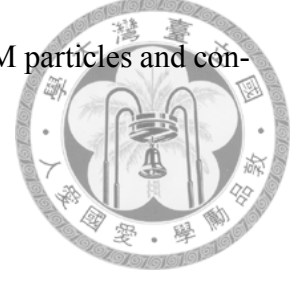
In both cases, the emissive luminosity peaks at  $r_{dec} (t_{dec})$  and declines afterward.

Unlike in the rising phase, it's not easy to have an universal description to the light curve declination. Because it may depend on the thermal-dynamical process(es) taken during the cooling, which relies on the compositions of the ejecta and ISM,  $\Gamma_0$  and  $t_{dec}$ . The current method dealing with the complexity is to apply a self-similar solution

$$L \propto r^{-g} \propto t^{\frac{-g}{1+2g}} \quad (1.25)$$

, where  $g$  is in  $3/2$  (adiabatic, totally inefficient)– $3$  (radiative, perfectly efficient) [58, 59].

To conclude, by observing the broken-power-law rising and decay of the afterglow light curve, one can determine the ejecta mass  $M_{ej}$ , the radius of the photosphere  $r_{dec}$ , the initial Lorentz factor  $\Gamma_0$ , and induces the condition of the ejecta and ISM from the thermal-dynamical index  $g$ .



## Spectrum

Similar to the prompt emission, it is believe a good fraction of the outflowing energy of the afterglow is converted into the magnetic field to trigger the synchrotron radiation, but the detail may be rather complicated due to the the involvements of the ISM, the local turbulences and Plasma physics. So far, there's also no predictive analytical model and most of the studies rely on numerical simulations with divergent assumptions of the ejecta and the ISM.

Nevertheless, based on the almost identical concept utilized in 1.3.3. the spectrum is expected to have the same form of Eqn. 1.18,

$$F_\nu \propto \begin{cases} \nu^{\frac{1}{3}} & , \nu \leq \nu_m \\ \nu^{\frac{-p+1}{2}} & , \nu_m < \nu \leq \nu_M \end{cases} \quad (1.26)$$

The differences between Eqn. 1.18 and Eqn. 1.26 are:

1. The cooling frequency  $\nu_c$  is omitted from Eqn. 1.18 because the energy (Lorentz factor) distribution is much broader in the afterglow-ISM interaction. A specific cutoff of cooling may not exist.
2. The utilization of the frequency upper bound  $\nu_M$ , which is governed by the Fermi acceleration timescale<sup>15</sup>. The ejecta doesn't generate SN-like afterglow emission above  $\nu_M$ .
3. The most distinct difference is, in the model of the prompt emission, the local Lorentz factors are approximated by constants during the short shock periods; in the model of the afterglow, on the other hand, the bulk Lorentz factor decreases continuously with the cooling. The effect is that one may expect the decreasing Lorentz boost shifts the peak frequency, i.e.  $\nu_m$ , toward the longer wavelength continuously.

<sup>15</sup>Fermi acceleration is the phenomenon of the charged particles undergoing repeatedly magnetic/electric reflections and being accelerated. It's believed to be the primary emission mechanism of SN remnant as the electrons are reflected in the ejecta by the magnetic fields generated by the shocks. The energy distribution is the same used in 1.3.3,  $N(\gamma) \propto \gamma^{-p}$ .

[60] illustrated the relativistic ejecta-synchrotron picture with some practical assumptions to the parameters, e.g. spherical expansion,  $\gamma \sim 10^2$ , adiabatic expansion, typical ISM density...etc. It predicted the peak frequency is in X-ray for the first week, then decays into optical, and eventually becomes the radio wave after a month. A few months after the prediction, the first observation of the afterglow was made from the famous GRB 970508<sup>16</sup> and provided an unquestionable evidence over a wide X-ray–radio span supporting the prediction so to the external shock-ISM model (Fig. 1.24).

The spectrum poses the rising index which consists with the prediction  $1/3$  in the radio wavelength. And it decays at a index  $-0.6$  in the synchrotron cooling range (middle) and implies  $p = 2.2$  with the index  $-(p - 1)/2$ . Since there's no obvious turning in the high energy range, the emission was emitting in the slow-cooling ( $\nu_m < \nu_c$ ) regime and the whole observed high energy range belongs to the hydrodynamic cooling. The fitted index  $-p/2 = -1.12$  gives  $p = 2.24$ , which also agrees with the result derived from the synchrotron cooling range [61]. The evolution of the non-extrapolated power-law index is also presented in Fig. 1.24. Sudden drops from the synchrotron cooling index  $-0.6$  to the hydrodynamic cooling index  $-1.12$  appear at about one day in the optical and later in the IR–radio (K-band) at about a week. The result is in consistent with the prediction of the peak shift.

---

<sup>16</sup>See 1.2.2.

### 1.3 Origin of GRB

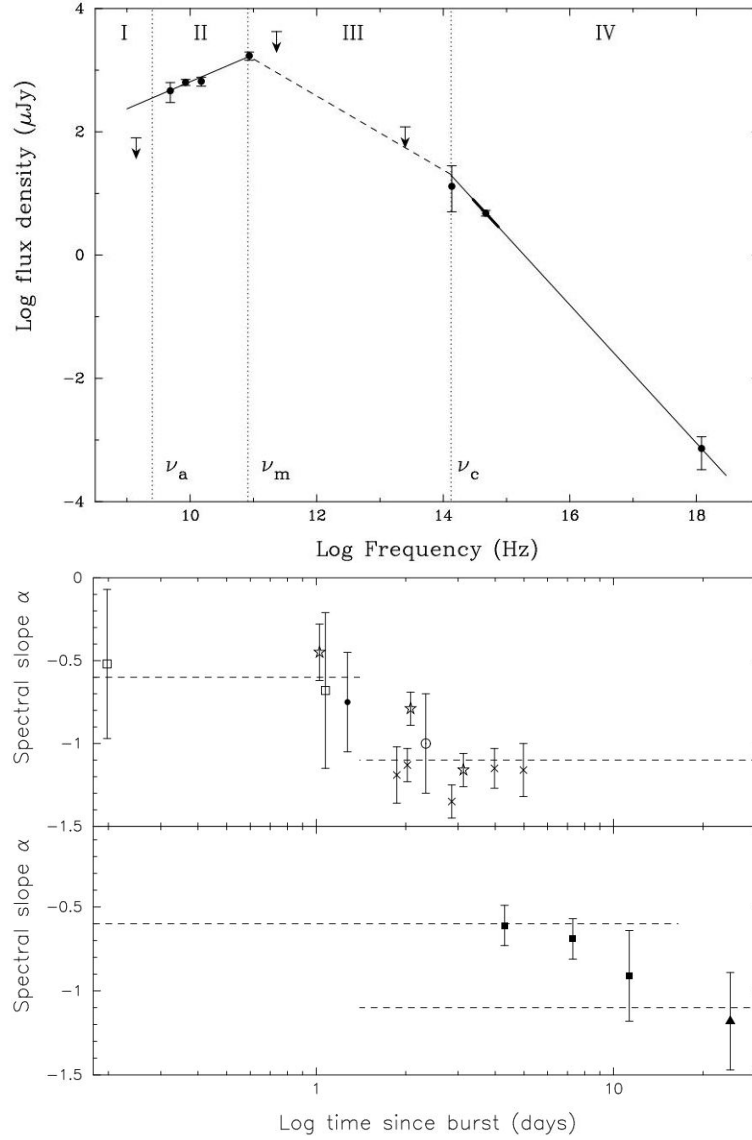


Figure 1.24: **top**: The multi-bands afterglow spectrum of GRB 970508 observed on May 21<sup>st</sup> (13 days). The data is fitted in the ranges of radio and X-ray (solid lines) and extrapolated in between (dashed line). The self-absorption low-energy cutoff, synchrotron peak, and the hydrodynamic cooling frequencies are roughly inferred and denoted by  $\nu_a < 2.5$  GHz,  $\nu_m = 86$  GHz and  $\nu_c \lesssim 1.6 \times 10^5$  GHz. The fitted power-law indices are  $0.44 \pm 0.07$ ,  $-0.6$  (extrap.) and  $-1.12 \pm 0.04$ , from left to right. **bottom**: The fitted power-law indices versus time in the optical (upper panel) and the K-band (lower panel). Lines drawn are the synchrotron cooling index  $-0.6$  and the hydrodynamic cooling index  $-1.12$ .



### 1.3.6 Progenitors

#### Long bursts

GRB 980425 was the first GRB related to SN. Back the time, only six GRBs had been measured by *BeppoSAX* with their afterglows and only two, GRB 970508 and GRB 971214, were measured with the redshifts  $z = 0.83$  and  $z = 3.4$ , respectively. There were two X-ray sources located in the error box of GRB 980425, one of them was later identified to be a Type Ic Supernove–SN1998bw [62]. There were several peculiar characteristics separated SN1998bw from other typical Type Ic SNe. First, it released totally  $\sim 10^{51}$  erg, which was about ten times the energy of others [63]. Second, combining different informations provided by spectroscopy, e.q. core composition, brightness and Lorentz factor, [63, 49, 64] pointed out SN1998bw was likely to be a core-collapse SN with an uniquely large outbursting velocity  $> 2 \times 10^5$  km/s yet released  $\sim 10^{51}$  erg into the ejecta. The model's acquired an unofficial nickname “Hypernova” from the series of papers ever after. Though the “Hypernova” progenitor is now concurred to be mostly correct on long bursts, GRB 980425-SN1998bw connection remained controversial in the later 5 years due to the facts that

1. Neither the two X-ray sources in the error box was rather preferable.
2. It had non-cosmological small redshift  $z = 0.0085$ .
3. The released energy was one OM larger than the common SNe, yet still one OM short compared with the typical number  $\gtrsim 10^{52}$  erg known at the time.
4. No optical afterglow was observed by *BeppoSAX* (possibly due to its dimness).

The disputation was eliminated by the detection of GRB 030329-SN2003dh<sup>17</sup>. GRB 030329 was a truly cosmological ( $z = 0.1685$ ) event, and was 3 OMs stronger than GRB 980425. Moreover, with its optical afterglow obtained (Fig. 1.12 & Fig. 1.13), the unquestionable evolution from the power-laws to the Type Ic SN signatures showed in both

---

<sup>17</sup>Also see 1.2.2

### 1.3 Origin of GRB

the spectrum and the light curve. The result was compared to SN1998bw and concurred GRB 980425 and SN1998bw was also a correct GRB-progenitor connection [18].

So far about 30 GRBs have had the afterglow spectra fell into SN signatures, about 10 were directly associated to the companion SNe. All the SN-connected GRBs are located in  $z < 1.1$ , which is viewed as being biased by the detection efficiency drawback of high- $z$  signals.

Woosley made an early prediction before the afterglow era the long GRBs would only be produced by the massive stars that were stripped from the Hydrogen envelopes, e.q. Type I SNe or called Wolf-Rayet (WR) stars<sup>18</sup> [65]. The argument provided were:

1. The most compact Type II SNe have the radius about 100 light seconds. When the jets plowed outward, the (prompt) light curves should have had been smoothened by the time scale of 100 sec. Which is obviously violated the observation  $\delta t \sim 1$  sec.
2. The progenitor systems must generate anisotropic magnetic fields to collimate the charged outflows. An intuitive realization was through a fast rotating system, e.q. Type I SNe or binary systems.

The assumption of the fast rotation is regarded as the most stringent requirement that separates the GRB-progenitors from other WR stars/binary systems. In fact, by comparing the absence of the late-time radio emissions, it is pointed out in [66] no more than 6% Type Ibc SNe make GRB-progenitors. The fraction is similar to which of the rotating SNe.

Today, two most favorable long burst progenitor models emerging from the Hypernova picture are the “millisecond magnetars” and the “collapsars”.

A Neutron star (NS) is called a millisecond magnetar when it rotates at the rate about 1 msec [67]. It possesses the energy  $\sim 10^{52}$  erg and the magnetic field  $\sim 10^{15}$  G which [68] proposes to be the necessary ingredients of generating GRBs. Magnetars are found in younger SN remnants that are likely to be derived from the populations heavier than  $30 M_{\odot}$ . It is worth noting that, the birthrate of the magnetars is about the same of the same of the ordinary SNe. So again, only a small fraction of the magnetars produce GRBs.

---

<sup>18</sup>SNe with the Hydrogen absorption shows in the spectra are Type II.

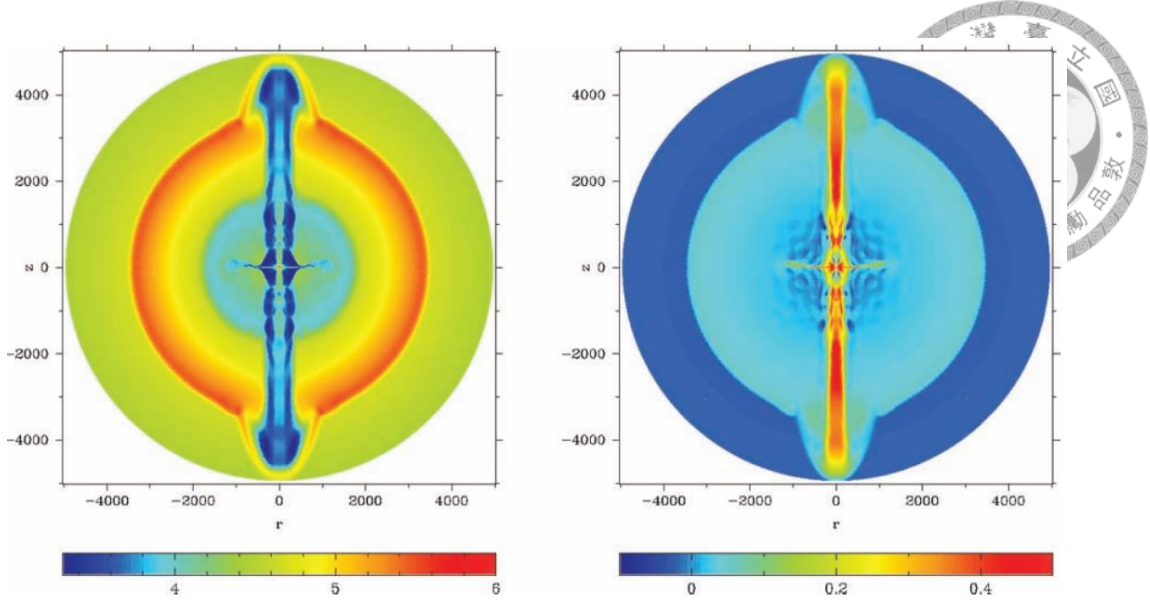


Figure 1.25: An example of the simulated magnetar explosion. The model has total energy  $10^{52}$  erg, magnetic field  $10^{15}$  G, rotates at the rate 2 msec. and emits at  $3 \times 10^{50}$  erg/sec. The left-hand panel shows the density  $\log_{10} \rho$  in  $\text{g}/\text{cm}^3$ ; the right-hand panel shows the velocity in  $v^r/c$ . In both figures, the unit of length is  $\text{GM}/c^2$ , where  $M$  is the core mass  $1.4M_{\odot}$ .

Recent simulation studies have demonstrated that the magnetars are capable of generating the relativistic and magnetic-collimated jets, and dissipating energy more than  $10^{51}$  erg (Fig. 1.25) [69].

SNe occasionally forms black holes (BHs). Many studies have shown that the falling-back processes of stars heavier than  $25M_{\odot}$  produce relativistic outflows, and are often accompanied by highly luminous X-ray transients. The processes are called the collapsars. As stated previously, in order to generate GRBs, one expects the Hydrogen envelopes to be evacuated beforehand for the benefit of the Gamma-ray transmission. One way to achieve the evacuation is when the inner cores of the collapsars collapse and forms a BH in an instant while the outer shells are still falling. Then the hydrogen envelopes are expelled during the lag time. To ensure the lag time is sufficient for the Hydrogen to be fully evacuated, the cores must be rotating rapidly at the comparable angular momenta of the Magnetars. Providing the whole scenario is proceeded, GRBs may be generated [65, 70].



### Short bursts

It's far greater challenging in consideration of the short bursts. Limited by the responding times of instruments, only a dozen of the short bursts have been observed with the afterglows. None of the observations shows direct connection to SNe. In addition to the statistical argument of  $T_{90}$  presented in 1.2.1, the result further supports the short GRBs are physically distinct from the long GRBs. Taking into account the peak brightness and the total energy, i.e. harder photons but 1-OM less energetic in total, theories started with suggesting the short bursts may be produced by the syntheses of the radioactive elements during the decompositions of the very dense and neutron-rich environments [71, 72]. Aside from the Magnetars and Collapsars which produce longer emissions, the intensive rotating environments can be realized by the mergers of compact objects, e.q. NS or BH [74]. The merger of compact objects are also the possible candidate of the Type Ia SNe, which is known as the double-degenerate (DD) model [75]. Presented in Fig. 1.26 is the latest simulation study demonstrates the process when a NS and a BH form an initial binary system closely and become a contact rotating system with the specific angular momentum larger than a maximally rotating BH, a small fraction  $\sim 1\%$  of the mass/energy is thrown out and forms a magnetized rotating torus. The magnetic field is subsequently generated along the axis of rotation of the resulting BH. It creates the environment satisfying the requirements given in [68], e.q.  $B \sim 10^{15}$  G,  $E \sim 10^{51}$  erg...etc, but still having difficulty prolonging the jet over 50 msec. and generating realistic short bursts [76].

## 1.4 PERSPECTIVE PHYSICS OF UFFO

Ultra-Fast Flash Observatory (*UFFO*) is an innovative space-borne detector built to be the first GRB observatory capable of responding to the UV–optical signals within one sec. The current limit of the responding time is set by the *Swift* at about 100 sec. after prompt emission triggers<sup>19</sup>. Fine observations of the sub-minute afterglows starting from the first second will hopefully be provided by *UFFO* in a few years.

<sup>19</sup>The instrumental limitation is reviewed in 2.2



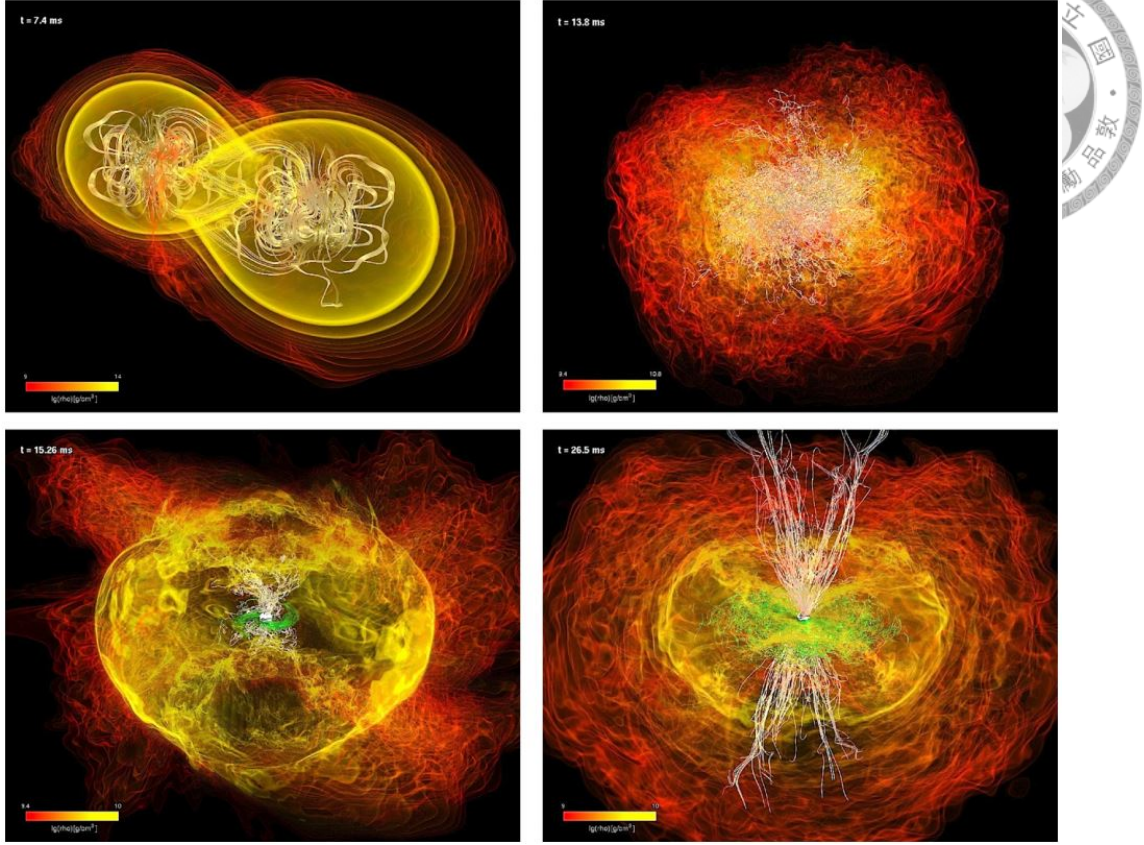


Figure 1.26: The simulated evolution of the NS-BH merger scenario. The region colored by the noted color code presents the density in  $\log_{10}\rho$  ( $\text{g}/\text{cm}^3$ ). The green and white lines present the magnetic field inside and outside the BH, respectively. The panels from top-left, top-right, lower-left to lower-right are the snapshots of the merger, before collapsing to BH, initial BH, after forming the torus, respectively with the time noted in the corners.

In this section, I discuss four selected topics which *UFFO* is likely to shed great lights on, namely the GRB standard candle proposition, the internal/external shocks unification, the physical origin of the short bursts and the dark bursts.

### 1.4.1 GRBs as standard candles

Not until lately, people had accepted the 2-sec. criteria as being the only certain classification discriminating different GRBs<sup>20</sup>. Rather than clarifying the long-and-short classification, the launch of *Swift* revealed an even complicated nature of GRBs from the early afterglows.

According to the afterglow samples of *Swift*, GRBs may be further classified upon

<sup>20</sup>Refer to 1.2.1

#### 1.4 Perspective physics of UFFO

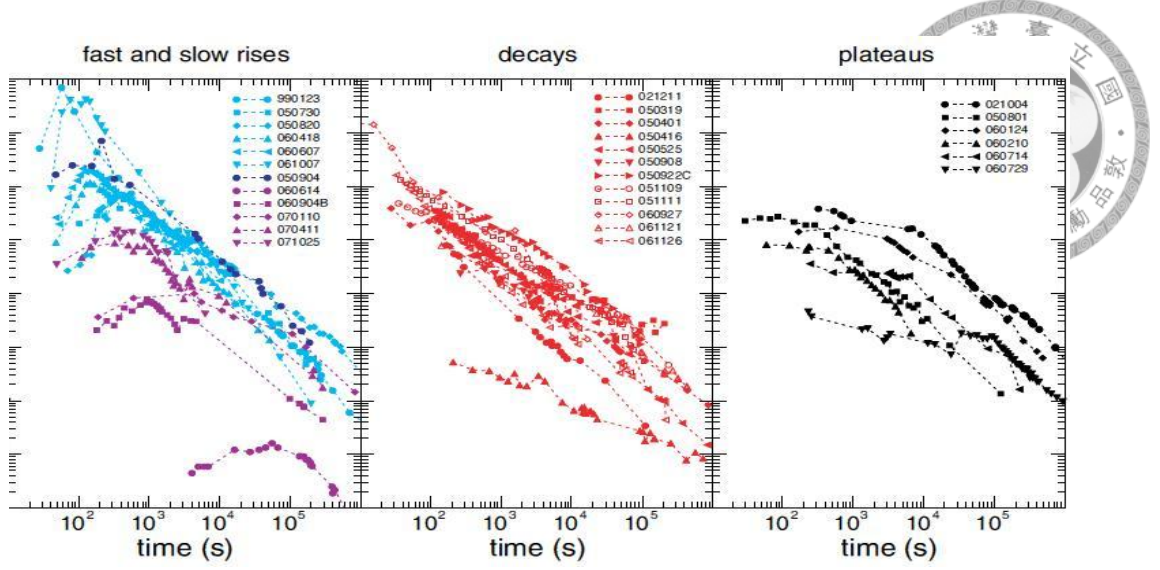


Figure 1.27: 30 selected *Swift*-*UVOT* optical light curves. The samples are selected with their redshifts determined. Totally 6 samples are classified as fast-rise (light blue), 5 as slow-rise (purple), 1 in the rise class but could be fast or slow-rise (dark blue), 12 as decay (red), and 6 as plateau (black). For better comparison, all the light curves are corrected in the fluxes for Galactic and host system duct extinction and are manually shifted to common  $z = 2$ . The classification criteria and detail discussions are given in the corresponding paragraph.

their early light curves, e.q. the first few minutes. Fig. 1.27 presents the classification of the rise, the decay and the plateau types based on the criteria [77]:

- The rise type: The light curves exhibit certain rising fluxes ( $F \propto t^{>0.5}$ ) at the beginnings. Those peak before 100 sec. are classified as the fast-rise type, others are classified as the slow-rise type.
- The decay type: The light curves exhibit fast decays ( $F \propto t^{\leq -1}$ ) at the beginnings.
- The plateau type: The light curves exhibit “plateau” features of uncertain tendencies, e.q.  $F \propto t^{-0.20.1}$ , and last for at least one decade.

As a result, about 2/5 of the *Swift* samples appeared to be rising in the early stages, e.q.  $t \sim 10^{2-3}$  sec. About half of them showed  $t^{\sim 2.5}$  fast rises and reached the peak luminosities close to the discriminating time 100 sec. (fast-rise type), and the others rose slowly at  $t^{\sim 0.6}$  and reached the peaks around  $10^{3-4}$  sec (slow-rise type). Besides the rise type, about 2/5 of the samples showed roughly monotonic decays at  $t^{\sim -1.0}$  (decay type) started from the first minute. In parallel with the rise- and decay- types, about 1/5 of the

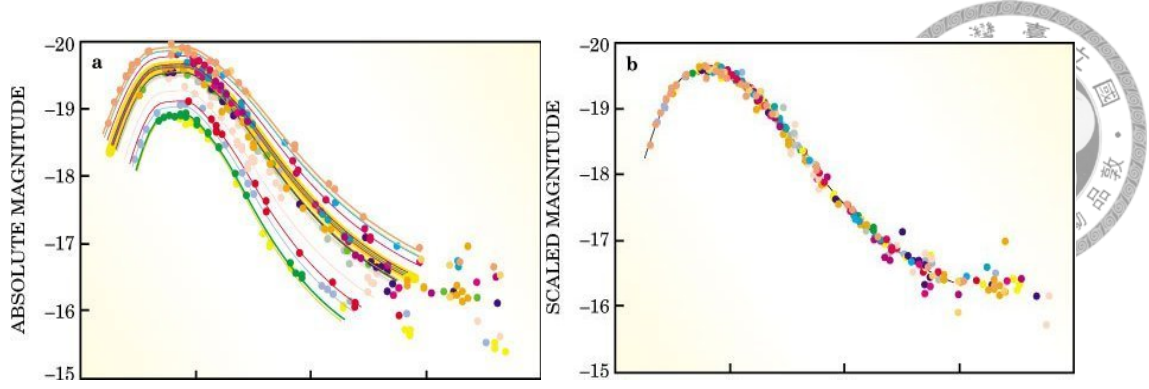


Figure 1.28: An illustration of how Type Ia SNe are utilized as the standard candles. The unprocessed light curves of Type Ia SNe are shown in the left panel. As long as the redshifts are determined through the spectroscopy, the luminosities can be rescaled to the same footing, e.g. boosted to the same  $z$ , which is the case in the right panel. Type Ia SNe exhibits a almost constant on-site magnitude which makes them competent standard candles.

samples started with the flat “plateaus” in the first hour (plateau type)<sup>21</sup>. Readers may have noticed that most of the light curves start no earlier than  $10^2$  sec., even when they do, they are most likely to be recored with only 1 or 2 data points.

There’s a peculiar feature discovered from Fig. 1.27. While the decay (red) and the plateau (black) types spread 2 OM in the luminosities, the fast-rise light curves (light blue) tend to concentrate withing 0.5 OM. This feature may remind one of the unique character of Type Ia SNe being the  $z$ -calibrated standard candles, and the Type Ia SNe are also the expected candidates of short-hard bursts<sup>22</sup>! Fig. 1.28 illustrates the standard candle character of Type Ia SNe [81]. Reader may find the similarity between the light curves of the fast-rise type and the Type Ia SNe. It is proposed in [77] GRBs might as well serve as the standard candles, but with the great advantage over Type Ia SNe that GRBs may be observed from large  $zs$ . The hint of GRBs being calibrated standard candles can be better visualized by plotting the 12 peaks of the rise types in Fig. 1.27 (Fig. 1.29). Instead a few outliers, the peak luminosities align with each other, which implies the emissions pose a constant on-site luminosity.

<sup>21</sup>Recent theories suggest the plateau feature might be the consequences of the refresh shocks or the prolonged central engine activities. [78, 79] argue it may be caused by the wider Lorentz factor distributions in the ejecta which prolong the energy ejections into the external shock-ISM interactions. The late-time shocks are called the refresh shocks. Investigating the detail of the Collapsar process, [80] suggests the falling-back of the outer layers could be delayed up to one day in certain situations and results in the delayed energy ejection.

<sup>22</sup>Note that the samples presented here are mostly long bursts. And the long bursts’ progenitors are Type Ibc SNe.

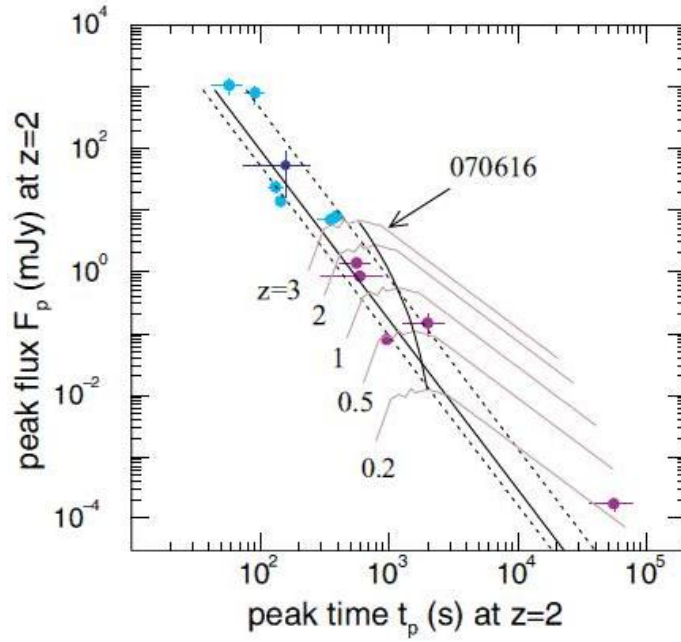


Figure 1.29: The peak luminosities of the 12 rise-type light curves, with the same color code in Fig. 1.27. The solid line represents the best (log-)linear fit with the correlation coefficient  $-0.97 \pm 0.01$ ; the dotted lines bound the  $1\sigma$  region. Also shown in the figure are the hypothetical light curves of GRB 070616 (faded lines), whose redshift is unknown.

More afterglow data in the early stage is urgent to further investigate the standard candle proposition. As the fast-rise light curves peaked closely to the responding time limit of *Swift*, they were mostly poorly resolved before 100 sec. What is more, there was a significant fraction of samples were observed with only decays started from  $\sim 100$  sec. It led to the uncertainty whether they were indeed decaying monotonically or they peaked some times before 100 sec. With the sub-minute light curves, *UFFO* will definitely be capable to examine the standard candle proposition rigorously.

### 1.4.2 Internal/External shocks unification

In 1.3.5, I review the emission mechanism of the afterglow. Provided the complete afterglow light curve obtained, the derivation therein suggests many essential parameters of the central engine and the ejecta may be determined directly, e.g. masses, Lorentz factors...etc. It is also understood from the flow dynamical nature, if the X-ray–optical band is completely external-shock dominant, one expects the light curves to be totally smooth.



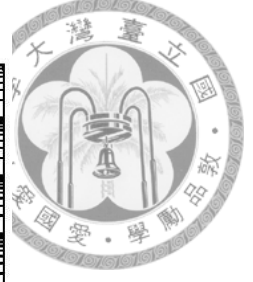
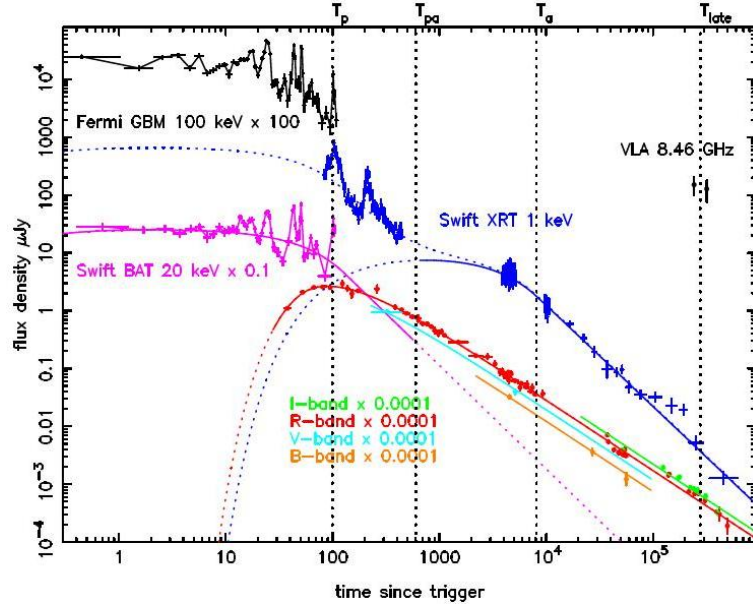


Figure 1.30: The multi-wavelength light curves of the energetic GRB 080810.  $T_p = 5 \times 10^1$  sec.,  $T_{pa} \sim 6 \times 10^2$  sec.,  $T_a \sim 8 \times 10^3$  sec. and  $T_{late} \sim 3 \times 10^5$  sec. mark the times of end of the prompt emission, the end of the  $\gamma$ -ray/X-ray fits overlapping phase, start of the power-law decay and the start of radio wave observation.

Fig. 1.30 shows an obvious counter example to the theoretical expectation [82]. From the bright event GRB 080810, a clear transition of the prompt-emission-like pattern to the afterglow-like power-law decay was observed in 50–8000 sec. after trigger at 1 keV. It demonstrates that during the early stage, e.g.  $10^1$ – $10^4$  sec. according to the fits in Fig. 1.30, the afterglow is actually an internal-external-shocks mixture rather than which expected by the simple flow-dynamical picture. *Swift* has revealed a part of the mixture starts from  $\sim 100$  sec., *UFO* will further prob the entire time lapse with a much finer resolution. The result may put on a tighter constraint to the current fireball model, verify the relativistic flow dynamical prescription, and clarify the roles of the internal shocks, the external shocks and the ISM in their interplay of GRBs.

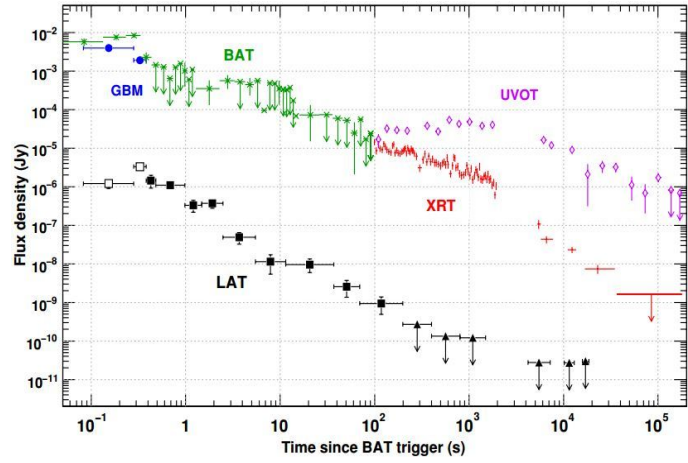
### 1.4.3 Origination of Short-Hard Bursts

It was from the afterglows of the long bursts did the scientists discovered the connection of long GRBs to Type Ibc SNe. Now theories suggest the progenitors of the short-hard bursts (SHBs) might be the mergers of the compact objects and point out the SN signa-

#### 1.4 Perspective physics of UFFO

ture may be observed following suit (See 1.3.6). However, suffering from the dimness of SHBs plus the responding limitation of *Swift*, only about 10 SHBs has been observed by *Swift* in the X-ray–optical ( $\sim 1/\text{yr.}$ ). Even in some extremely bright cases, e.g. GRB 090510 (Fig. 1.31 [83][84]<sup>23</sup>), the afterglows started at  $\sim 10^2$  sec. and subsided in about 1 day. It is suggested in [5], instead of tracing the fast subsiding SHB afterglows, future experiments may also search for the early clues of the progenitors in the rather bright stages. It is where *UFFO* will immediately come in handy.

Figure 1.31: The collected light curve of *Swift* SHB GRB 090510. Instruments shown are LAT (100 MeV–4 GeV, square, hollowed for the prompt emission), GBM (8 keV–1 MeV, circle), BAT (15–350 keV, star), XRT (0.2–10 keV, cross), UVOT (renormalized to V-band).  $1\sigma$  and  $2\sigma$  ranges are noted for error bars and upper limits, respectively.



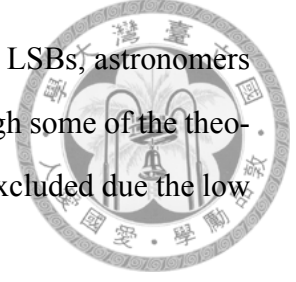
#### 1.4.4 Dark bursts

The dark bursts were firstly proposed by *BeppoSAX* to address the GRBs whose afterglows fell only in the X-ray but not UV–optical. *BeppoSAX* observed the afterglows in X-ray from more than 90% events, but only 1/3 were accompanied by UV–optical signals. By the time it was unclear if it's due to the instrument's limitation or the events were indeed “dark”. *HETE-2*, with its faster response, was able to identify some fast dimming events and temporarily concluded  $\geq 90\%$  seen-to-be-dark *BeppoSAX* events were detection biased. Unexpectedly the issue resurfaced with the launch of *Swift*. While the latest limit of the dark long-soft bursts (LSBs) set at 10%–20% roughly included the pre-*Swift* expectation, with a handful of optically-valid SHBs, studies simultaneously pointed out the first time the dark bursts might and might not exist among SHBs<sup>24</sup> [86, 87]. As a start,

<sup>23</sup>a revision to [83].

<sup>24</sup>all SHBs were basically seemed dark before *Swift*

by comparing the discrepancies between the dark SHBs and the dark LSBs, astronomers were able to evaluate the candidate theories for the first time. Although some of the theories were argued to be less favored by the *Swift* data, none has been excluded due the low statistics of the SHBs.



Several explanations have been proposed to cause the optical darkness:

1. Obscuration scenario: As some dark bursts were observed with the evidences the host galaxies exhibited high dust extinctions, e.q. see [88], theorists are suggesting if GRBs occur in moderately distant galaxies with high dust extinctions, the redshifted obscured signals might lead to the results of dark bursts. Note that the obscuration scenario predicts insignificant chromatic decays since the dusty extinction should be achromatic and high redshifts are not necessary.
2. Intergalactic scenario: As mentioned above, the obscuration scenario has trouble adjusting for the chromatic afterglows. Inspired by some “reddish” events such as GRB 980329 [89], theorists have analytically derived the spectra when the highly-redshifted ( $z > 4$ ) afterglows are absorbed by the intergalactic Ly- $\alpha$  forests and concluded such events are likely to be identified as the dark bursts [90].
3. Intrinsic inefficiency: The emissions may have low intrinsic optical-conversion efficiencies and result in “truly dark” bursts. In other words, unexpected new physics must take places in either the central engines, the ejecta, or through other mechanisms.
4. Detection bias: The slow-following-up bias was obviously the main cause to the pre-*Swift* dark bursts. But since the *Swift* has obtained the similar result as *HETE-2*, the responding bias should be less important.

One way to present the discrepancy between SHBs and LSBs is by plotting the events in the optical-X-ray fluxes correspondence plot (Fig. 1.32). According to the general fire-ball expansion discussed in 1.3.5, assuming synchrotron radiation, a typical cooling fre-



#### 1.4 Perspective physics of UFFO

quency  $\nu_c$  is expected to locate between the X-ray and the optical bands, i.e.

$$F_\nu \propto t^{\beta_{ox}} \propto \begin{cases} t^{-(1-p)/2} & , \nu < \nu_c, \text{ optical} \\ t^{-p/2} & , \nu \geq \nu_c, \text{ X-ray} \end{cases} \quad (1.27)$$



Considering a typical  $p = 2$ , the allowed region is bounded by the “Dark” Line (dashed) and the X-ray dominant line (dotted) in the Fig. 1.32.  $\beta_{ox} < 0.5$  implies inefficient fast-cooling optical emissions and  $\beta_{ox} > 1$  implies X-ray dominant afterglows, both are not the typical cases. Nevertheless, two notions should be emphasized; first, typically  $p \in [2.0, 2.5]$ , so the events above the X-ray dominant line may be reconciled by  $\beta_{ox,upper} = 1.0 \rightarrow 1.25$ ; second, the events below  $\beta_{ox,lower} = 0.5$  are expected to have major emissions in the IR–radio while being fastly decaying ( $\beta_{ox} < -1$ ) in optical [91].

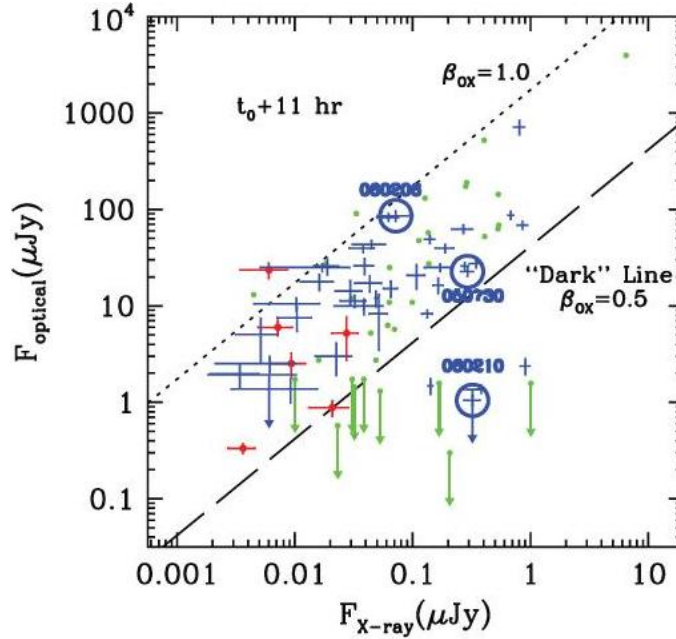


Figure 1.32: Optical-X-ray flux correlations of selected *Swift* GRBs [86]. Data are selected if valid in optical. LSBs and SHBs are marked by blue and red symbols, respectively. Three circled events are the highly ( $>3.9$ , suffice the intergalactic scenario) redshifted events. Also plotted are the pro-*Swift* events (green), with the dots and arrows represent the optically-valid bursts and optical upper limits of the dark bursts. The two lines bound the region that the cooling frequency  $\nu_c$  lays between X-ray and optical, which is the common situation of afterglows. Readers should refer to the corresponding paragraph for detail.

One may infer from Fig. 1.32 the optical afterglow universality might exist despite LSBs or SHBs. Several comments can be made from the figure:

1. Dark bursts' optical fluxes should be at most 1–2 OMs smaller than the common bursts.
2. Since the fireball-based allowed region governs all the non-dark SHBs and LSBs equally and discriminates the (long) dark bursts nicely, the optical afterglow universality might exist based on the equally-valid flow dynamical fireball model.
3. 6 SHBs have been measured in optical, no dark SHBs have been discovered. It is argued in [86] the dark bursts might not exist among SHBs. But according to the similar points, namely 1. 2., [87] interprets it as a hint to the existence of dark SHBs. Both papers note the arguments are inconclusive due to the facts of the low statistics of SHBs, and the exclusive limit of luminosity of the dark SHBs should be very close to *Swift*'s detection limit.
4. As the two highly redshifted events being located in the allowed region, together with the identifications of the high Hydrogen column densities in the host galaxies, it is stated in the references the intergalactic scenario is less favored than the obscuration scenario. However, the statistics is also too low to be conclusive.

*UFFO* is promised with the rapidity to investigate the long-standing mystery of the dark bursts, not only in the manner of catching the bright first-second light curves, but also guaranteeing effective data accumulation. The knowledge of the dark bursts may be the key to the understanding of the galactic composition, cosmic dust population, and the Universe evolution.



#### *1.4 Perspective physics of UFFO*





## Bibliography

- [1] Klebesadel, R. W., et al. 1973, *ApJ*, 182, L85
- [2] Tegmark, M., et al. 1996, *ApJ*, 573, 312
- [3] Band, D., et al. 1996, *ApJ*, 413, 281
- [4] Kaneko, Y., et al. 2006, *ApJS*, 166, 298
- [5] Naker, E., et al. 2002, *MNRAS*, 331, 40
- [6] Norris, J. P., et al. 1996, *ApJ*, 459, 393
- [7] Qin, Y. 2000, *PAsJ*, 52, 759
- [8] Qin, Y. 2005, *MNRAS*, 358, 1320
- [9] Ruderman, M. 1975, *7<sup>th</sup> Taxes Symposium on Relativistic Astrophysics*, N. Y. Acad. Scin., 262, 164
- [10] Costa, E. 1997, *Nature*, 387, 783
- [11] Van Paradijs, J., et al. 1997, *Nature*, 386, 686
- [12] Djorgovski, J. S., et al. 2003, *ApJ*, 591, L13
- [13] Jacobsson, P. 2006, *A&A*, 447, 897
- [14] Bloom, J. S., et al. 2002, *AJ*, 123, 1111
- [15] Galama, T. J., et al. 2001, *ApJ*, 549, L209
- [16] Piro, L. 2002, *ApJ*, 577, 680

## BIBLIOGRAPHY

- [17] Stratta, G., et al. 2004, *ApJ*, 608, 846
- [18] Hjort, J., et al. 2003, *Nature*, 423, 847
- [19] Zeh, A., et al. 2003, *GCN notice* #2081
- [20] Mangano, V., et al. 2007, *arXiv:astro-ph*, 0701812
- [21] Kouveliotou, C., et al. 2013, *Gamma-ray Bursts*, Cambridge Univ. Pres.
- [22] Rees, M. J., et al. 1992, *MNRAS*, 258, L41
- [23] Bahcall, J. and Ostriker, J. 1995, *Some Unsolved Problems in Astrophysics*, p. 237, Princeton Univ. Pres. Original credit goes to Piran, T.
- [24] Zou, Y.-C., et al. 2010, *MNRAS*, 402, 1854
- [25] Sari, R., et al. 1997, *ApJ*, 485, 270
- [26] Fenimore, E. E., et al. 1996, *ApJ*, 473, 998
- [27] Lazar, A., et al. 2009, *ApJ*, 695, L10
- [28] Katz, J. I., et al. 1994, *ApJ*, 422, 248
- [29] Rybicki, G. B., et al. 1979, *Radiative Process in Astrophysics*, p. 221, N. Y.: Wiley-Interscience
- [30] Fenimore, E. E., et al. 1995, *ApJ*, 448, L101
- [31] Sari, R., et al. 1998, *ApJ*, 494, L10
- [32] Preece, R. D., et al. 1998, *ApJ*, 506, L26
- [33] Katz, J. I. 1994, *ApJ*, 423, L107
- [34] Tavani, M. 1995, *Ap&SS*, 231(1), 181
- [35] Derishev, E. V., et al. 2001, *A&A*, 372, 1071
- [36] Nakar, E., et al. 2009, *ApJ*, 703, 675





- [37] Fan, Y.-Z. 2010, *MNRAS*, 403, 483
- [38] Ando, et al. 2008, *ApJ*, 689, 1150
- [39] Piran, T. 1999, *Phys. Rep.*, 314, 575
- [40] Felix, R., et al. 2005, *arXiv:astro-ph*, 0504450
- [41] Ryde, F., et al. 2009, *arXiv:astro-ph*, 0911.2025v3
- [42] Guiriec, S., et al. 2013, *arXiv:astro-ph*, 1210.7252v2
- [43] Meszaros, P., et al. 1993, *ApJ*, 405, 278
- [44] Akerlof, C., et al. 1999, *Nature*, 398, 400
- [45] Li, W., et al. 2003, *ApJ*, 586, L9
- [46] Klotz, A., et al. 2006, *A&A*, 451, L39
- [47] Laskar, T., et al. 2013, *arXiv:astro-ph*, 1305.2453
- [48] Sari, R. 1999, *ApJ*, 524, L43
- [49] Kulkarni, S. R., et al. 1998, *Nature*, 393, 35
- [50] Kulkarni, S. R., et al. 1999, *Nature*, 398, 389
- [51] Harrison, F. A., et al. 1999, *ApJ*, 523, L121
- [52] Heise, J. 2003, *AIP Conf. Proc.*, 662, 229
- [53] Falcone, A. D. 2006, *ApJ*, 461, 1010
- [54] Pandey, S. B., et al. 2006, *A&A*, 460, 415
- [55] Romano, P. 2006, *A&A*, 450, 59
- [56] Sari, R. 1999, *Ph. D thesis*, Hebrew Univ.
- [57] Proga, D., et al. 2006, *MNRAS*, 370, 61

## BIBLIOGRAPHY

- [58] Sari, R. 1997, *ApJ*, 489, L37
- [59] Waxman, E. 1997, *ApJ*, 491, L19
- [60] Meszaros, P., et al. 1997, *ApJ*, 476, 232
- [61] Galama, T. J., et al. 1998, *ApJ*, 500, L97
- [62] Galama, T. J., et al. 1998, *Nature*, 395, 670
- [63] Paczynski, B. 1998, *ApJ*, 494, L45
- [64] Iwamoto, K., et al. 1999, *Nature*, 395, 672
- [65] Woosley, S. E. 1993, *ApJ*, 405, 273
- [66] Soderberg, A. M. 2004, *ApJ*, 607, L13
- [67] Thompson, C. 2006, *ApJ*, 473, 322
- [68] Kouveliotou, C. 1998, *Nature*, 393, 235
- [69] Komissarov, S. S., et al. 2008, *MNRAS*, 382, 1029
- [70] MacFadyen, A. I., et al. 1999, *ApJ*, 524, 262
- [71] Li, L.-X., et al. 1998, *ApJ*, 507, L59
- [72] Rosswog, S., et al. 2002, *MNRAS*, 336, L7
- [73] Ruiter, A., et al. 2010, *ApJ*, 717, 1006
- [74] Paczynski, B. 1986, *ApJ*, 308, L43
- [75] Wang, B., et al. 2012, *arXiv:astro-ph*, 1204.1155v2
- [76] Rezzolla, L., et al. 2011, *ApJ*, 723, L6
- [77] Panaitescu, A., et al. 2008, *MNRAS*, 387, 497
- [78] Rees, M. J., et al. 1998, *ApJ*, 496, L1





- [79] Sari, R., et al. 2000, *ApJ*, 535, L33
- [80] Woosley, S. E. 2006, *AIP Conf. Proc.*, 836, 398
- [81] Wang, Y., et al. 2008, *MNRAS*, 389, 489
- [82] Page09, K. L., et al. 2009, *arXiv:astro-ph*, 0907.4578
- [83] Pasquale, M. D., et al. 2010, *ApJ*, 709, L146
- [84] Guelbenzu, A. N. 2012, *A&A*, 538, 207
- [85] Park, I. H. 2013, *New J. of Phys.*, 15, 023031
- [86] Gehrels, N., et al. 2008, *ApJ*, 689, 1161
- [87] Zheng, W.-K., et al. 2009, *RAA*, 9, 10, 1103
- [88] Djorgovski, S. G., et al. 2001, *ApJ*, 562, 654
- [89] Fruchter, A. S. 1999, *ApJ*, 512, L4
- [90] Lamb, D. Q., et al. 2000, *ApJ*, 536, 1
- [91] Jakobsson, P., et al. 2004, *ApJ*, 617, L21



## *BIBLIOGRAPHY*





## CHAPTER 2

# UFFO

Looking back over the history of the GRB research, the discovery of the afterglow is unquestionably one of the most crucial ingredient boosts the progression of the field. *UFFO*, as it is named, is built to be the fastest ever GRB observatory responding to the GRB afterglows and guarantees a new frontier of Astrophysics.

In this chapter, the overview of *UFFO* is given in 2.1 as an opening, then the current limitations of other experiments are reviewed in 2.2. In 2.3 and 2.4, the constructions and operational principles of the two major detectors—*UBAT* and *SMT*, are introduced. Finally in 2.5, as being the focus of this thesis, an elaboration on the *UBAT* focal surface is provided.

## 2.1 OVERVIEW

### Plan

In the past twenty years, experiments from *BeppoSAX* to the latest *Swift* and *Fermi* have helped astronomers accumulating an appreciable deal of UV–optical data of GRBs that brings about the developments of GRB physics, SN physics and Cosmology. Yet limited by their choices of the mechanical designs and operation schemes, even the most advanced ones can only aim their UV–optical telescopes to the prompt sources a few minutes lagging behind. Through MEMS (Micro-Electrical-Mechanical System), *UFFO* has overcome the “minute barrier” and is able to target its V-band telescope, stabilize it, and begins to take data within several seconds.

## 2.1 Overview

*UFFO* is scheduled to be launched in 2014 on Russian spacecraft *Lomonosov*. It will be orbiting Earth every 9.6 hr. at the altitude 509 km together with  $\gamma$ -ray spectrometer *BDRG* (0.01–30 MeV), UHECR (ultra-high energy cosmic ray) telescope *TUS* (105–6 PeV), fast optical observatory *SHOCK* and other scientific apparatuses. Due to the payload limitation of *Lomonosov*, the launch schedule and the MEMS mirror R&D, the MEMS-mirror-equipped *UFFO* was replaced with the *UFFO*-pathfinder (*UFFO-p*) which fitted the payload limitation and utilized the motorized slewing mirror stage (SMS) as a comparable demonstration of the idea of the original *UFFO*. Fig. 2.1 presents *Lomonosov* and *UFFO-p*<sup>1</sup>.

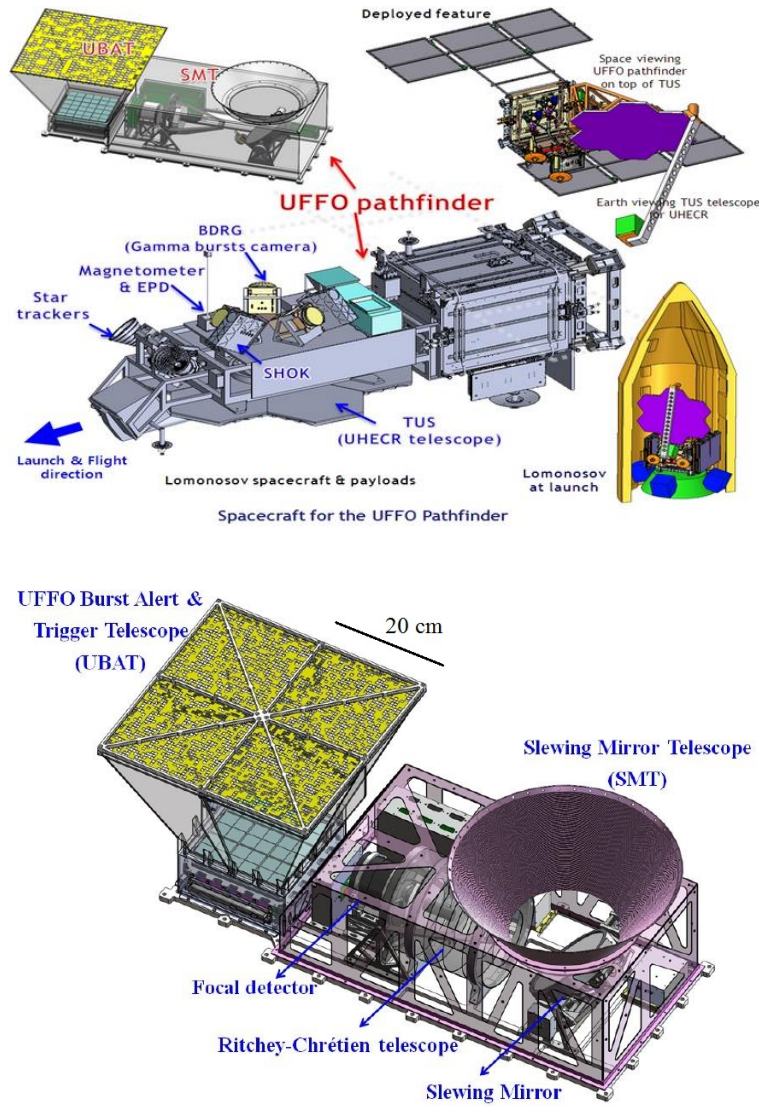


Figure 2.1: The schematics of *Lomonosov* and *UFFO-p* [1, 2].

<sup>1</sup>I will simply use the name *UFFO* hereafter.



## Operation

*UFFO* triggers on GRBs and other transient X-ray to soft  $\gamma$ -ray events in 15–150 keV [3]. It's composed of two major telescopes: *UBAT* (*UFFO* Burst Alert and Trigger Telescope) and *SMT* (Slewing-Mirror Telescope). They coordinate the full operation of *UFFO*.

*UBAT* possesses a wide field of view (FOV) and serves as the primary trigger telescope responsible for the prompt emission observation. Benefited by the coded mask aperture camera scheme, once *UBAT* observes a GRB, it may determine the signal direction immediately and forwards the information to *SMT* for subsequent targeting. The key feature leads to *UFFO*'s ultra-fast optical detection is, *SMT* then adjust the lightweight SMS instantly to redirect the light path in the UV–optical telescope. Distinctive from the previous experiments, without steering around the entire telescope to target the signal, *SMT* requires merely  $\sim 10^{-1}$  sec. for the process, while performs the observation just fine as others.

## 2.2 CURRENT LIMIT OF GRB OBSERVATORIES' RESPONDING TIME

Because most of the  $\gamma$ -ray/X-ray detectors utilize the scintillator-fast photon detector pairs and directly trigger on the signals, the trigger-to-data-recording lags are considered negligible. On the other hand, experiments have been struggling for almost two decades to push the response limitations in UV–optical from days of *BeppoSAX* to minutes of *Swift*.

Some ground-based observatories such as *ROTSE* and *TORTORA* have demonstrated rapid responses about 20 sec. But being limited by their ground-based nature (weather, day/night...etc.) and the GCN trigger distribution time lag, [4] reports that the fast space-borne observatories like *Swift*, with its 30-cm-aperture *UVOT* responding at  $\sim 100$  sec., is in favor of the meters-large instruments. Reader may see from Fig. 2.2, *Swift-UVOT* is most likely starts its observation at  $\sim 100$  sec. after prompt triggers [5]. Even when the events start within a minute, it is seen from Fig. 1.27, the light curves usually have one or

## 2.3 UBAT

two data points before 100 sec.

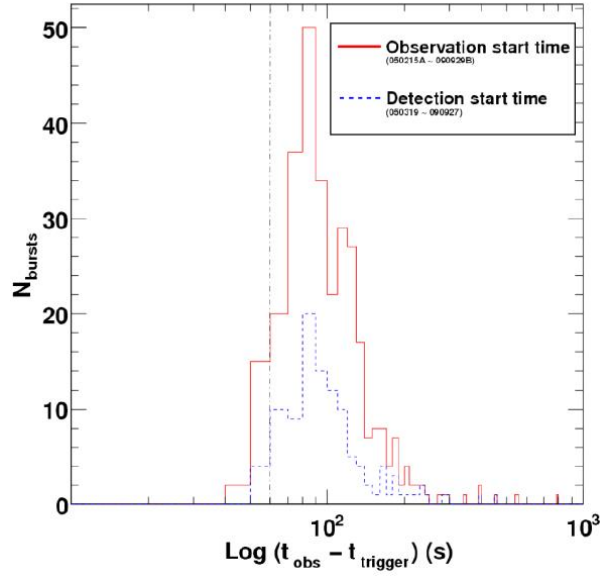


Figure 2.2: Statistics of *Swift*'s responding time. The vertical dashed line marks 60 sec.

The limitation of *UVOT* comes from the rotation of the entire instrument. The process requires not only a nontrivial lapse (20–27 sec.) for rotation, but also the additional time for acceleration, deceleration and stabilization, which is even longer than the rotation.

## 2.3 UBAT

### 2.3.1 Structural design

*UBAT* operates on the principle of *coded mask aperture camera scheme* similar to *Swift-BAT* [6]. The main components are: the coded mask, the hopper, the FS components and the electronics (Fig. 2.3 [3, 5]).

The coded mask is a  $\sim 400^2 \text{ mm}^2$  flat plate made with Tungsten-Tantalum alloy which can totally stop the photons in the energy range of *UBAT*. It's coded with a  $64 \times 64$ -pixels random pattern. Seeing from the photo, there are three types of transmittances coded by the pixels, the fully blocked, the unblocked and the Kapton tape. Fig. 2.4 illustrates the principle of the coded mask aperture camera scheme. When a GRB appears in the FOV of *UBAT*, the  $\gamma$ /X-ray photons project the pattern of the coded mask onto FS reflecting



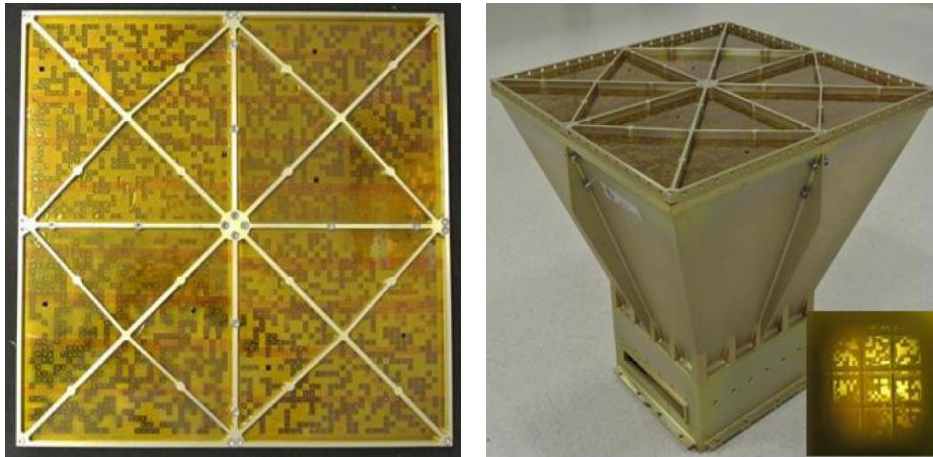
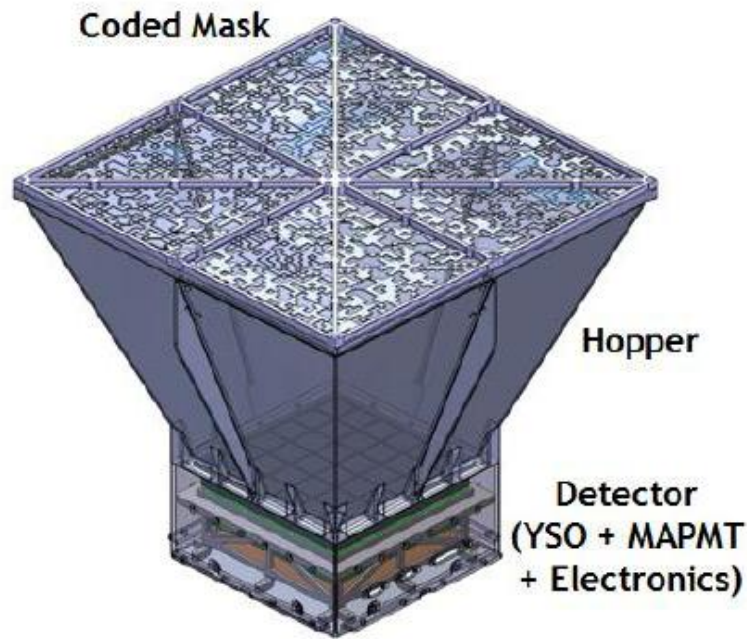


Figure 2.3: Schematics (top), topview (bottom left) and sideview (bottom right) of *UBAT*.

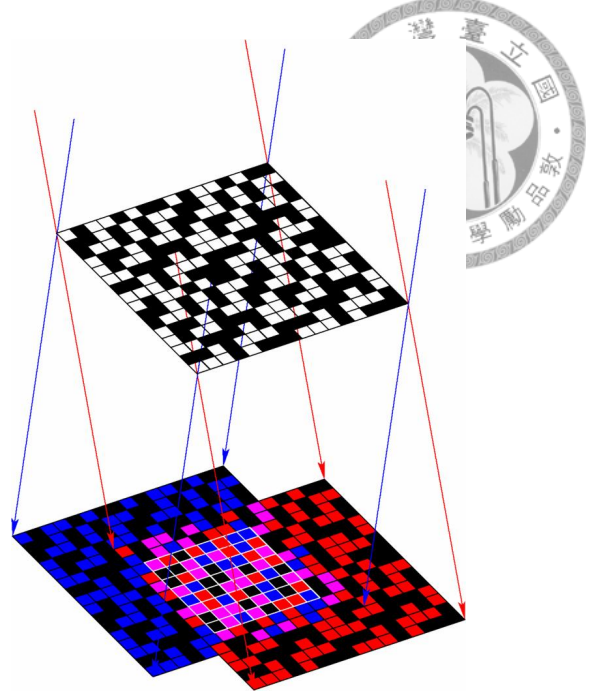
the different transmittances of the pixels. By comparing the pre-memorized mask pattern with the projection, *UBAT* can determine the direction of the event and deliver it to SMT for secondary targeting. *UBAT* is designated to trigger at  $7\sigma$  directional accuracy. To that end, it is required at least  $\sim 50\%$  the coded mask pattern is projected in the FS sensitive region. The requirement corresponds to the FOV  $1.83 \text{ sr}$  ( $\pm \leq 10''$  accuracy).

The hopper connects the coded mask and the detector box. The separation between the code mask and the FS is 280 mm. Tab. 2.1 summarizes the design of *UBAT*.



### 2.3 UBAT

Figure 2.4: An illustration to the principle of the coded mask aperture camera scheme. The black-and-white matrix on top is the coded mask, the projection plan at the bottom is the FS, where the blue and the red projections represent the full projected images of two events from the different directions. The white-lined matrix at the center of the FS represents the camera's sensitive region and bounds the legible parts of the projections. By comparing the pre-loaded mask pattern to the projections, the directions may be discerned. Note that as the incident angle rises, the legible fraction of the projection decreases [7].



Width (coded mask) (mm <sup>2</sup> )	400.8×400.8
Height (mm)	365
Weight (kg)	10
Structural material	W-Ta alloy
Coded mask/FS separation (mm)	280
Coded mask number of pixels	32×32×4 quadrants
Coded mask pixel size (mm <sup>2</sup> )	5.76×5.76
FOV (sr., deg.)	1.83, ±45.1° × ±45.1°
Angular resolution (")	≤ 10

Table 2.1: Structural specification of *UBAT*.

#### 2.3.2 Readout

*UBAT* electronics reads the MAPMT (Multi-Anode Photon Multiplier Tube) charge signals through two stages, the ASIC stage and the FPGA stage [8]. Fig. 2.5 shows an example of the readout.

In the ASIC stage, Preamp (Pre-amplifier) integrates the charges from 8 MAPMT pixels in the same row and performs the Q-T transformation<sup>2</sup>. The ASIC ships perform the threshold comparisons at 20 MHz and send the digitized counts-of-clocks to the FPGA. The count is called KI, which is regarded as the ADC (analogue-to-digital count)

<sup>2</sup>Outputting the signal whose duty time is proportional to the input charge. The Q-T transformation, as an example, may be achieved by outputting triangular signal whose height is proportional to the input charge.

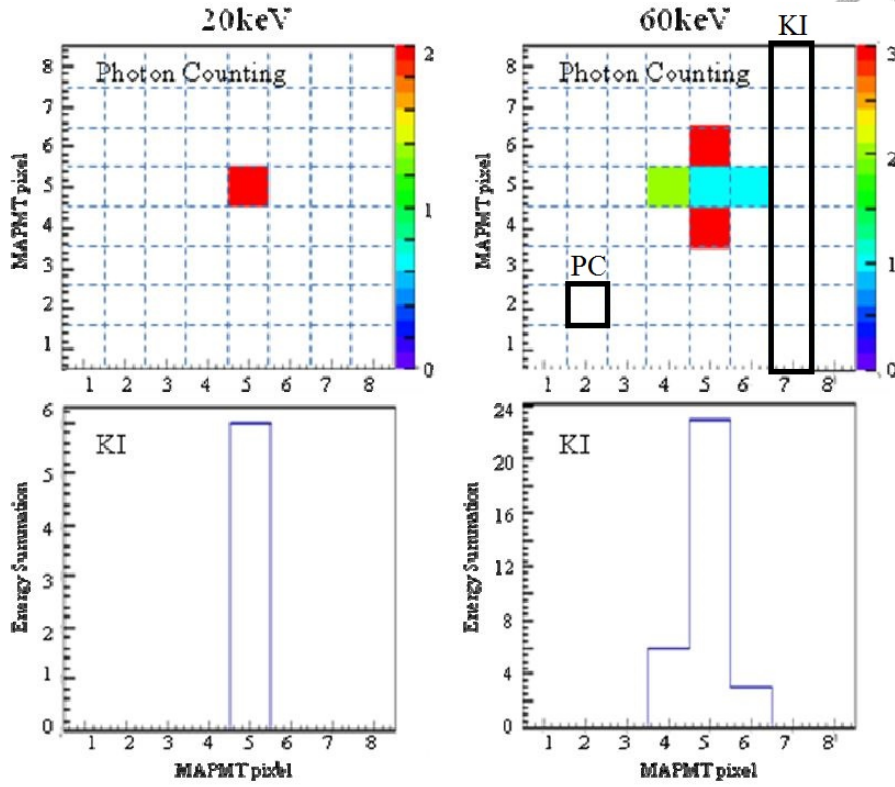


Figure 2.5: UBAT readout with radioactive  $\text{Am}^{241}$ . The radioactivity is collimated to the scintillator on top of pixel (5,5). One KI channel and one PC channel are marked as illustration. The 20 keV emission is shown at the left-handed panels, the 60 keV emission is shown at the right-handed panels. The upper two panels are the PC readings, the lower two panels are the KI readings. For more information, please refer to the corresponding paragraph.

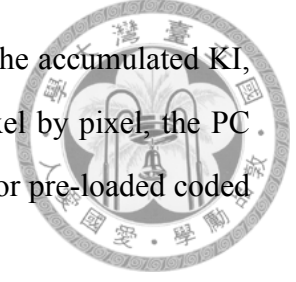
of MAPMT charge signal. For each  $8 \times 8$ -pixels MAPMT, there are 8 KI channels. In parallel with KIs, the ASIC also acquires unshaped charge pulses from individual MAPMT pixels and the last dynode (LD) to perform the PC (photon count) threshold comparisons. It's believed the calculation is fast enough and is suitable for single photon detection. To summarize, each MAPMT has 8 KI channels, 64 PC channels and 1 LD channel. All the thresholds of the 73 channels are set up independently in ASIC, and the threshold-exceeding counts are continuously transmitted to FPGA at 50 MHz.

UBAT FPGA handles the data processing and the mask pattern identification. To avoid the cross interference of the two tasks, they are handled by the separated *DATA\_FPGA* and *Trigger\_FPGA* FPGA chips. *DATA\_FPGA* operates on the rate trigger scheme. It continuously sums up all the input ADCs in each ASIC channel in the designate time



## 2.4 SMT

window. At the ending of every time window, *DATA\_FPGA* stores the accumulated KI, PC and LD counts to be a event frame. Since PCs are recorded pixel by pixel, the PC frame (or simply the PC “image”) is then passed to *Trigger\_FPGA* for pre-loaded coded mask pattern comparison and the signal direction determination.<sup>3</sup>



## 2.4 SMT

The main components compose *SMT* are the Slewing Mirror System (SMS), the Richey-Chretien telescope (RCT) and the Intensified Charge-Coupled Device (ICCD) readout. When *SMT* receives the GRB direction triggers, SMS slews the mirror to redirect the light to RCT. RCT observes the signals with ICCD readout in the UV–optical band. In this section, *SMT*- SMS, RCT and ICCD are introduced in series. Reader may refer to [2] for detail discussion.

### 2.4.1 Slewing Mirror System (SMS)

The reason the previous experiments required long time to target GRBs in UV/optical is they steered the entire instruments. Like which mentioned in 2.2, turning the massive telescopes around is usually a matter of hundreds kg or more. Due to the huge moments of inertia, the processes inevitably take long times to accelerate, rotate, decelerate, and stabilize.

What if the precess involves less than a kg or even grams? Fig. 2.6 explains the concept that achieves *SMT*’s ultra-fast response. Instead of steering the whole telescope, SMS slews its lightweight mirror to reflect the light path in to the stationary RCT. By means of the optical lever, the angle of rotation is halved, so is the rotation time. Also with the significant reduction in rotated mass, the time is also reduced in the acceleration, deceleration and stabilization. The active SMS concept may be further upgraded with MEMS technology. Fig. 2.6 also presents an example of the MEMS micro-mirror array [9, 10]. The one-piece flat mirror can be upgraded to an integration of the mirror-mirrors. The

---

<sup>3</sup>By the time this thesis is written, the exact length of the time window is undetermined. The possible choices are 1 msec., 100 msec. and 500 msec. The algorithm of distinguishing the truly illuminated pixels of MAPMTs, so-called the “hit finding”, is also under development.

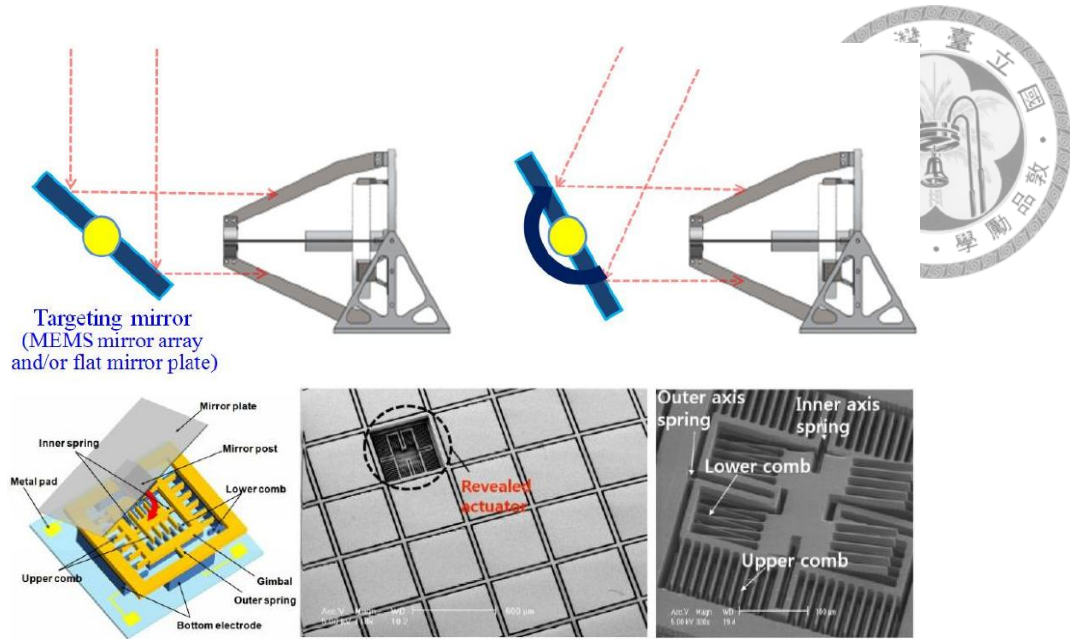


Figure 2.6: Top: An illustration of targeting by redirecting the light. The blue rectangular represents the mirror, the red dotted lines are the light paths, and the construction at the right-hand side is the telescope. Bottom: A MEMS-engineered micro-mirror array. On top of the array are the  $300\mu\text{m}$ -across micro-mirrors (central photo), beneath the mirrors are the 2-axes actuators (right-handed photo).

moment of inertia, in this case, should be negligibly small. Besides the impressive improvement in the responding time, the actuators beneath the micro-mirror may control the movement with spectacular accuracy.

As for a trial demonstration for the ultra-fast response, *UFFO-SMS* equips a 15 cm-diameter round flat mirror driven by the 2-axes motorized gimbal stage, which is expected to be capable of sweeping over the *UBAT*-FOV coverage in 1sec. Fig. 2.7 shows some photos of the *SMT* components. The 15 cm slewing mirror illuminates the full aperture of RCT on-axis,  $\sim 80\%$  off-axis, and reduces 57% weight with the honeycomb design. The final product is only 482 g yet proven robust to survive the space mission. All mirror surfaces are made of ZERODUR<sup>®</sup> substrate and coated with  $\text{SiO}_2$  for average reflectivity  $>85\%$ .

The 2-axes gimbal stage utilizes the step motors and rotary encoders whose minimal steps correspond to  $\sim 4''$ . The mirror is mounted on Axis-A (see Fig. 2.7), Axis-A is mounted on Axis-B which aligns with the optical axis of RCT. Using a closed-loop control in conjunction with the rotary encoders, the rotation control is precise to  $2'$ . Axes A and B rotate in  $+66.26^\circ$ — $-2.25^\circ$  and  $+22.25^\circ$ — $-21.47^\circ$ , respectively (+ marks the arrowed

## 2.4 SMT

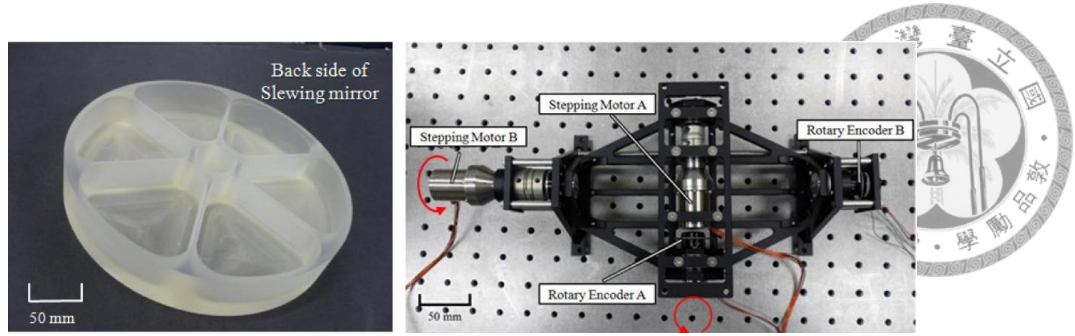


Figure 2.7: Left: *SMT*-SMS honeycomb mirror. Right: 2-axes *SMT*-SMS gimbal stage.

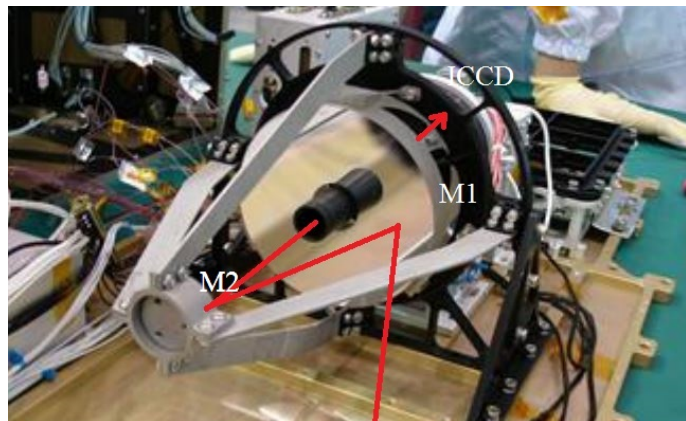
direction in Fig. 2.7). The rotation allows a full  $\pm 35^\circ$  sky coverage. The total mass of SMS is 1.85 kg.

SMS requires about 1.5 sec. to slew end-to-end over the  $\pm 35^\circ$  sky coverage. The absolute angular accuracy of targeting is  $2.56'$ . Additional 340 msec. and 110 msec. are needed to stabilize Axes-A and -B to the RCT-ICCD imaging resolution. Current SMS takes  $\sim 1.6$  sec. on average to complete the targeting procedure. Through optimizing the motorizing algorithm (may be install before launch or on-flight), 1 sec. responding time is expectable.

### 2.4.2 Richey-Chretien telescope (RCT)

Fig. 2.8 presents the *SMT*-RCT. *SMT*-RCT is equipped with a 100 mm-diameter primary mirror and a 20 mm-diameter secondary mirror, the distance between is 130 mm. RCT has 1.14 m effective focal length and a  $17' \times 17'$  FOV. A thorough simulation and test work were also performed to guarantee the delicate telescope is robust enough for the space mission.

Figure 2.8: The photo of *SMT* RCT with it primary mirror (M1), secondary mirror (M2) and ICCD noted. The red line illustrates the light path.





### 2.4.3 Intensified Charge-Coupled Device (ICCD)

ICCD is the composite photon detector deploys the intensifying micro-channel plate (MCP) in front of the traditional CCD photon detector. Fig. 2.9 shows the schematics and photos of the MCP phosphor intensifier [11]. A photocathode is on the input window of the intensifier to convert the incident photon to the electron<sup>4</sup>. The photoelectron is accelerated by an external field about 1000 V across the MCP channel. While traveling in the MCP, the photoelectron constantly bombards the inner wall of the MCP. Since the MCP is made of dynode materials, whenever the electron(s) strikes the wall, more secondary electrons are emitted, as shown in the figure. After traveling through the MCP (typically 0.1–1  $\mu\text{m}$  in thickness), the number of electrons is amplified by  $10^3$ – $4$ . Then the electric current is subjected to the phosphor screen, which provides another factor of  $\sim 1000$  amplification and turns the electrons back into CCD-detectable photons. The MCP feeds the phosphorous photons to the CCD array pixel by pixel with the micro-channels.

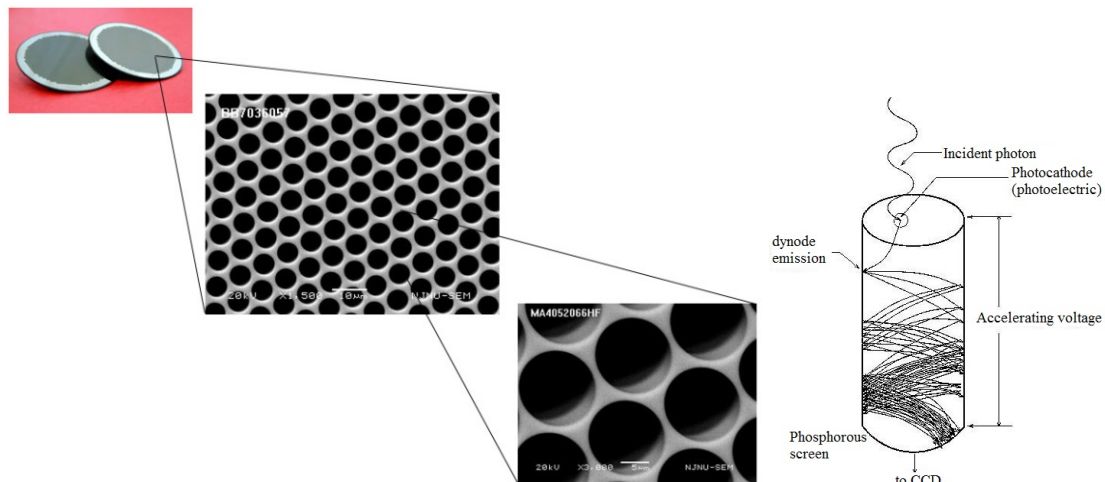


Figure 2.9: An example of MCP. The micro-channels in the left-handed photo are about 5  $\mu\text{m}$  in diameter. The right-handed sketch illustrates the amplification principle of phosphorous MCP.

*SMT* is equipped with the ICCD sensor Kodak CCD KAI-0340. The sensitive range is 200–650 nm. It operates in the Geiger mode<sup>5</sup> at the gain  $\sim 10^6$  and can observe faint

<sup>4</sup>See 4.1 for more informations about the characters shared by MAPMTs, e.q. photocathode, photoelectron acceleration, dynode....

<sup>5</sup>A semiconductor is said to be in Geiger mode when a slight reverse voltage is applied to the junction. When the forward avalanche or intensified pulse current overcomes the reverse voltage, it is registered as one (photo-)electron pulse. The strength of a signal is measured by the number of pulses. Geiger mode is

## 2.5 *UBAT focal surface*

objects up to 19.14 mag. B-star in white light for 100 msec. To guarantee the image quality, only the central  $256 \times 256$  pixels are used over the  $640 \times 480$  pixels. each pixel corresponds to  $4'' \times 4''$  and thus defines the angular image resolution of SMT. The physical MCP area maps to the employed pixels is  $\sim 15 \times 15 \text{ mm}^2$ . *SMT* ICCD reads at the frame rate 250 fps.

## 2.5 UBAT FOCAL SURFACE

UBAT FS is composed of 36 assemblies of the YSO scintillator arrays and MAPMTs (Fig. 2.10). The assemblies are frequently addressed as the (*UBAT* FS) detection units in this thesis. Each scintillator array is attached to MAPMT by EPO-TEK<sup>®</sup> 301-2 silicon optical adhesive. The detection units are connected to *UBAT* ASIC board in a  $6 \times 6$  arrangement. The effective area of detection is  $13.82 \times 13.82 \text{ cm}^2 = 191.1 \text{ cm}^2$ .

In the following sections, I firstly introduce the YSO scintillator, then the *UFFO* MAPMT, both with detail informations which are frequently mentioned through this thesis. The characteristics and the usage of the optical couplant is summarized in the end.

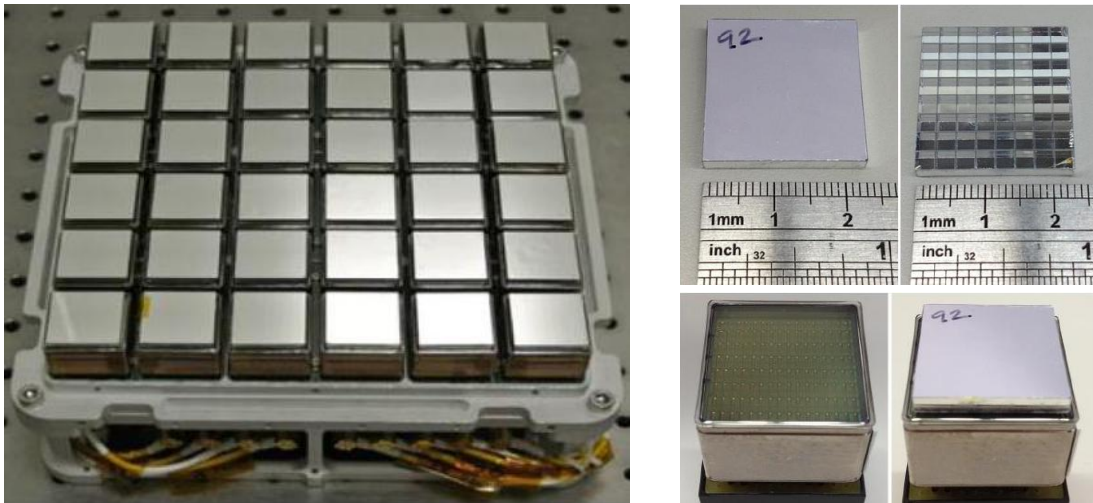


Figure 2.10: The left-handed photo presents the complete construction of UBAT FS and the electronics. The detection units forms a  $6 \times 6$  matrix. The four right-handed photos, from top-left, top-right, bottom-left to bottom-right present the back side of the scintillator, the front side of the scintillator, the MAPMT and the assembled detection unit. Dimensions may be inferred from the reference shown.

---

especially suitable for weak signal detection.





### 2.5.1 YSO scintillator array

The scintillator array is an  $8 \times 8$  integration of  $64 \text{ } 2.68 \times 2.68 \times 3 \text{ mm}^3$  Cesium-doped Yttrium Oxyorthosilicate (YSO,  $\text{Y}_2\text{SiO}_5 : 0.2\%\text{Ce}$ ) crystal cubes. To enhance the collectivity of the scintillation photons and improve the imaging quality,  $200 \text{ }\mu\text{m}$  3M VM2000 dielectric mirror reflector films are attached between the crystal cubes. A  $70 \text{ }\mu\text{m}$  VM2000 covers the entire non-MAPMT-coupling surface. The scintillator is designed to match the pixel geometry of MAPMT; each YSO crystal cube aligns its corresponding MAPMT pixel at the center as being coupled. Fig. 2.11 summarizes the geometry of the scintillator array. Tab. 2.2 lists the characteristics of the YSO crystal<sup>6</sup>.

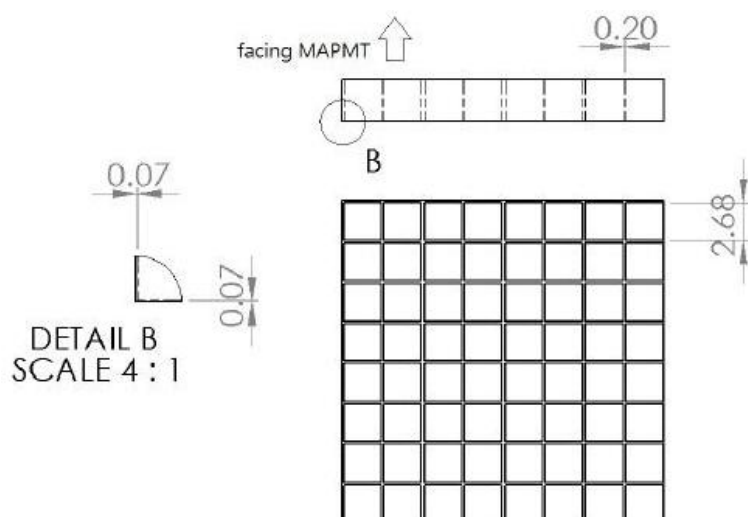


Figure 2.11: The schematics of the YSO scintillator array. The unit is mm.

Specific gravity ( $\text{g}/\text{mm}^3$ )	4.45
Peak scintillation (nm)	400
Index of refraction (@ 400 nm)	1.8
Scintillation time constants (nsec.)	35 [12]
Photon yield ( $\gamma/\text{keV}$ )	9.2 [13]

Table 2.2: The specification of *UBAT* YSO crystal.

<sup>6</sup>Items without the references mentioned are provided by the manufacture.

## 2.5.2 MAPMT

The success of *SMT* targeting is sensitive to the accuracy of the event direction delivered by *UBAT*. In order to determine the direction with the high accuracy, it's crucial the *UBAT* FS identifies the coded mask projection in high resolution and certainty. To this end, *UBAT* utilized the latest model of MAPMTs specialized for the imaging proposes in space scientific missions. The chosen model is Hamamatsu-R11265-03-M64. It is developed from the widely-applied model R7600. The *UFFO* collaboration has demonstrated the *UFFO* observatory, including the delicate MAPMTs and other optical components, will survive the launch and the space environments. The test includes the thermal vacuum, shock and vibration tests was performed at *NSPO* (*National Space Project Organization*), Taiwan in August, 2011 [5].

Window geometry (mm <sup>3</sup> )	26.2 × 26.2 × 0.8
Window material	Hamamatsu UV glass
Pixel arrangement	8 × 8
Pixel size (mm <sup>2</sup> )	2.88 × 2.88
Pixel material	Hamamatsu Super-Bialkali
Pixel gapping	None
Operation high voltage (V)	900

Table 2.3: The specification of *UBAT* MAPMT.

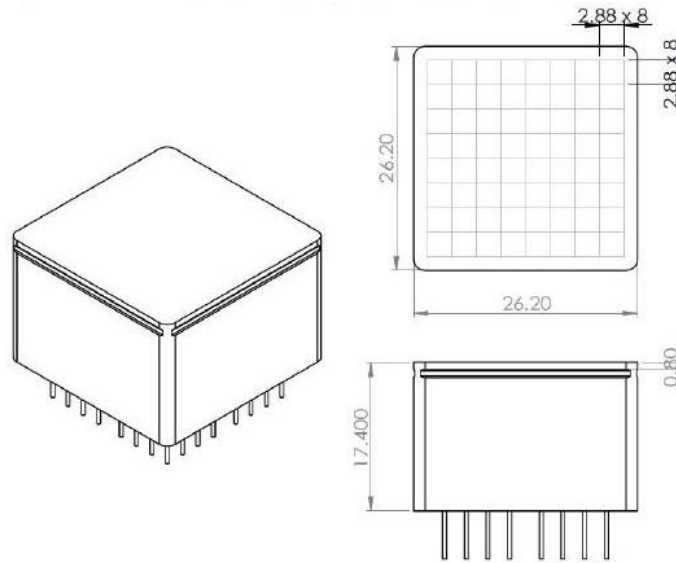


Figure 2.12: The schematics of *UBAT* MAPMT. The unit is mm.

Tab. 2.3 lists the parameters of *UBAT* MAPMT. It has two special features:

1. *UBAT* MAPMT doesn't implement any insensitive gaps between the photocathode material of each pixel. This modification of its predecessor not only enlarges the packing factor of the sensitive region by about 30%, but also makes the imaging quality even on the whole surface. *UBAT* MAPMT is expected to have better sensitivities, energy-wise and spatial-wise.
2. *UBAT* MAPMT equips the newly developed photocathode compound. The Quantum Efficiency (QE) of the old model is  $\sim 25\%$  at the YSO scintillation peak; the QE of *UBAT* MAPMT, on the other hand, is  $\sim 35\%$  (Fig. 2.13).

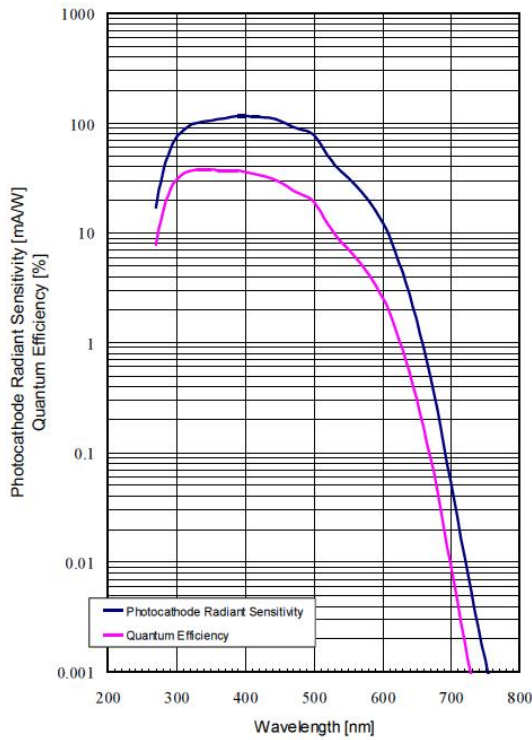


Figure 2.13: Quantum Efficiency of *UBAT* MAPMT.

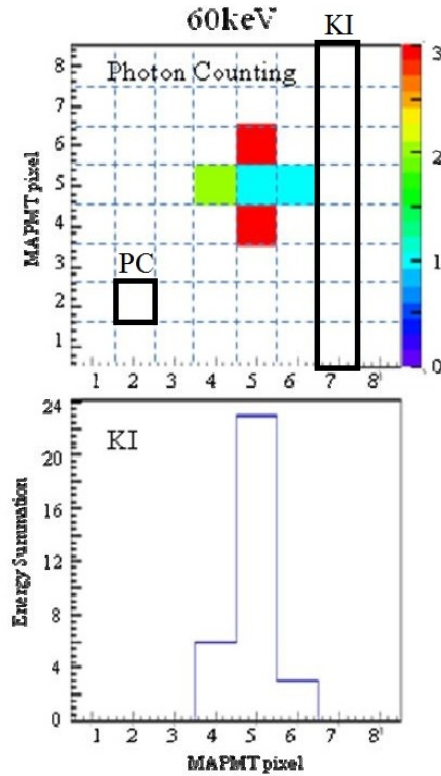


Figure 2.14: The preliminary calibration result of  $\text{Am}^{241}$ .

Despite the improvements mentioned above, the preliminary tests indicated the detection unit could observe the scintillations with quite nontrivial crosstalk. Readers may refer to the result of 60 keV  $\text{Am}^{241}$  calibration presented in Fig. 2.14<sup>7</sup>. When only one crystal cube in the scintillator is illuminated by the 60 keV X-ray, the PC image shows a obvious

<sup>7</sup>copied from Fig. 2.5, discussion is given in the original figure.



## 2.5 *UBAT focal surface*

cross pattern of 1 count in the correct pixel but 2–3 counts in the nearby pixels. In its KI histogram, although the peak occurs in the correct channel, the close by channels both show about 30% signal detections. Recall it was mentioned in 2.3, *UBAT* requires at least half the coded mask being identified in PC with perfect certainty, i.e. perfectly discriminating the corresponding MAPMT pixels of the X-ray-photon illuminations on the FS, so the trigger algorithm may determine the signal directions at  $7\sigma$  confidence level. The signal crosstalk may significantly reduce the certainties of the mask pattern identification, the direction calculation, and results in a catastrophic failure in the *SMT* operation.

### 2.5.3 Optical couplant

Each scintillator and MAPMT are coupled tightly by the epoxy optical adhesive EPO-TEK<sup>®</sup> 301-2, which is specially approved for space usages by *NASA* and *RKA*. The couplant has transmittance  $> 99\%$  in the optical band and the refractive index 1.5115 under living condition [14].

Throughout this thesis, all the optical components are coupled by Dow-Corning<sup>®</sup> Q2-3067 optical grease of refractive index 1.47–1.48 in the optical band. The properties of the optical grease can be found in [8].



## Bibliography

- [1] Liu, T.-C. 2010, *UFFO Project in Taiwan*, the website of LeCosPa center (lecospa.ntu.edu.tw)
- [2] Jeong, S., et al. 2013, *Opt. Exp.*, 21, 2, 2263
- [3] Lee, J. 2013, *Gamma-ray Bursts: 15 Years of GRB Afterglow*, *EPS Publ. Seri.*, 61, 525
- [4] Roming, P., et al. 2005, *Spa. Sci. Rev.*, 120, 95
- [5] Park, I. H. 2013, *New J. of Phys.*, 15, 023031
- [6] Barthelmy, S. D., et al. 2005, *Spa. Sci. Rev.*, 120, 143
- [7] Turler, M. 2005, *Image gallery, iSDC website* (<http://www.isdc.unige.ch/>), Univ. Geneva
- [8] Kim, J. E., et al. 2012, *Proc. of SPIE.*, 8443, 84432V-1
- [9] Park, I. H. 2004, *Nucl. Phys. B*, 134, 196
- [10] Park, I. H., et al. 2009, *arXiv*, 0912:0773
- [11] Photos copied from the website of **tectra** GmbH Physikalische Instrumente ([www.tectra.de](http://www.tectra.de))
- [12] Ruthfuss, H. E., et al. 2007, *IEEE-NSS*, N24, 196
- [13] Beringer, J., et al. (Particle Data Group) 2012, *Phys. Rev. D*, D86, 010001

## *BIBLIOGRAPHY*

[14] The technical data sheet of EPO-TEK<sup>®</sup> 301-2 ([www.epotek.com](http://www.epotek.com))

[15] The technical data sheet of Dow Corning Q2-3067 ([www.dowcorning.com](http://www.dowcorning.com))





## CHAPTER 3

# EXPERIMENTAL DESIGN

In this chapter, the preparation work, includes the experimental environment and the apparatus layout, is introduced in 3.1. The DAQ (data acquisition) system developed by *NuTel* experiment was utilized for the work of this thesis. The design and the calibration of *NuTel* DAQ are reported in 3.2. In 3.3, an overview of the research plan is provided in the logical sequence. Finally, the expected result of each experiment discussed in 3.3 is estimated in 3.4.

### 3.1 PREPARATION

All the experiments in this thesis were conducted in the laboratory environment under normal atmospheric pressure, 23°C and 50–53% relative humidity. Every contact interface between the optical components, e.g. MAPMT, scintillator and light guide, was coupled by Dow-Corning® Q2-3067 optical couplant. The couplant was 50–100  $\mu\text{m}$  in thickness.

A  $25 \times 25 \times 180 \text{ cm}^3$  completely light-sealed aluminum cabinet was prepared for the experiments involved sensitive photon detectors. The interior and the fixtures were covered by black flannel blanket to eliminate any reflections. The calibration sources, e.g. LED, radioactive sources...etc., were situated 80–160 cm away from the detectors. Assuming the point-like calibration sources, the divergent angles of the illuminations were  $\pm 0.4^\circ - \pm 0.7^\circ$  in the frontal area of *UBAT* detection unit.

## 3.2 NuTel DAQ

### 3.2.1 Design

The DAQ system developed by *NuTel* experiment was utilized in this thesis to acquire the MAPMT signals. The DAQ system was composed of the analogue pre-amplifier (Preamp) and FPGA (field-programmable gate array) data collection module (DCM) [1].

### Preamp

Preamps were designed with the charge-sensitive circuits and connected to MAPMT outputs directly. Each Preamp board had 16 channels, so one 64-pixels MAPMT was handled by 4 Preamps. Fig. 3.1 is the one-channel layout of Preamp circuit [2].

The 1<sup>st</sup> stage of the circuit (left-handed part in Fig. 3.1) utilized a charge-sensitive R-C circuit and was responsible for integrating and reshaping the nanoseconds MAPMT charge pulses. The R-C circuit integrated the charge and discharged in the form

$$V \propto e^{-t/\tau} \quad (3.1)$$

$$\tau = R8 \times C9 \sim 187\text{nsec.}$$

The time constants of every Preamp channel were calibrated individually to 0.01 nsec.;  $\tau$  fluctuated about 10%.

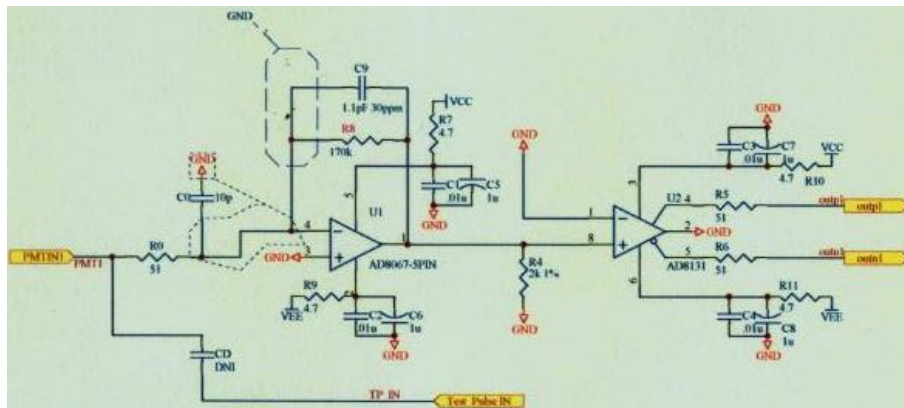


Figure 3.1: The one-channel layout of *NuTel* Preamp circuit. The main circuit (left-handed part) was a virtual-short R-C circuit with  $R8 = 170 \text{ k}\Omega$ ,  $C9 = 1.1 \text{ pF}$ , shaping time  $\sim 187 \text{ nsec.}$

The 2<sup>nd</sup> stage (right-handed part in Fig. 3.1) utilized the differential Op-amp (operational amplifier) and served as the noise rejection. The differential Op-amp subtracted the reshaped signal from the 1<sup>st</sup> stage with the common ground signal. The electronic noise in Preamp was less than 8 mV.



## DCM

DCM digitized and stored the analogue Preamp signals. It was composed of 40-MHz, 32-channels cPCI FPGAs. Each DCM FPGA connected to 2 Preamps and digitized 2000 mV signal by 10 bits, i.e.  $1 \text{ ADC} \cong 2 \text{ mV}$ ,  $1 \text{ clock} = 25 \text{ nsec}$ . The system was built to have the maximal capacity of simultaneously taking data from up to 512 Preamp channels/MAPMT pixels (2 chassis setup) [3].

In one chassis, one DCM board served as the “Master” and regulated the others via the daisy chain. Once a channel was trigger, the trigger requisition was passed down sequentially to the master. The master then sent an universal data acquisition to each in the chassis so the data in the buffer ram was transported to the hard disc. In practice, in order to locate the trigger-time data in the buffer ram, the user should specify the time delay of the master in the configuration file. Receiving signals took 4 clocks, sending the universal data acquisitions took 24 clocks. So the rewind should be 24 or 28 clocks, depended on the trigger was issued from the master itself or the slaves, respectively. In case the trigger threshold rejected some weak leading signals, it was suggested to rewind 2 more clocks, so the common setting of delay became 26 or 30 clocks.

To discriminate expected signals, the trigger threshold must be specified channel by channel in the configuration file. The DCM firmware calculated the charge accumulation in every channel every clock by

$$\begin{aligned}
 Q_i &= ADC_{i-1} - e^{-25/187} \times ADC_i \\
 &\cong ADC_{i-1} - 0.875 ADC_i
 \end{aligned} \tag{3.2}$$

, where  $i$  denoted the trigger clock. Whenever  $Q_i$ s exceeded the designated thresholds,

### 3.2 NuTel DAQ

DCM boards issued triggers. In principle, if DCM observed distinctive signals at  $i^{th}$  clock and no additional charges came in afterward, it observed the  $e^{-t/187}$  discharging tails in later clocks and Eqn. 3.2 gave all  $Q_{later} = 0$ .

One event frame of NuTel DAQ contained 8-clocks information, 200 nsec. signal. One could reconstruct the total accumulated signal charges by

$$Q_{tot} = \sum_{i=1}^8 Q_i \quad (3.3)$$

$$= \sum_{i=1}^8 ADC_i - e^{-25/\tau} \times ADC_{i-1} \quad (3.4)$$

, where  $\tau$  of each channel had been calibrated accurately. DCM firmware was implemented with the approximated equation of Eqn. 3.2 for trigger identification and Eqn. 3.3 was applied in the off-line analyses. The charge reconstruction with Eqn. 3.3 was linear in 0 mV–3250 mV. The rates of event losses were less than 2% and 6.4% at 1000 Hz and 1500 Hz total trigger rates, respectively.

#### 3.2.2 Calibration

The DAQ pedestal, i.e. voltage biases either in Preamps or DCM, could result in non-zero  $Q_i$ s when no signal was observed and biased the reconstructions when signal levels and the pedestal were comparable. According to [4], the main cause of the pedestal was the programmable potentiometers in DCM which caused constant biases.

The method of pedestal calibration was:

1. I Set up the trigger masks for all channels which were used by MAPMT, which prevented the DAQ being triggered by any spontaneous signals.
2. The DAQ was then triggered from another channel which was not connected to MAPMT by the stable oscilloscope-generated pulses at 100 Hz. DAQ took data in all the channels when triggered. The trigger scheme of masking all MAPMT channels and triggering by the oscilloscope is called the *external/force trigger scheme* in this thesis.

3. I averaged totally 1000 triggered events (8000 pedestal readings in each channel) to be the calibrated pedestals. The database was implemented for pedestal subtraction,

$$Q_{i, \text{ applied to Eqn. 3.2 and Eqn. 3.3}} = Q_i - \text{pedestal} \quad (3.5)$$

,in both the on-line trigger firmware (in integer ADCs) and the off-line analyses (in floats).

As a result, the pedestal in each channel ranged in 0–10 ADC and fluctuated by  $\leq 1$  ADC. The calibrated  $Q_{tot}$  showed trivial baseline deviation from 0 mV and RMS  $\leq 0.5$  mV in non-triggered channels.

As reported in 3.2.1, the intrinsic noise level of Preamp was  $< 8$  mV , and the pedestal fluctuation was less than 1 ADC. Once the pedestal calibration was carried out, I designated 5 ADC ( $\sim 10$  mV) to be the thresholds in all channels for all the later experiments. The trigger scheme of DAQ being triggered freely from every channel with the threshold 5 ADC is called the *self trigger scheme* in this thesis. The DAQ-noise trigger rate of the 64 MAPMT-connected channels was less than  $10^{-2}$  Hz under the self trigger scheme<sup>1</sup>.

### 3.3 EXPERIMENTAL METHOD

The propose of this section is to demonstrate the general logic of this study. Readers may find the details covered in the noted chapters/sections. The method of this study is as follow:

0. The MAPMT was firstly connected to 770V and left standing in the light-sealed cabinet for 1 hr. to deplete the agitated electrons in the MAPMT. This treatment is called the “baking” process in this thesis.
1. The MAPMT spontaneous emissions, so-called the dark current, were measured in 64 channels under self-trigger scheme. The signal was single-(MAPMT-)photoelectron (PE) dominant and was regarded as the instrumental background of the study. The

<sup>1</sup>When the electronics was float but connected to a MAPMT.



### 3.3 Experimental method

system gain was defined as  $Q_{tot}/PE$ . From the result I roughly estimated the channel gains of the MAPMT-DAQ system. (4.2)

2. The gains were accurately calibrated with the LED illumination through the photon counting method, the gain and the number of PE (#PE) emitted in each channel were determined by theoretical fit. The DAQ operated under the force-trigger scheme for a better noise rejection. The calibrated gains were in consistent with the estimation in 1. With the gains calibrated, the signals observed in the later experiments were all converted into #PE. (4.3)
3. I attached the scintillator to MAPMT and recorded the scintillations under the self-trigger scheme. Most of the scintillation events were identified as the cosmic ray events and vetoed. The cosmic-ray-free signal was considered to be the detection-unit background of this study. (5.1)
4. The energy scale of *UBAT* detection unit was calibrated by seven radioactive sources in the range 8 keV–60 keV. In this experiment, a collimator was applied to guide the X-ray photons to a central YSO cube, and the trigger scheme was self trigger but disabling the triggers from all the non-collimated channels, i.e. data in all channels were taken only when the central channel passed triggers. The calibration established the photoelectron yield (#PE/keV) and the linearity of *UBAT* detection unit. It also quantified the crosstalk which had been observed in the preliminary test<sup>2</sup>. The trigger scheme is called the *collimated trigger scheme* in this thesis. (5.2 & 5.3)
5. To further resolve the crosstalk issue and search for the possible solutions, I constructed a Geant 4-based simulation package of the detection unit. The simulation reproduced the result in 4 and indicated the reflections occurred at the MAPMT photocathode as the cause of the crosstalk. (Ch. 6)
6. Based on the mechanism of the crosstalk resolved in the simulation, I proposed the idea of Inverted-Conical light guide as a possible solution to the crosstalk smearing. The purpose was to reduce the crosstalk and enhance the scintillation detection in the

---

<sup>2</sup>See 2.5.2

channel correctly conjugated to the X-ray-deposited crystal cube, e.q. in the central channel according the collimated trigger scheme. The geometry of the Inverted-Conical Light Guide was optimized in the simulation and a test sample was fabricated. The energy/crosstalk calibration in 4 was repeated with the Inverted-Conical Light Guide. An ameliorative result was reported. (Ch. 7)

In the following content the MAPMT pixels, their corresponding DAQ channels and YSO cubes in the scintillator matrix are addressed as ch. (number). The naming of the 64 channels are in Fig. 3.2.

7	8	23	24	39	40	55	56
6	9	22	25	38	41	54	57
5	10	21	26	37	42	53	58
4	11	20	27	36	43	52	59
3	12	19	28	35	44	51	60
2	13	18	29	34	45	50	61
1	14	17	30	33	46	49	62
0	15	16	31	32	47	48	63

Figure 3.2: The naming rule of the 64 MAPMT channels used in this thesis.

### 3.4 SIGNAL YIELD ESTIMATION

The light yield of YSO crystal was  $9.2 \gamma/\text{keV}$ , and the attenuation was negligible at the YSO peak frequency (400 nm). Accurate spectra implemented in the simulation is provided in 6.1.

It was reported in [5, 6, 7] VM2000 exhibited the reflectance 0.9–0.95 . Since the reflector/crystal cell was tiny, the scintillation photons were expected to be reflected a few times. The reduction factor due to the reflectance of VM2000 was estimated 0.7–0.9.

The 10-mm transmittance of Q2-3067 optical grease is 73% at 400 nm [8]. Assuming constant attenuation, the transmittance of the  $100\text{-}\mu\text{m}$  coupling layer was  $0.73^{0.1/10} > 0.996$ . The attenuation of the couplant was simply omitted.

### 3.4 Signal yield estimation

The transmittance of the Hamamatsu UV-transmittance type glass window was  $\sim 0.91$  [1]<sup>3</sup>. The Quantum Efficiency was  $\sim 0.35$  at 400 nm. The cathode radiant sensitivity was omitted ( $>0.999$ ). The first dynode sensitivity was estimated by the MAPMT Hamamatsu R8900 series, which was another descendant model of R7600 like *UBAT* MAPMT. The first dynode sensitivity taken was 0.5(perimetric pixel)–0.75(central pixel) [10]. The dynode amplification was estimated by which of Hamamatsu R7600 at 800V  $\sim 3 \times 10^5$ .

So the expected signal yield of 1 keV scintillation was estimated by

$$\begin{aligned}
 Q_{tot} = & 9.2(\text{photon yield}) \times 0.7(\text{VM2000}) \times 0.91(\text{glass window}) \\
 & \times 0.35(\text{QE}) \times 0.75(1^{\text{st}} \text{ dynode}) \times 3 \times 10^5(\text{dynode amp.}) \\
 & \times \frac{1.6 \times 10^{-19} \text{ C}}{1.1 \text{ pF}} \\
 \cong & 70 \text{ mV/keV}
 \end{aligned} \tag{3.6}$$

The estimation implied the full DAQ range 3200 mV corresponded to  $\sim 50$  keV. To match the dynamic range of DAQ to the full 5–150 keV range of *UBAT*, I could adjust the high voltage of MAPMT in 600–1000 V, which brought in another factor 0.1–10 and made the range easily satisfied. In other word, *NuTel* DAQ was suitable for the calibration of *UBAT* FS.

---

<sup>3</sup>Fig. 4-5 of the ref.



## Bibliography

- [1] Yeh, P., et al. 2004, *Mod. Phys. Lett.*, A19, 1117
- [2] Huang, K.-X. 2007, *master thesis*, Phys. Dept., N. T. U. (unpublished)
- [3] Velikzhanin, Y. S., et al. 2006, *Nucl. Inst. and Meth. A*, 552-3, 477
- [4] Chang, C.-P. 2011, *master thesis*, Phys. Dept., N. T. U. (unpublished)
- [5] Janecek, M., et al. 2008, *textitNucl. Sci., IEEE Trans.*, 55-4, 2432
- [6] Steinbuegl, F., et al. 2001, *Proc. of ICRC 2001*, p. 912
- [7] Weller, M. F., et al. 2000, *Science*, 287, 2451
- [8] The technical data sheet of Dow Corning Q2-3067 ([www.dowcorning.com](http://www.dowcorning.com))
- [9] Hamamatsu Photonic K. K. editorial committee 2006, *PHOTOMULTIPLIER–Basics and Application*, 3<sup>rd</sup> ed.
- [10] Kawasaki, Y., et al. 2006, *Nucl. Inst. and Meth. A*, 564, 378

## *BIBLIOGRAPHY*





## CHAPTER 4

# UBAT MAPMT - HAMAMATSU R11265

### 4.1 REVIEW OF CONVENTIONAL MAPMTS

MAPMT is the common abbreviation of the Multi-Anode PMT (Photomultiplier tube), i.e. one photo-tube with many separate PMT channels. Fig. 4.1 illustrates the construction of a typical single channel PMT [1]. PMTs are the vacuum tubes operate at the typical high voltages  $\sim 1000$  V and multiply very dull light signals to detectable charge signals.

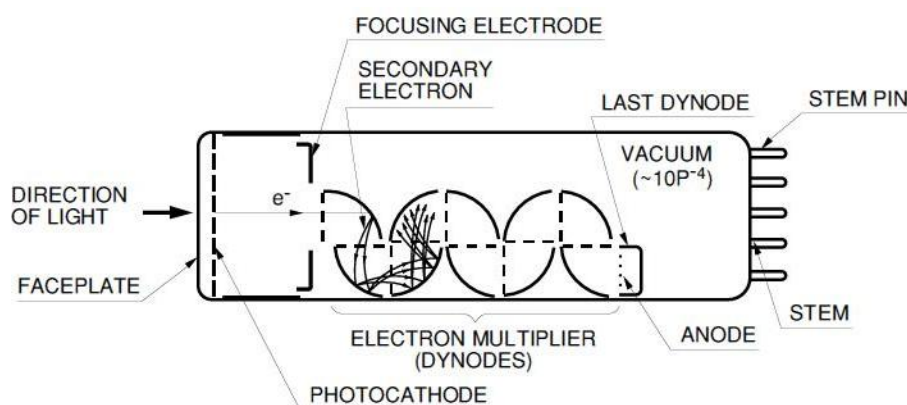


Figure 4.1: The schematics of a single channel PMT.

When the light illuminates MAPMT, the photons transmit through the frontal window and trigger the photoelectric effect at the photocathode which is coded on the inner side of the window. The typical photocathode is a tens-nanometers-thick evaporated layer of the alloys of group-1A, 2A and 3A elements such as Sb, Rb, Cs, K, Ga...etc. These alloys are mostly sensitive in the range of the visible light, while some are also applicable in short IR and long UV.

#### 4.1 Review of conventional MAPMTs

The photoelectric efficiency of the photocathode is called the Quantum Efficiency (QE). In principle, it is a dependent of the wavelength, incident angle, polarization of the illumination.<sup>1</sup> For the sake of simplification, conventional single-value QEs are defined upon unpolarized, normal incident lights. It is shown in Fig. 4.2 commercially-available QEs usually peak in  $\sim 300\text{--}500\text{ nm}$  with the values  $0.25\text{--}0.3$ .

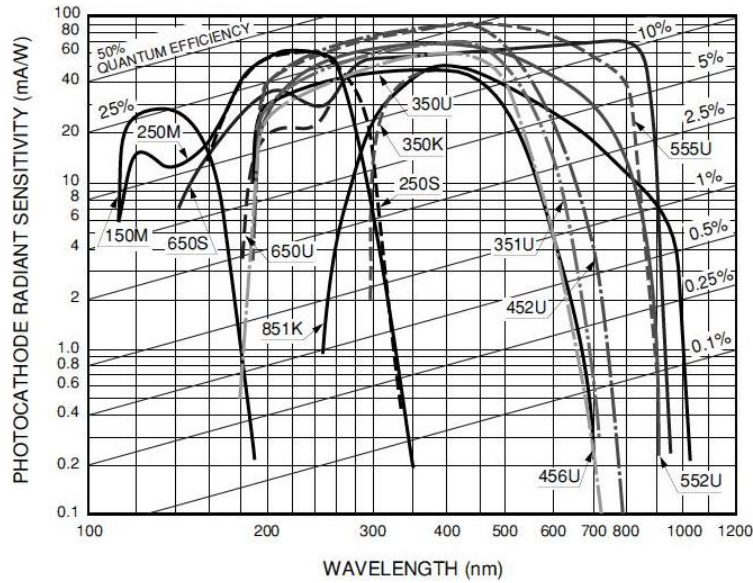


Figure 4.2: Quantum efficiencies of some commercial photocathode compounds. U452 and U552 denote the most common types Bialkali and Multialkali, respectively. [1]

There are two methods to guide the PEs drifting through the vacuum tube and being collected by the dynode for subsequent amplification. MAPMT may either utilizes special structures for passive collections or actively focusing them with the external fields. While the characteristic times of photocathode photoelectric effects are short, different collecting mechanisms may result in distinctive MAPMT performances, e.q. pulse width, sensitive area, linearity...etc.

Once PEs arrives at the 1<sup>st</sup> dynode, the dynode multiplies the number of the electrons by 1–3 OM and hands them to the next dynode. The process proceeds as electrons being multiplied and passed down through many dynode stages. Fig. 4.3 illustrates the “snowball” Dynode process. One can easily imagine how gigantic the amplification would be if the current is passed down through 10 dynodes. Also presented in Fig. 4.3 is the amplifica-

<sup>1</sup>These variables must all be specified in a realistic simulation of MAPMT. Further discussion is provided in 6.2.

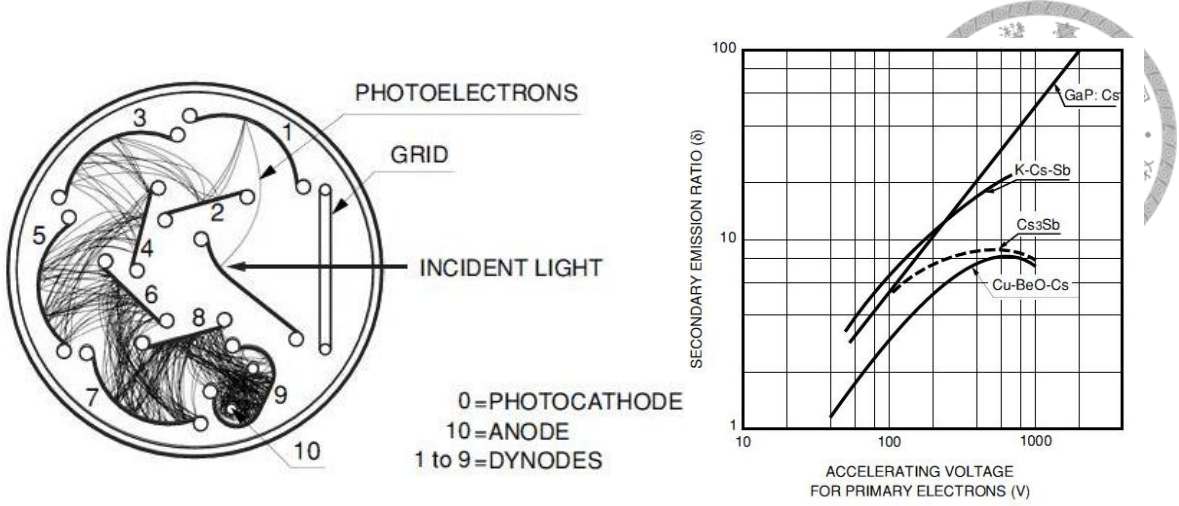


Figure 4.3: left: A illustration of the Dynode process. The thin faded lines represent the electron paths. right: Dynode amplifications versus applied voltages. The relation is obviously power-law linear. [1]

tion of a single dynode stage to the applied voltage. The typical dynode is a substrate electrode made of Nicole or stainless steel and coated with Alkali Antimonide(Sb)/Oxide(O). When an electron strikes the dynode with kinetic energy  $E_k$ , the amplification  $g$  is described by

$$g_i = k_i \Delta V_i^{a_i} = k_i \left( \frac{E_k}{e} \right)^{a_i} \quad (4.1)$$

, where  $\Delta V_i$  is the voltage subjected to the dynode and drives the electron to strike with energy  $E_k$ ,  $a$  is the slope of the curve in Fig. 4.3 which depends on the material nature,  $i$  is the dynode stage index. So the overall amplification  $G$  can be written in

$$G = \prod_{all\ i} g_i = \prod_i K V^A \quad (4.2)$$

, where  $V$  is the high voltage (HV) applied to MAPMT,  $K$  and  $A$  are the serial products (with some rearrangements) of  $k_i$  and  $a_i$ . The gain-to-HV power-law relation is shown in Fig. 4.4. For a typical MAPMT subjected to HV  $\sim 1000$  V divided by 10 dynode stages, the gain of each dynode is about 5 (100V), and the overall gain is  $5^{10} \sim 10^{5-6}$ . The proportional constant  $K$  depends highly on the fabrication quality and the design of the photocathode, it may vary by factor 3–5 among pixels of one MAPMT.



#### 4.1 Review of conventional MAPMTs

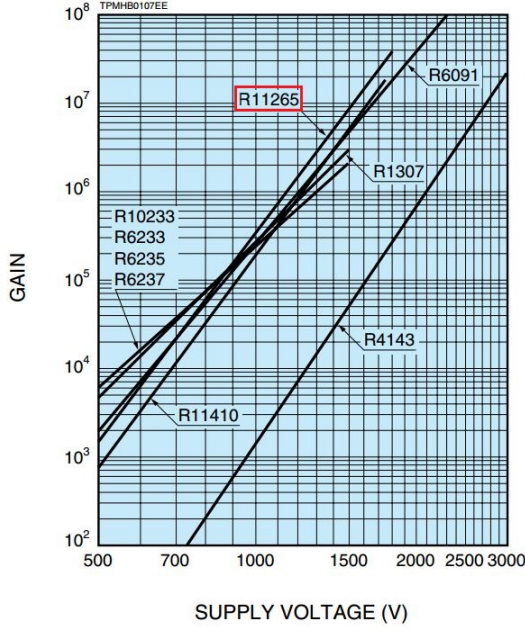


Figure 4.4: The gain to HV relation of MAPMTs. *UBAT* MAPMT R11265 is marked in red.

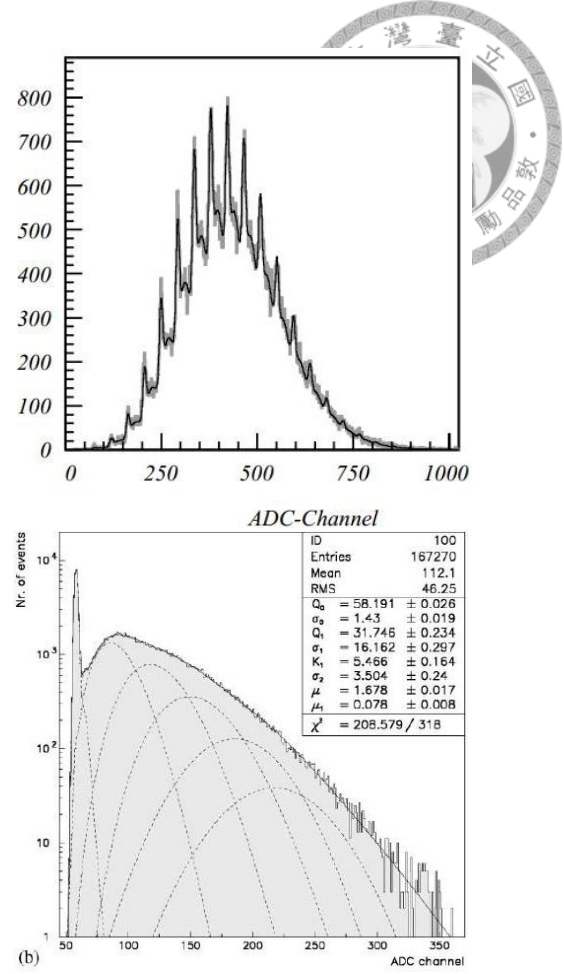


Figure 4.5: The examples of HPD (top) and PMT (bottom) signal histograms.

It is important that, although QE and  $G$  may be regarded as constants as the HV is fixed, electrons are only created/annihilated by integer many. It implies the number of electrons after each stage obeys Poisson distribution, e.q. the number of PEs generated by a constant light pulse obeys Poisson distribution; the overall amplification of the Dynode process is a serial product of Poisson distributions, which may be simplified with a single Gaussian distribution considering the gain is typically as large as  $10^5-6$  [2]. In realistic signal modeling, if the uncertainty of the Gaussian-like (dynode) process is small, the detector observes well separated peaks corresponding to different numbers of PEs emitted at the photocathode. This is usually the case of Hybrid Photon Detector (HPD) or Avalanche Photon Detector (APD) (Fig. 4.5, top panels) [3]. On the contrary, for PMTs/MAPMTs which utilize 10 dynode stages or more, the large uncertainty of the Dynode process leads

to a convoluted smooth signal histogram or sometimes partially separated. In weak light situations ( $PE < 5$ ), one may model the signal with many Gaussian distributions whose heights are governed by a Poisson distribution (Fig. 4.5, bottom panels). When the incident light is strong enough to stimulate more than 5 PEs, a single smooth Poisson function is sufficient to fit the signal histogram [4, 5].

## 4.2 DARK CURRENT

The dark current of *UBAT* MAPMT was calibrated at 770 V. 100 k events were taken under the self trigger scheme after 1 hr. baking (Fig. 4.6).

Most of the channels exhibited 0–2 Hz signal rates, and a few perimetric channels near the HV power cables, namely ch. 4, ch. 7 and ch. 61, showed  $\sim 10^2$  Hz signal rates. Assuming the signal peak at 30 mV was due to the agitated electrons and was single-PE dominant, the dynode gain of MAPMT could be roughly calculated by

$$G \sim \frac{30 \text{ mV} \times 1.1 \text{ pF}}{1.6 \times 10^{-19} \text{ C/e}^-} \sim 2 \times 10^5 \quad (4.3)$$

It was a reasonable result and I expected the calibrated gain to be comparable to 30 mV.

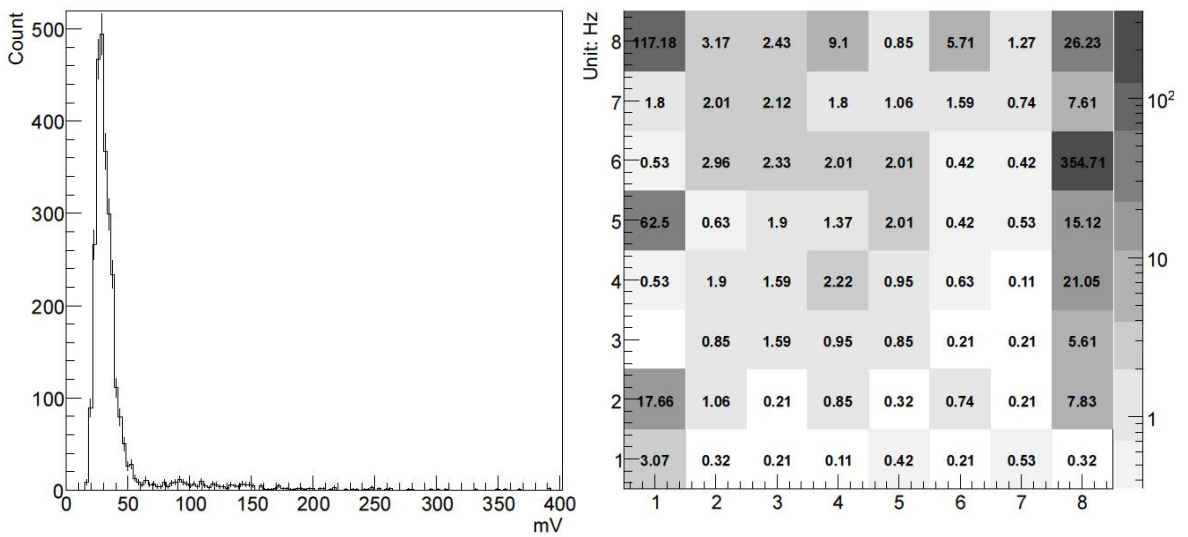
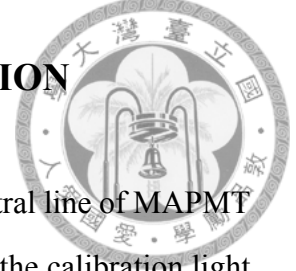


Figure 4.6: The typical dark current of *UBAT* MAPMT. The left-handed panel presents the signal histogram, the right-handed panel presents the map of the trigger rates in 64 channels.

### 4.3 PHOTON COUNTING AND GAIN CALIBRATION



A blue LED with similar spectrum of YSO was placed on the central line of MAPMT as the calibration source. At a distance 1.6 m, the divergent angle of the calibration light was  $\sim \pm 0.4^\circ$ . The LED was controlled by an oscilloscope and shined 10–20 nsec. pulse lights at 1 kHz. For each light level, i.e. pulse width, 50k events were recorded under force trigger scheme. The external triggers were synchronized with the light pulses, so the background triggers were completely suppressed and the true signal triggers were hardly biased by threshold.

The number of LED photons arrived at the MAPMT was assumed constant  $N$  since it shined at very short pulses. Detection efficiency was also assumed to be a constant  $\epsilon \cong \text{QE} \times 1^{\text{st}} \text{ dynode sensitivity}$ . The probability of detecting  $n$  PEs obeyed the Poisson distribution [3, 6]

$$\mathcal{P}_{\text{cathode}}(n) = \frac{\mu^n}{n!} e^{-\mu} \quad (4.4)$$

, where  $\mu$  is the mean #PE being detected, which could be simply taken as  $\mu = N\epsilon$ . The equation was generally applicable to photon detectors. When it came to MAPMT, regarding the  $10^6$  gain, the signal histogram could also be described by a smooth Poisson function. The signal fitter used in this study was modified from Eqn. 4.4

$$y(x) = A \times \frac{\mu^{x/G}}{\Gamma(x/G - 1)} e^{-\mu} \quad (4.5)$$

The #PE being detected  $n$  was represented by  $x/G$ , so  $x$  was in the DAQ unit (mV). The factorial was replaced by the Gamma function since the “mean” #PE might not be a integer for the factorial to be valid. The constant  $A$  was the entry height.

With Eqn. 4.5, I determined the gains ( $G$ ) and mean #PEs ( $\mu$ ) in 64 channels at different light levels. The result is shown in Fig. 4.7. The fitted gains in every channel varied by less than 3% at different light levels. The gains were about 30 mV/PE in the central channels, 20 mV/PE in other channels, and about 10 mV/PE in some perimetric channels. In every channel, the calibrated gain differed by less than 3% from the dark current peak observed

in 4.2. The result justified the dark current peaks were really single-PE.

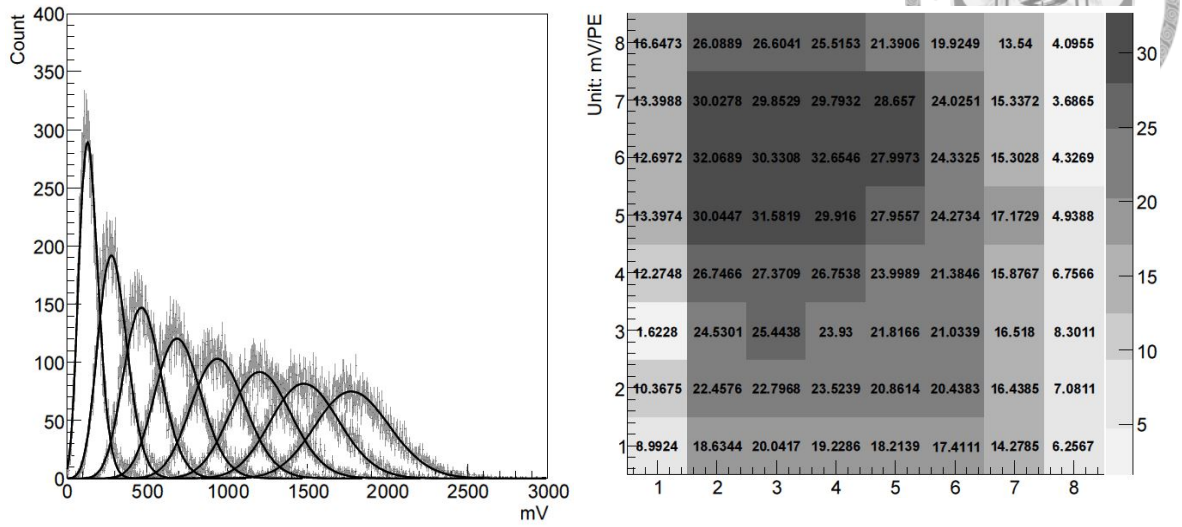


Figure 4.7: left: The signal histograms of 8 different light levels, ranged from 5 to 60 PEs. The signal error bars and the fitting functions are represented by the faded and thick black lines, respectively. right: The gain distribution of 64 channels. The gains in the central region were about 4 times higher than those around the perimeter.

### *4.3 Photon counting and gain calibration*

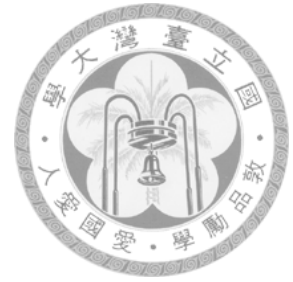




## Bibliography

- [1] Hamamatsu Photonic K. K. editorial committee 2006, *PHOTOMULTIPLIER–Basics and Application*, 3<sup>rd</sup> ed.
- [2] Foord, R., et al. 1969, *Appl. Opt.*, 8-10, 1975
- [3] Hoepfner, K., et al. 2002, *Nucl. Inst. and Meth. A*, 483, 747
- [4] Chirikov-Zorin, I. E., et al. 2001, *Nucl. Inst. and Meth. A*, 461, 587
- [5] Dossi, R., et al. 2000, *Nucl. Inst. and Meth. A*, 451, 623
- [6] Fried, D. L., et al. 2006, *Opt. Mate.*, 35, 1679

## *BIBLIOGRAPHY*





## CHAPTER 5

# CALIBRATION OF UBAT FS

Since the gains had been calibrated for all the channels, signals were presented in the unit of #PE in later experiments for better comparison. The calibrations involved the complete construction of *UBAT* FS detection unit were proceeded under the collimated trigger scheme, with the central channel ch. 27 chosen to be the collimated main channel.

The experimental background and the cosmic ray veto are discussed in 5.1. In 5.2, the calibration of PE yield of the detection unit is reported. With the aid of the collimated trigger scheme, I was able to calibrate the crosstalk and estimate the shares of the total scintillation budget. The quantification of the crosstalk is elaborated in 5.3.

### 5.1 EXPERIMENTAL BACKGROUND

50k events were recorded by the full construction of the detection unit under the collimated trigger scheme. DAQ saturations occurred at 0.49 Hz. According to the estimation in 3.4 and substituted the gains acquired in 4.3, a  $\sim$ MeV cosmic ray event was expected to yield the signal more than  $10^5$  mV (3000 PEs), which is far beyond the range of DAQ. So I identified the saturation events as the cosmic ray and vetoed them.

Fig. 5.1 was the cosmic-ray-vetoed self scintillation spectrum of YSO crystal. The major peak was at the rate 31.56 Hz. The spectrum was generally in consistent in shape to the YSO:0.3%Ce spectrum provided in [1]. Assuming the 1.3 PEs peak was the Yttrium/Silicon peak at 2 keV, the PE yield was  $\sim$ 0.7 PE/keV. The result suggested *UBAT* might be able to self-calibrate the energy scale on-board with the Yttrium radioactivity.



## 5.2 Energy calibration

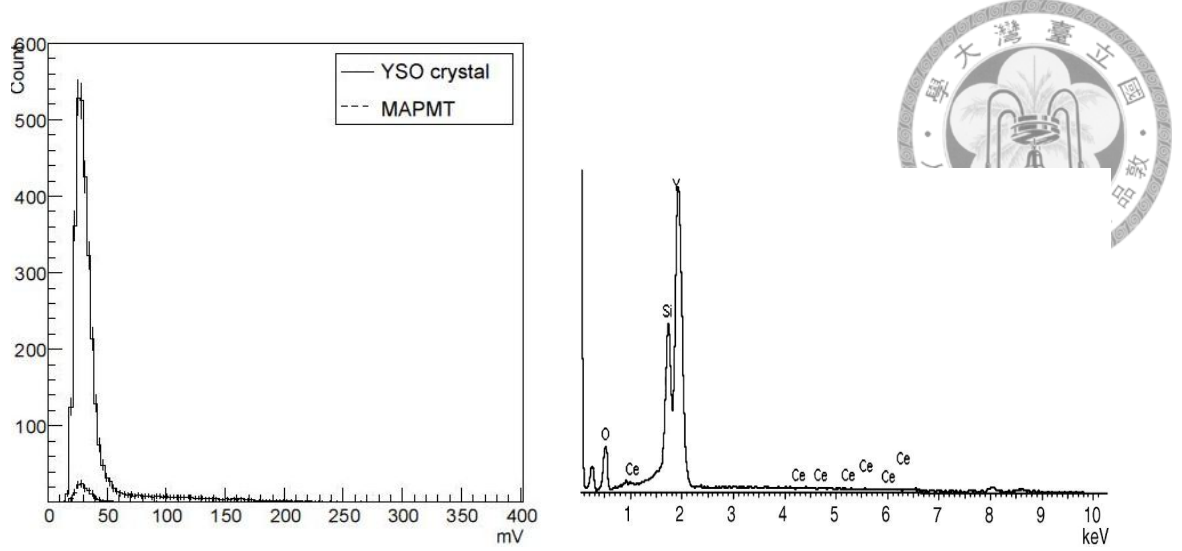


Figure 5.1: The observed YSO crystal self scintillation (left-handed) and a reference spectrum copied from [1] (right-handed). The two spectra are in agreement in 1.5–6 keV, including the Y/Si and Ce radioactivities. But due to the low energies, it's unlikely *UBAT* FS detection unit can resolve the spectrum as clear as the reference with few PEs. The rate-normalized MAPMT background, i.e. dark current, is also shown in the figure.

## 5.2 ENERGY CALIBRATION

Tab. 5.1 lists the radioactive calibration sources used in this study. The range was 8–60 keV. The sources were from a separated  $\text{Am}^{241}$  coin whose activity was  $\lesssim 300$  mCurie<sup>1</sup> and *Amersham Variable X-ray Source* that contained 6 non-radioactive targets stimulated by build-in  $\text{Am}^{241}$  [2]. The X-ray photon flux was estimated by, assuming isotropic decay,

$$\mathcal{F} \sim A \times (3.7 \times 10^7) \times \frac{\pi 0.5^2}{4\pi R^2} \quad (5.1)$$

Because the round collimator pinhole was 0.5 mm in radius and the distance ( $R$ ) between the sources and the scintillator was far greater, the flux was estimated by the area ratio, and  $A$  was the radioactivities in mCurie. I intended to control the fluxes at 150–200 Hz, which corresponded to  $R \sim 100$ –120 cm at 300 mCurie. It turned out the distances gave the fluxes were 80–100 cm. It might due to the degradation of the sources or the inefficiencies of the detections.

The calibration sources were applied successively to the detection unit. In each run, 50k events were taken under collimated trigger scheme. The signal strengths were identi-

<sup>1</sup>1 Curie=  $3.7 \times 10^{10}$  decay/sec.



keV	$K_{\alpha}$	$K_{\beta}$
$\text{Am}^{241}$	59.5	59.5
Tb	44.23	50.65
Ba	32.06	36.55
Ag	22.10	24.99
Mo	17.44	19.63
Rb	13.37	14.97
Cu	8.04	8.91

Table 5.1: The radioactive calibration sources utilized in this study.

fied as the fitting means of the Gaussian fits to the histogram peaks, and the fits were in the ranges from the shallowest points between the peaks and the pedestals to the symmetric points above the peaks. Fig. 5.2 shows the result of the calibration. Only four sources,  $\text{Am}^{241}$  (60 keV), Tb (44 keV), Ba (32 keV) and Ag (22 keV) were identified from the signal histograms. For other sources below 20 keV, the signals only reflected the fluxes  $\sim 150$  Hz, but only the source-induced pedestals were observed. The cause of the pedestal was unclear. But by adjusting the locations of the sources, both the peaks and the pedestals followed the changes of fluxes. So it was concluded the pedestals were induced by the X-ray but instruments. Also shown in Fig. 5.2 is the PE yield. The PE yield was 0.72 PE/keV and linear.

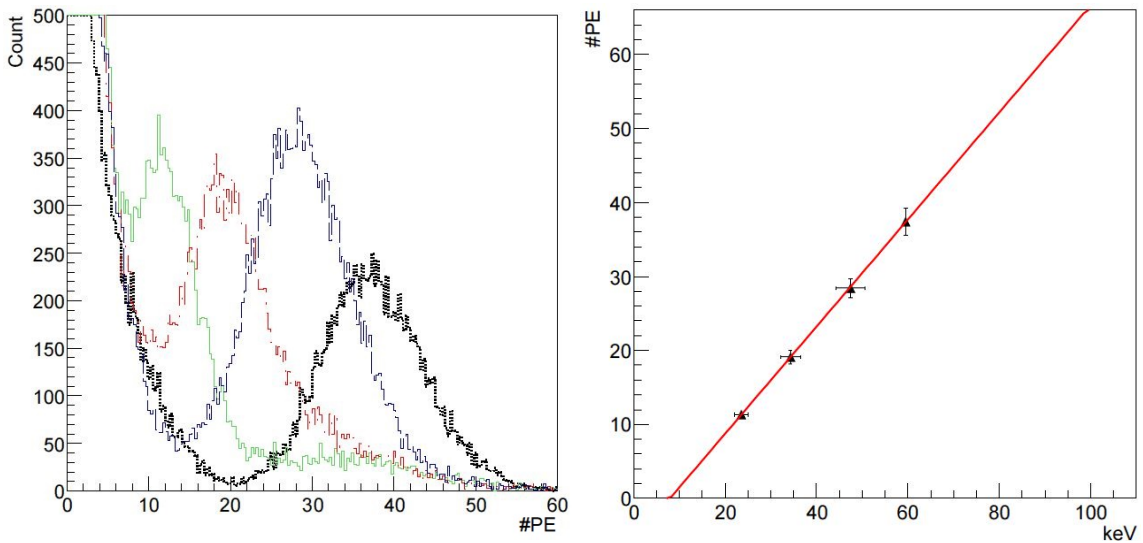


Figure 5.2: left: The signal histograms of, peaks from right to left,  $\text{Am}^{241}$ , Tb, Ba and Ag. right: The peak #PEs versus the corresponding X-ray energies. The linear fit shows the slope 0.72 PE/keV. The error bars were taken as  $K_{\alpha}-K_{\beta}$ .

### 5.3 Crosstalk calibration

Some conclusions were made from the result:

1. The PE yield given by the estimation in 3.4 was about thrice of the calibration result.
2. Considering the source-induced pedestal, it may be difficult for *UBAT* to determine the X-ray energy below 18 keV from the signal spectra.
3. Although the energy may be indeterminable below 18 keV, the detection unit still reflected significant trigger responses down to 8 keV. It was sufficient for the coded mask aperture camera of *UBAT* to identify the mask pattern.
4. The calibration sources showed a linear PE-keV relation but deviated by 7.9 keV. While it might imply a detection threshold of 7.9 keV, the linear-fit PE yield was in consistent to which of the estimation from the Yttrium 1 keV self scintillation.



### 5.3 CROSSTALK CALIBRATION

I'd focused on the collimated channel in 5.2 because it will provide the GRB spectrum of *UBAT*. To visualize the pattern of the coded mask clearly and determine the GRB directions with accuracy, which is an even more important role of *UBAT*, however, relies on the sharpnesses of the entire FS images, i.e. the discriminability of the X-ray-illuminated and non-X-ray-illuminated channels. Fig. 5.4 explains the situation of the crosstalk. It presents the  $\text{Am}^{241}$  signals observed by the collimated channel, the alongside channels and the diagonal channels (Fig. 5.3).

Figure 5.3: An illustration of the channel naming. The black channel is the collimated (trigger) channel, the red channels are the alongside channels, and the green channels are the diagonal channels.

7	8	23	24	39	40	55	56
6	9	22	25	38	41	54	57
5	10	21	26	37	42	53	58
4	11	20	27	36	43	52	59
3	12	19	28	35	44	51	60
2	13	18	29	34	45	50	61
1	14	17	30	33	46	49	62
0	15	16	31	32	47	48	63

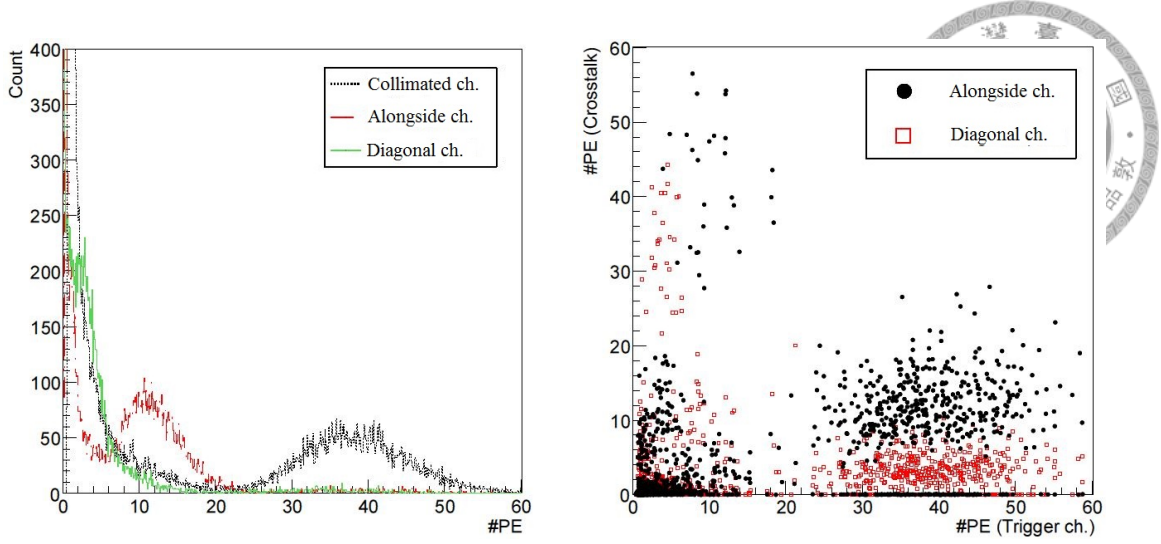


Figure 5.4: left: The spectra of  $\text{Am}^{241}$  observed in the collimated, alongside and the diagonal channels. It is understood from the spectra a significant fraction of the scintillation photons were observed by the non-collimated channels. right: The correlation plot of the  $\text{Am}^{241}$  signal of each event observed in the alongside/diagonal channels to the collimated channel. In the crosstalk-free case, all the data points should lay on the horizontal axis.

$38.27 \pm 3.25$ ,  $11.22 \pm 0.99$  and  $3.13 \pm 0.26$  PEs were observed in the collimated channel, the alongside channels<sub>(avg.)</sub> and the diagonal channels<sub>(avg.)</sub>, respectively. It's obviously a great fraction of the scintillation light didn't illuminate the collimated MAPMT pixel. The crosstalk was quantified by the Crosstalk Ratio ( $CR$ ) defined by

$$CR = \frac{\#PE \text{ observed in the ch. of discussion}}{\#PE \text{ observed in the collimated ch.}} \times 100\% \quad (5.2)$$

, e.q.  $CR_{\text{alongside}} = 11.22/38.27 \sim 30\%$ . The  $CR$ s in the alongside channel and the diagonal channel were 29% and 8%, respectively. If the crosstalk in remoter channels was omitted, one could conclude the leakage of the emitted scintillation light was about 60%, e.q.

$$\frac{\text{crosstalk}}{\text{crosstalk} + \text{collimated}} = \frac{(8\% + 29\%) \times 4}{(8\% + 29\%) \times 4 + 100\%} = 0.60 \quad (5.3)$$

, where the factor 4 was for the 4 alongside/diagonal channels. The result coincided with the PE yield difference between the expectation and the calibration.<sup>2</sup> It indicated the crosstalk led to not just a serious drawback of detection efficiency, but even crucial, a

<sup>2</sup>See 5.2, last paragraph.

### 5.3 Crosstalk calibration

smearing of the coded mask image. Fig. 5.5 shows a simulated coded mask image considering the crosstalk. One could immediately understand by comparing the expected coded mask image and the resulting one, it's unlikely *UBAT* could set up a simple threshold and discriminate the X-ray-illuminated and -non-illuminated channels of a factor-10 dynamic range, e.g. 15–150 keV, under the rate trigger scheme.

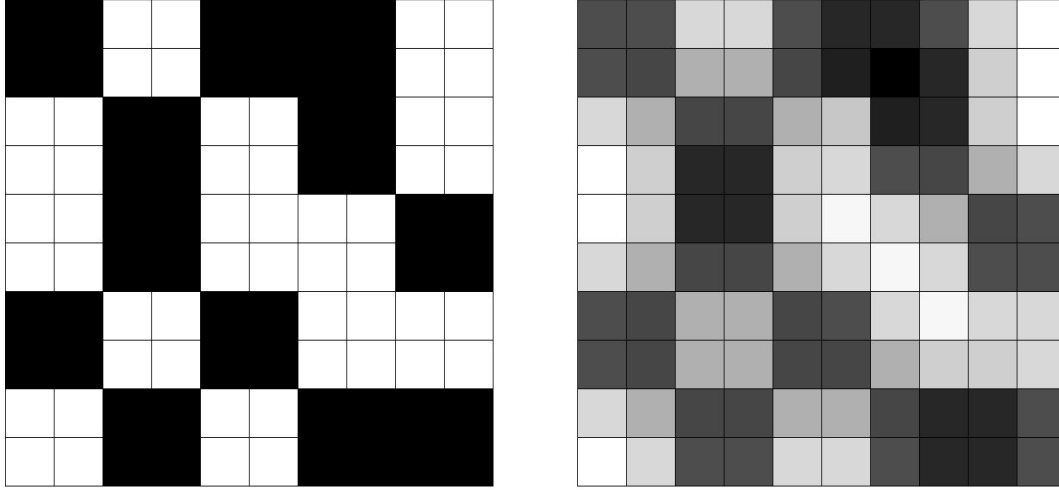


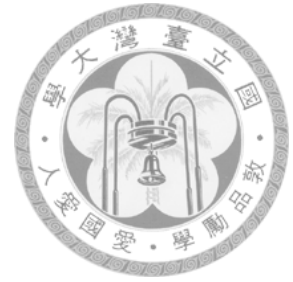
Figure 5.5: The comparison of the scintillation detections of the expected coded mask image (left-handed) and the simulated observation (right-handed) with CRs 0.29 and 0.08 into the alongside and the diagonal channels. The simulation presents the result in  $10 \times 10$  FS channels ( $5 \times 5$  coded mask pixels), both figures are normalized by the channels of the highest energy and equally scaled in the gray-scale.



## Bibliography

- [1] Zycha, E., et al. 2008, *Jour. of All. and Comp.*, 451, 1-2, 286
- [2] M.I.T. Dept. of Phys. 2007, in *X-Ray Physics*, from *Amersham* Data Sheet 11196

## *BIBLIOGRAPHY*





## CHAPTER 6

# SIMULATION

To further resolve the crosstalk issue and search for possible solutions, I've constructed the simulation package of the *UBAT* FS with GEANT4. The simulation includes the X-ray sources, the collimator, the scintillator array, the optical couplant and the MAPMT. Both the scintillator and the MAPMT were hybrid components composed of many different materials. I inspected their constructions thoroughly so I could pin point the cause the crosstalk. The simulation doesn't include the DAQ operation but registers the exact coordinates of the primary PEs for off-line analysis.

Fig. 6.1 is the construction of the apparatus. There are the lead collimator, the YSO crystal array coated by VM2000 reflector, 100  $\mu\text{m}$  Dow-Corning optical grease, and the MAPMT. The constructions of the scintillator array and MAPMT are discussed in 6.1 and 6.2, respectively; other miscellaneous details on the apparatus such as the signal registration, the optical couplant...etc. are collected in 6.3. 6.4 lists the physical processes implemented in the simulation. Finally, the simulated experimental result were presented in the identical format of the calibration data in 6.5.



## 6.1 Construction of YSO scintillator array

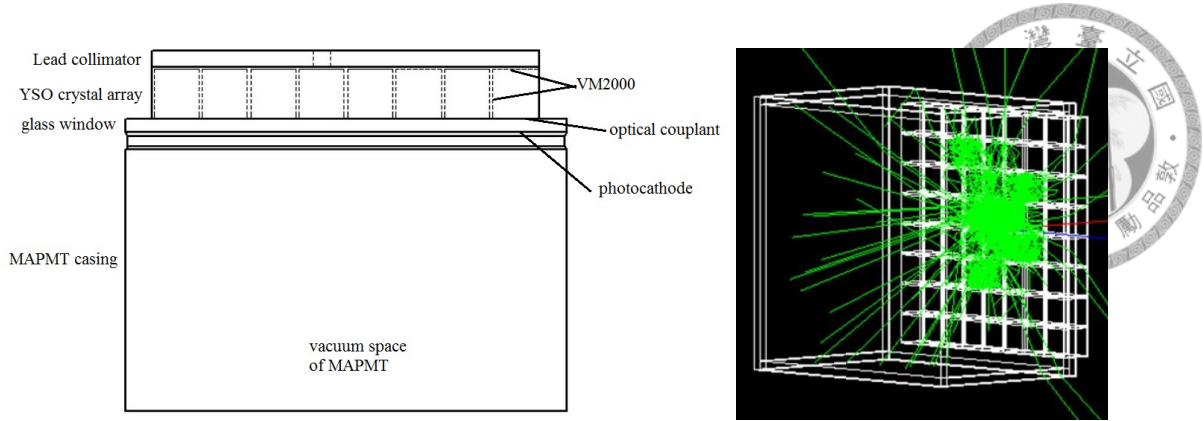


Figure 6.1: The side view (left-handed) and the 3D screen shot (right-handed) of the simulation. The green lines scattered in the 3D screen shot represent the paths of the scintillation photons generated by one 60 keV X-ray photon. It can be seen a non-trivial amount of the scintillation photons may travel into non-collimated channels.

## 6.1 CONSTRUCTION OF YSO SCINTILLATOR ARRAY

### YSO crystal

The schematics of the crystal cubes is in Fig. 2.11.  $2.68 \times 2.68 \times 3(\text{thickness}) \text{ mm}^3$  YSO:0.2%Ce crystal cubes were arranged as an  $8 \times 8$  matrix. All the elements needed by the YSO compound were acquired from GEANT4's material bank. The scintillation spectrum implemented is shown in Fig. 6.2. In spite of many papers had reported the YSO posing it's peak emission at 420 nm, the spectrum utilized here was provided by the crystal manufacturer whose peak was at  $\sim 400 \text{ nm}$  [1, 2]. An wavelength-independent absorption length 50 cm was used in the range of Fig. 6.2. The absorption length corresponded to  $-2\% \text{ flux/cm}$ . The refractive index of YSO was 1.80.

### 3M VM2000 reflector

At the beginning the reflectance of VM2000 was assumed perfect, i.e.  $> 0.999$ , but it was later realized from the performance of the simulation, e.q. unrealistic CR, interminable runtime..., the amount of the crosstalk could be sensitive to the reflectance.

Since VM2000 was widely applied by many experiments, the calibration data could be obtained easily. The reflectance was mostly reported as a wavelength-independent constant in 0.89–0.99, e.q. [3], which was unacceptably inaccurate considering the purpose

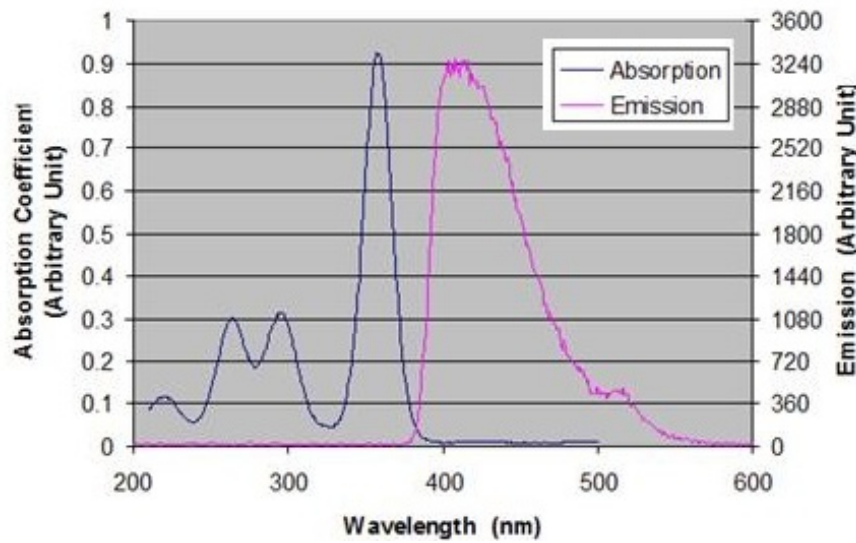


Figure 6.2: The YSO scintillation spectrum provided by the manufacturer. The peak wavelength of scintillation was 400 nm.

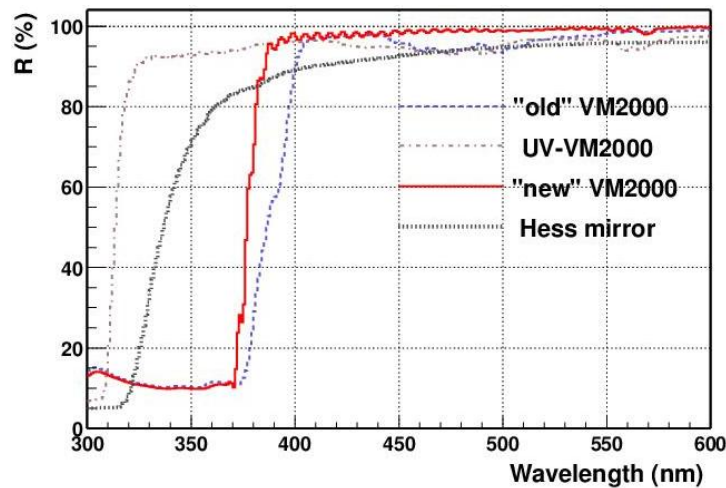


Figure 6.3: The reflectance of VM2000 copied from [4]. The “new” one was implemented by the simulation.

of simulating the crosstalk. These reflectance was calibrated by referring to an “almost perfect” standard  $\text{AlO}_2$  diffusive reflector built in the spectrometer. [4] had demonstrated the simulation of a scintillation detector is sensitive to the reflectance of the crystal coating. The reason of the standard-reference-based calibration being inaccurate were

1. The coatings usually had the comparable or slightly higher reflectances than the standard “perfect”  $\text{AlO}_2$ . The little differences between the reflectances to be calibrated and the reference led to significant uncertainties.
2. If the coatings were the specular type, the calibration results could be highly setup

## 6.1 Construction of YSO scintillator array

(light path) dependent. This was also the case of VM2000.

VM2000 was calibrated in [4] by a self-referred method. The result was implemented in the simulation (Fig. 6.3).

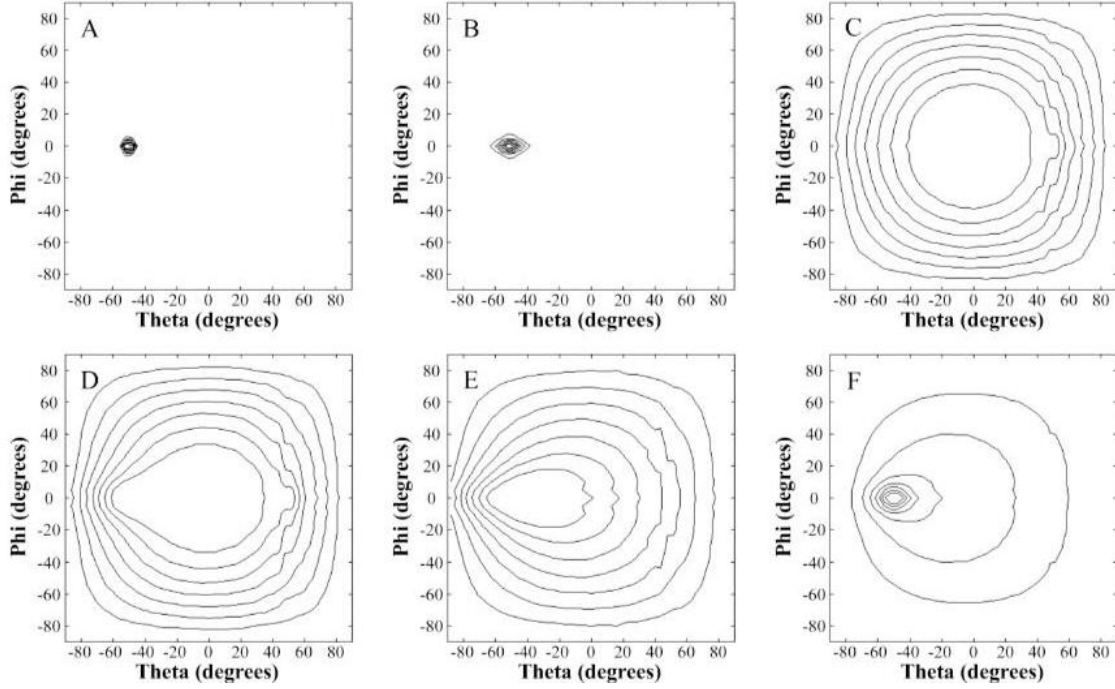


Figure 6.4: Reflected laser profiles of the reflectors. All shown by the angular distributions focus at  $50^\circ$ . The samples are A: VM2000, B: Aluminum foil, C:  $\text{TiO}_2$  paint, D: 3 layers of Teflon<sup>®</sup> tape, E: Tvvek<sup>®</sup> paper, F: Lumirror<sup>®</sup>.

[5] provided a detail study on the peculiarities of some widely used reflectors. Fig. 6.4 lists the reflected laser beam profiles of the reflectors. It can be seen VM2000 was the most specular one among all, and the beam refracted  $\sim 15^\circ$ . The specularity was modeled by the *GLISUR* model built in GEANT4 Optical Photon Process. The surface roughness was described by  $\alpha \equiv \cos(\theta)$ , where  $\theta$  was the open angle of the specular spike of the point source (see Fig. 6.5) [6]. In the case of VM2000,

$$\cos^{-1}(\alpha) \sim 15^\circ \Rightarrow \alpha = 0.97 \quad (6.1)$$

The dielectric multilayer reflectors like VM2000 were constructed with layers of  $\sim 0.5$   $\mu\text{m}$  thick polymer foils of two different refractive indices, usually  $n_1 \sim 1.9/n_2 \sim 1.7$  or

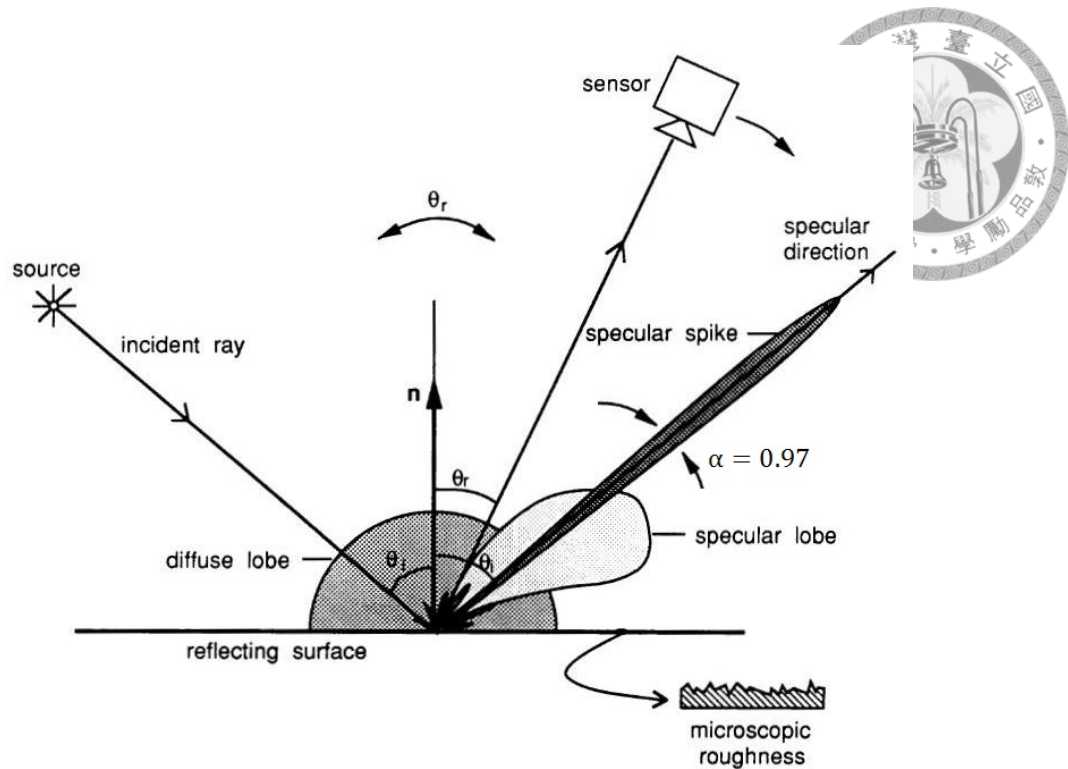


Figure 6.5: A complete modeling of the reflective surface including the diffuse lobe, the specular spike and the specular lobe. When a point-like parallel light illuminates the surface, the reflection appears to have the focused component and the smeared component. The focused component is called the specular spike. The isotropic and anisotropic smeared components are called the diffuse lobe and the specular lobe, respectively.

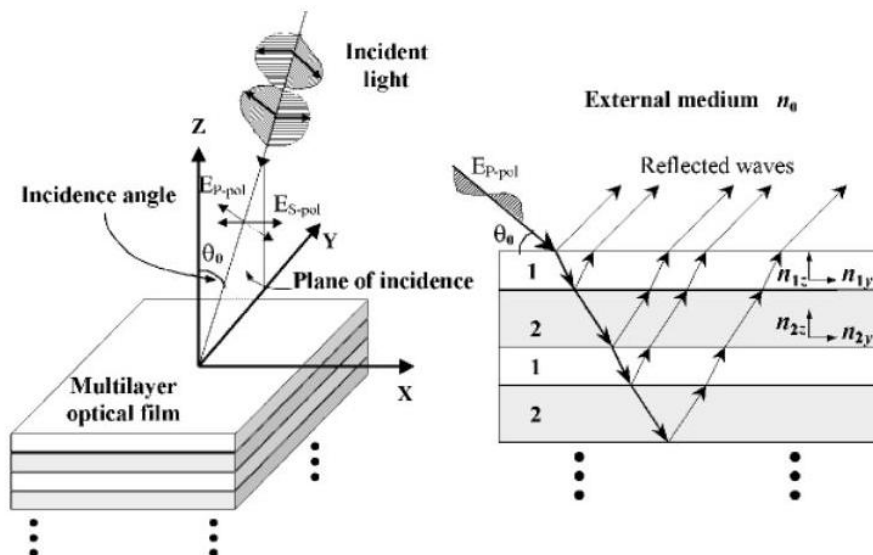


Figure 6.6: The construction of the multilayer reflector. When the light travels from the large-refractive-index foil to the one with smaller refractive index, total reflection occurs. The reflector is made of the two polymer foils sandwiching each other. Note that only p-polarized light is reflected.

## 6.2 Construction of UBAT MAPMT

$n_1 \sim 1.5/n_2 \sim 1.3$  (Fig. 6.6) [7]. Whenever the photon traveled from  $n_1$  to  $n_2$  at angles  $\gtrsim 60^\circ$ , total reflection occurred. The probability of a photon traveling  $1 \mu\text{m}$  into the reflector (one layer of both materials) was about 7%<sup>1</sup>. It corresponded to the absorption length

$$e^{-100/L_{abs}} = 0.07 \Rightarrow L_{abs} \sim 15\mu\text{m} \quad (6.2)$$

One could actually see the light through the  $10 \mu\text{m}$  VM2000 foil bare-eyed. The simulation indeed showed the scintillation photons could penetrate the reflector in to the neighboring crystal cells and enhanced the crosstalk. This was the reason the original scintillator array coated with  $10 \mu\text{m}$  VM2000 was replaced by the current design.

## 6.2 CONSTRUCTION OF UBAT MAPMT

### Glass window

Hamamatsu R11265 had a 0.8 mm-thick frontal glass window made of Hamamatsu UV-transmitted type glass. It had the refractive index 1.53, constant absorption length about 10 cm ( $\sim -10\%/cm$ ) at the wavelength longer than 250 nm. While being a rather simple component, the glass window was one of the key component led to the crosstalk. Because the MAPMT inner space behind the glass window was vacuum, total reflection occurred at the glass-vacuum interface. Although the scintillator ( $n \sim 1.8$ ) and the glass window ( $n \sim 1.5$ ) were well coupled by the optical couplant, the photons frequently encountered difficulties penetrating the glass-vacuum window to be the signals. On the contrary, when they were reflected, they were likely to be detected by the nearby channels as the crosstalk. Fig. 6.7 presents a snapshot of the simulation. The total reflections occurred at the glass-vacuum boundary can be seen.

### Photocathode

The photocathode was a  $\sim 20 \text{ nm}$  thick film of Bealkali metal evaporated on to the inner (vacuum) side of the glass window. It looked transparent from some angles and

---

<sup>1</sup>It's not  $60^\circ/90^\circ = 1/3$  because the illumination was not isotropic.

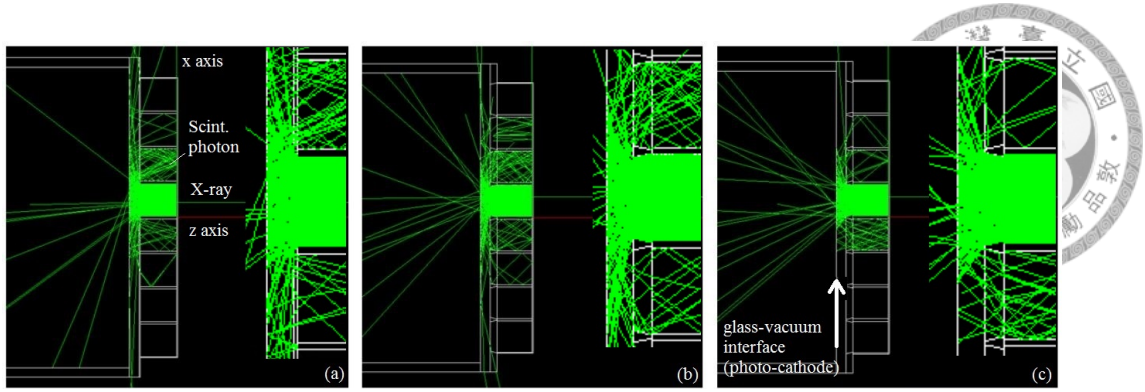


Figure 6.7: The side-view snapshots of the simulations. Three cases are presented: a) no light guide (LG), the original design of the detection unit, b) with a traditional focusing LG, c) with a Inverted-Conical LG. The green lines represent the photon paths. It can be seen in the figures the total reflections occurred frequently at the glass-vacuum boundary, and most of the reflections became the crosstalk. The paths at the left-hand side of the boundary represent the photons weren't absorbed by (and penetrated) the photocathode. By comparing the three cases, it's obvious the Inverted-Conical light guide suppressed the crosstalk.

metallic otherwise. In classical electrodynamics, the reflectance ( $R$ ) and the absorbance ( $A$ ) of a thick metal depended on the complex refractive indices of the mediums and both were the dependences of the incident angle. It's known the electromagnetic (EM) wave could only travel a few “skin depths” into the metal before being fully absorbed. In other word,  $R$  and  $A$  exhausted the 100% probability of the fate of the photon. On the other hand, when the metal had the thickness comparable to the wavelength, it's possible the EM wave could travel through the film-like metal. In this case, one must consider  $R$  the transmittance ( $T$ ) to determine the accurate  $A$  [8].

The *dielectric\_metal* optical boundary model prepared in GEANT4<sup>2</sup> required the users to verify  $R$  and  $A$  of the metallic object as two constants explicitly. As which elaborated in the previous section, the model was obviously insufficient to the end of simulating the angular dependency of the photocathode, for the simulated crosstalk and the signal strength were naturally sensitive to  $R$  and  $A$ , respectively. I constructed a new model of the optical boundary in the source library of GEANT4 Optical Photon Process to describe the  $R$ ,  $T$  and  $A$  of the film-like metals. The model was named *dielectric\_filmMetal*. It required the user to verify the real refractive indices of the dielectric mediums sandwiched the metallic film, the complex refractive index of the film metal, and the thickness of the

<sup>2</sup>ver. 4.9.5, the recommended production version until May, 2013.

## 6.2 Construction of UBAT MAPMT

metallic film. All the refractive indices could be set as lookup tables depended on the wavelengths.

The analytical prescription of the metallic film to the photocathode had been demonstrated in some works [9, 10]. Considering the usage of MAPMT, the parameters required were the thickness of the photocathode, the refractive indices of the glass window ( $\mathbb{R}$ ), the photocathode ( $\mathbb{C}$ ) and the vacuum ( $\mathbb{R}$ ). The classical EM equations utilized by the *dielectric\_filmMetal* model were

$$a_R(\lambda, \theta) = \frac{r_{23} + r_{34}e^{2i\delta}}{1 + r_{23}r_{34}e^{2i\delta}} \quad (6.3)$$

$$a_T(\lambda, \theta) = \frac{t_{23}t_{34}e^{2i\delta}}{1 + r_{23}r_{34}e^{2i\delta}} \quad (6.4)$$

where

$$n_i \sin(\theta_i) = n_j \sin(\theta_j) \quad (\text{Snell's Law}) \quad (6.5)$$

$$r_{ij} = \frac{n_i \cos(\theta_{i(j)}) - n_j \cos(\theta_{j(i)})}{n_i \cos(\theta_{i(j)}) + n_j \cos(\theta_{j(i)})} \quad (6.6)$$

$$t_{ij} = \frac{2n_j \cos(\theta_i)}{n_i \cos(\theta_{i(j)}) + n_j \cos(\theta_{j(i)})} \quad (6.7)$$

$$\delta = \frac{2\pi d n_3^* \cos(\theta_3)}{\lambda} \quad (6.8)$$

, where  $d$  denoted the thickness of the photocathode,  $n$ 's denoted the refractive indices, and  $\theta$ 's denoted the propagating angles with respect to the normal direction of the interfaces, i.e. Z axis in Fig. 6.7. The medium originated the scintillation photons, the glass window, the photocathode and the vacuum space were denoted by the lower indices  $i(j) = 1, 2, 3$  and 4, respectively<sup>3</sup>.

$$n_3^* = n_{ph} + ik_{ph} \quad (\text{photocathode}) \quad (6.9)$$

Eqn. 6.6 and Eqn. 6.7 were for the p-polarized wave; for the s-polarized wave, one needed

<sup>3</sup>[9] used  $i = 1$  to denote the scintillator and neglected the coupling medium of the scintillator and the glass window. But based on the derivation provided in [8], it's better regarded  $i = 1$  as the optical couplant contacting the glass window. In this simulation,  $i = 1$  was taken to be the optical couplant, the scintillation photons were originated in the YSO crystal region and the angles in the optical couplant region were calculated by the Snell's Law.

to use indices noted in the parentheses. The reflectance could be calculated by

$$R_{s,p}(\lambda, \theta) = |a_R^{s,p}|^2 \quad (6.10)$$



Considering the Fresnel reflection coefficient between the scintillator and the glass window,

$$F_s(\lambda, \theta) = \left[ \frac{\sin(\theta_1 - \theta_2)}{\sin(\theta_1 + \theta_2)} \right]^2 \quad (6.11)$$

$$F_p(\lambda, \theta) = \left[ \frac{\tan(\theta_1 - \theta_2)}{\tan(\theta_1 + \theta_2)} \right]^2 \quad (6.12)$$

, the overall reflectance was then

$$R_{s,p}^{tot}(\lambda, \theta) = F_{s,p} + \frac{R_{s,p}(1 - F_{s,p})^2}{1 - F_{s,p}R_{s,p}} \quad (6.13)$$

Assuming even polarization generated by the scintillator crystal,

$$R^{tot}(\lambda, \theta) = \frac{1}{2}[R_s^{tot}(\lambda, \theta) + R_p^{tot}(\lambda, \theta)] \quad (6.14)$$

Also considering the Fresnel reflection between medium 1 and 2, the nonzero photocathode transmittance was calculated by

$$T_{s,p}(\lambda, \theta) = \frac{n_4 \cos(\theta_4)}{n_2 \cos(\theta_2)} |a_T^{s,p}|^2 \quad (6.15)$$

$$T_{s,p}^{tot}(\lambda, \theta) = \frac{T_{s,p}(1 - F_{s,p})}{1 - F_{s,p}R_{s,p}} \quad (6.16)$$

$$T^{tot}(\lambda, \theta) = \frac{1}{2}[T_s^{tot}(\lambda, \theta) + T_p^{tot}(\lambda, \theta)] \quad (6.17)$$

This equation permitted the photon penetrating the photocathode shown in Fig. 6.7. Finally, the photon absorbance of the photocathode was simply

$$A^{tot}(\lambda, \theta) = 1 - R^{tot}(\lambda, \theta) - T^{tot}(\lambda, \theta) \quad (6.18)$$



## 6.2 Construction of UBAT MAPMT

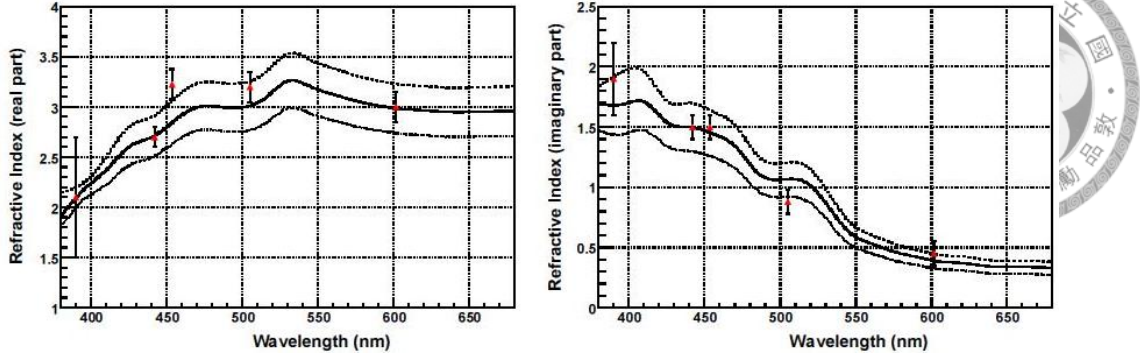


Figure 6.8: The fitted real ( $n_i$ , left panel) and imaginary ( $k_i$ , right panel) refractive indices of Hamamatsu Bialkali. The solid curves represent the best fits, and the dotted curves bound the  $2\sigma$  allow regions. The data points are plotted with  $1\sigma$  error bars.

It's justified in [9, 10] by fitting the experimental data with Eqn. 6.14 and Eqn. 6.18, the complex refractive index and the thickness of the photocathode could be determined nicely, and the angular-dependent PE signal strength was proportional to the number of photon absorbed by the photocathode. The refractive index and the evaporated thickness (20.0 nm) of Hamamatsu Bialkali material were determined in [9] (Fig. 6.8) and were implemented in the simulation of UBAT FS. Plugging other parameters required by the equations, Fig. 6.9 shows the A, R and T of the photocathode model of UBAT simulation.

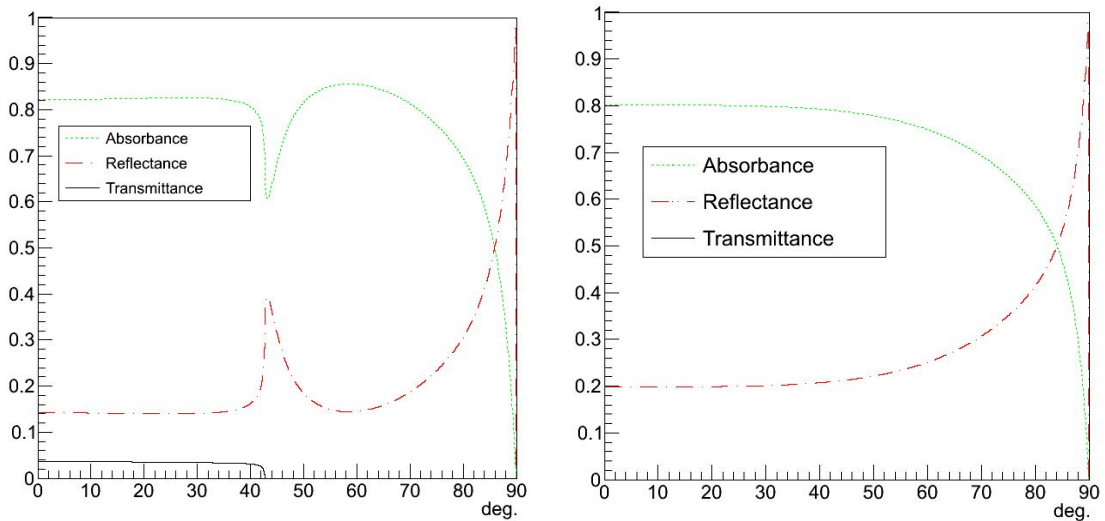


Figure 6.9: The left panel shows the angular-dependent absorbance, transmittance and reflectance of UBAT photocathode assuming  $n_1 = 1.475$ ,  $n_2 = 1.53$ ,  $n_3 = 2.28 + 1.70i$ ,  $n_4 = 1.0$ ,  $\lambda = 400$  nm and  $d = 20$  nm. Here the “typical” numbers presented as an example are of the scintillation peak of YSO. Also shown in the right panel is the result from *dielectric\_metal* model with the same parameters.

The critical angle of T was governed by the total reflection angle of the mediums sandwiching the photocathode, e.q.  $41.8^\circ$  of the glass and the vacuum in the presenting case. It was demonstrated in Fig. 6.9, if the *dielectric\_metal* model was utilized instead of the *dielectric\_filmMetal*, the signal strength (A) would be overestimated by about 100%, the crosstalk (R) would be underestimated by about 75%. Without the aid of *dielectric\_filmMetal*, the simulation was incapable to describe the crosstalk phenomenon and CR was trivially small.

### 6.3 CONSTRUCTION OF SIGNAL RECORDING AND OTHER COMPONENTS

The signal was registered by the position when the scintillation photon was absorbed at the photocathode. The MAPMT-pixel-wise signal strength was then obtained by identifying which pixel the position belonged to and accumulating all the photons generated by one X-ray photon deposition. The simulation package accumulated all the X-ray events, no trigger mechanism was presumed. In each run, 1000 successful events were recorded. e.q. not terminated by the collimator. The corresponding number of the scintillation photons was about  $1000 \times 60 \text{ keV} \times 9.2 \gamma/\text{keV} \sim 10^{5-6} \gamma\text{s}$ .

The lead collimator was identical to which applied during the experiment. The X-ray photons were generated on the center line of the collimated channel, 100 cm above the scintillator surface. They had 60 keV energy as  $\text{Am}^{241}$  and shot on the detection unit with the divergent angle  $\pm 0.05^\circ$ . The X-ray illumination covered a concentric area of the the collimating pinhole with 1.8 times radius.

The optical couplant was assumed to be a  $100 \mu\text{m}$  layer of Dow-Corning Q2-3067 of  $n=1.47-1.48$ . The  $100 \mu\text{m}$  transmittance provided by its manufacture is in Fig. 6.10, which was actually negligible at the thickness.

## 6.4 Physical process

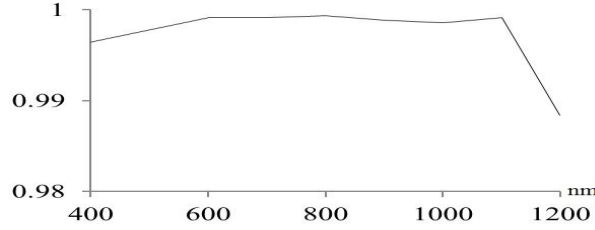


Figure 6.10: The 100  $\mu\text{m}$  transmittance converted from the data sheet of Dow-Corning Q2-3067 assuming constant attenuation.

## 6.4 PHYSICAL PROCESS

The physical processes enabled from GEANT4 Physical Process were the optical process, the low energy EM processes and the decay processes. Tab. 6.1 lists all the particles and the processes enabled. In the practical situation, the 60 keV photon only triggered the photoelectric effect or sometimes Compton scattering in the YSO crystal, then the ionization occurred so the scintillation process might take place. The boundary processes and the optical absorption were called when necessary. No other process was called at the energy level.

In very rare cases, the X-ray photons might be scattered by the crystal elements into the non-collimated nearby crystal cubes. The scintillation processes initialized in the non-collimated locations. These events were observed as the 1 (out of 1000) highlighted events in the upper-left of the 2D correlation plot of Fig. 6.11.

$\gamma$	$e^{\pm}$	$\mu^{\pm}$	$\pi^{\pm}$
<b>photoelectric effect</b>	multiple scattering	multiple scattering	multiple scattering
<b>Compton scattering</b>	<b>ionization</b>	ionization	ionization
Gamma conversion	Bremsstrahlung	Bremsstrahlung	Bremsstrahlung
	pair annihilation	pair annihilation	pair annihilation
$p^{\pm}$	$\alpha/\text{He}^{3+}/\text{Generic ions}$	charged particles	Optical photons
ionization	ionization	ionization	Cerenkov
Bremsstrahlung	multiple scattering	multiple scattering	<b>scintillation</b>
pair annihilation		Bremsstrahlung	<b>optical absorption</b>
		pair annihilation	Rayleigh scattering
			Mie scattering
			<b>optical Boundaries</b>

Table 6.1: The particles and physical processes enabled by the *UBAT* FS simulation. The bold-faced items occurred during the simulation.

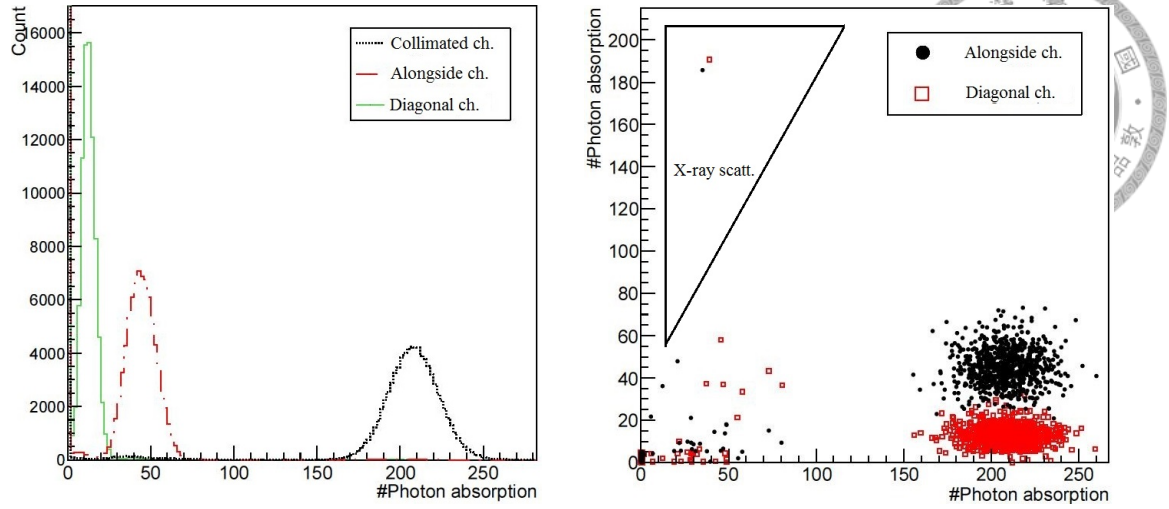


Figure 6.11: left: The simulated spectra of  $\text{Am}^{241}$  observed in the collimated, alongside and the diagonal channels. The simulation didn't show the low #PE event accumulation as in Fig. 5.3, i.e. the low #PE “shoulders” rose along the Y axis. right: The simulated correlation plot of the  $\text{Am}^{241}$  signal of each event observed in the alongside/diagonal channels to the collimated channel. Compared to the experimental data, much less events showed in the highlighted X-ray scattering region. The events located in this region implied the the X-ray photon triggered the ionization-scintillations in the non-collimated channels.

## 6.5 RESULT

Fig. 6.11 shows the result of the simulation. As stated in 6.2-Photocathode, #PE was proportional to the number of photons being absorbed by the photocathode, so CRs were derived directly from the number of absorbed photons. The simulated CRs in the alongside channel and the diagonal channel were 21.2% and 5.8%, respectively. Readers may refer to this result the the experimental data in 5.3, the simulation revealed a the CRs  $0.728 \pm 0.003$  times to the experiment in both the alongside and the diagonal channels. Comparing Fig. 6.11 to the corresponding plots in Fig. 5.4, one concluded that the simulation had much less low-luminance scattering scintillation photons and scattered X-ray events. These two disagreement might be the explanation to the underestimation of the crosstalk.

Fig. 6.12 presents the simulated event lost rate in the target energy range of *UBAT*. Because the higher-energy X-ray photons were more likely to penetrate the 3 mm depth of the scintillator before triggering any primary ionization via photoelectric effect or Compton scattering, the scintillation might not occur for the events to be detected. This result could be applied to reweigh the light curves of different energies.

## 6.5 Result

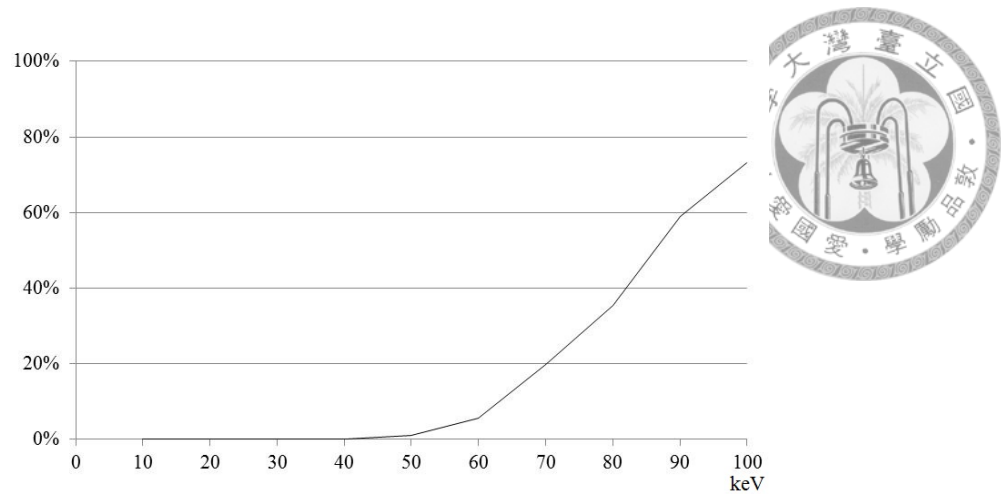


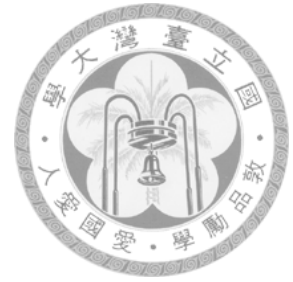
Figure 6.12: The simulated event lost rate of *UBAT* FS to different X-ray energy.



## Bibliography

- [1] Kapusta, M., et al. 2000, *Acta Phys. Polo. B*, 31-1, 101
- [2] Moszynski, M., et al. 2000, *1999 IEEE-NSS*, vol. 2, 677
- [3] Lorenz, E., et al. 2001, *Proc. of ICRC 2001*, p. 912
- [4] Motta, D. G. 2004, *Ph. D thesis*, Ruperto-Carola Univ.
- [5] Janecek, M., et al. 2008, *textitNucl. Sci., IEEE Trans.*, 55-4, 2432
- [6] Nayar, S. K., et al. 1989, *Surface Reflection: Physical and Geometrical Perspectives*, C.M.U.
- [7] Weber, M. F. 2000, *Science*, 287, 2451
- [8] Born, M., et al. 1964, *Principle of Optics*, Pergamon Press, Oxford
- [9] Motta, D. T., et al. 2005, *Nucl. Inst. and Meth. A*, 539, 217
- [10] Moorhead, M. E., et al. 1996, *Nucl. Inst. and Meth. A*, 378, 162

## *BIBLIOGRAPHY*





## CHAPTER 7

# INVERTED-CONICAL LIGHT GUIDE

### 7.1 MOTIVATION

As reported in 5.3, a serious crosstalk issue in *UBAT* FS detection unit was identified. The CR in the alongside channels were 29%. Under the rate trigger scheme with a constant energy threshold, if the 15 keV lower bound of observation is to be retained, the FS can only obtain resolvable coded mask pattern up to  $15/0.29 = 52$  keV. If the incident X-ray photon deposits more than 52 keV in the struck channel, the alongside channels may observe the crosstalk signals equivalent to the directly-struck X-ray signals  $>15$  keV, which is indiscriminable by the 15 keV threshold. The presumed 150 keV upper bound of observation is immediately trimmed by 65%, which is catastrophic. Also learned from the calibration, the expected PE yield is halved by the energy sharing of the crosstalk. It implies the resolution of detection is also halved.

To cope with the crosstalk issue, the application of the light guides (LGs) or other types of the scintillation light modulators was proposed. We searched for the solution that reduced the CR and preserved the absolute PE yield. We expected the LG to enhance the threshold discriminability of FS detection unit while the physical modification to the whole detector is limited.

In this chapter, I first review the previous studies on LGs in 7.2. An inchoate trial with some commercially available LGs is reported in 7.3. The special design of Inverted-Conical (IC) LG inspired by the trial test and the simulation study is elaborated in 7.4. The optimization of the geometry of IC-LG is discussed in 7.5. Finally, the work is concluded



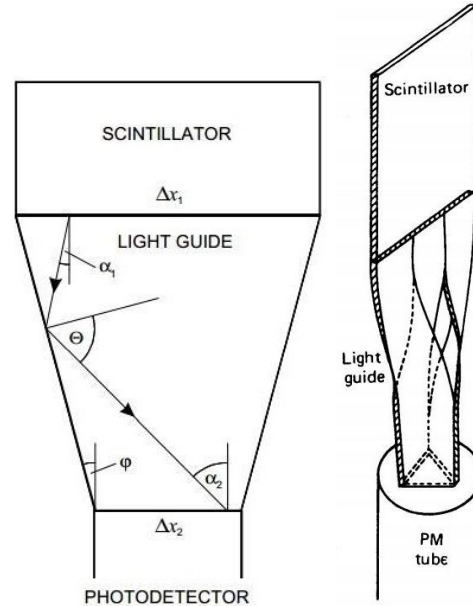
in 7.6 by the fabrication and the calibration of the sample product.



## 7.2 REVIEW ON LIGHT GUIDES

Before multi-channel photon detectors (PDs) were widely used, the LGs were commonly utilized by the scintillation detections when the scintillators and the single-channel PDs mismatched in sizes. Fig. 7.1 shows an example of the traditional LG. The PD might have the pixel size  $10^{0-2}$  cm, and the scintillator might have a comparable or larger size with a very different geometry. The LG was designed intuitively mimicking the funnel that collecting photons [1].

Figure 7.1: A typical deployment of the traditional light guide by a scintillation detector. The scintillator on top has a narrow rectangular cross section which obviously mismatches the triangular pixel of the photon detector below. One can expect most of the scintillation photons may not be detected due to the mismatch. The light guide is then designed to be a channel with the shapes of the scintillator and the pixel at two ends and is reflective inside. So the light guide may collect most of the photon by multiple scattering/reflection into the pixel.



When the scintillation photons were emitted from the scintillator, they underwent multiple reflections inside the LG and eventually arrived at the PD. In order to limit the signal reduction due to the multiple reflection, the LG were typically made with high-reflectance materials such as aluminum, or transparent materials of refractive indices greater than the surrounding, so the total reflection might occur. Despite the diverse geometries, an universal characteristic of the traditional LGs was the scintillation luminance reduced with the length of the LG (Fig. 7.2 [2](1970)).

Nowadays, multi-channel PDs are widely applied to the scintillation detectors in different fields. They may equip tightly-arranged pixel arrays of pixels size only  $10^{-1-1}$

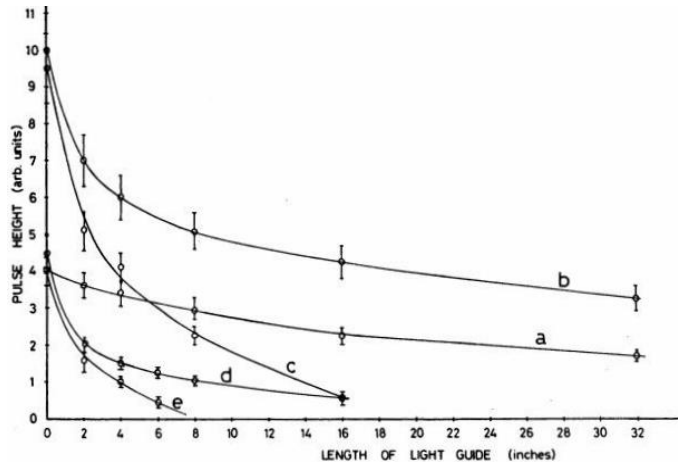


Figure 7.2: The plot of the scintillation pulse height to the length of LG. Data shown in the plot are a) total reflection type, b) total reflection type with reflective coating, c) reflective type, and focusing the scintillation light with d) specular reflector and e) diffusive reflector. It is shown despite the designs of the LGs, the signal are all reduced by factor 2–10 when the LGs extend to 10”.

mm. Reckoning for the progress, studies have proposed diverse designs of LGs to improve not just the overall luminance, but also the uniformity of multi-channel detection, signal-to-crosstalk contrast, fabrication feasibility...etc. [3](2000) suggested the scintillation imaging could be improved by replacing a one-piece bulk scintillator with a discrete arrangement of many scintillators that separated by reflective housing (Fig. 7.3). The housing was also regarded as a kind of LG therein. Readers may notice the similarity of the discrete scintillator and the scintillator array of *UBAT*.

Based on a simulation study, the paper investigated the effect of the different combinations of the parameters in Fig. 7.3-(c), e.q. the separation of the scintillator and the PMTs (t) and the extension of the LG (s). It concluded the repeating housing generally improved the result from the bulk scintillator (Fig. 7.4). It's pointed out in the paper the extended slots of the LG effectively reduced the crosstalk along the housing repeating directions

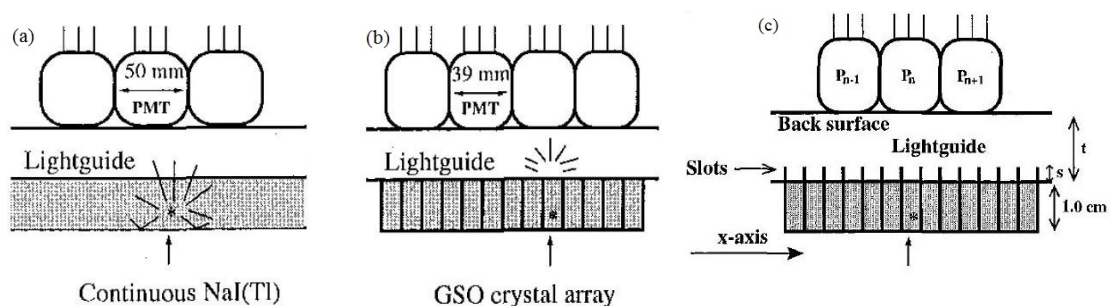


Figure 7.3: The discrete scintillators and the PMT arrays. The gray areas, the arrows point upward and the star symbols represent the scintillators, the X-ray photons and the scintillations. a) The pre-modified bulk scintillator with 50 mm wide PMT array, b) The discretized scintillator integration with reflective housing, c) The discretized scintillator integration with the reflective housing extends out from the scintillator.

## 7.2 Review on Light Guides

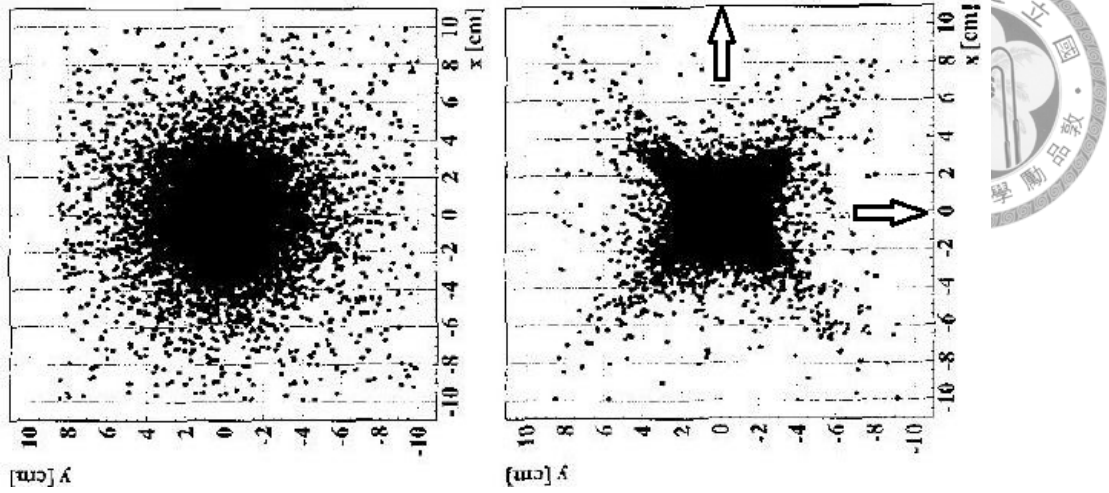
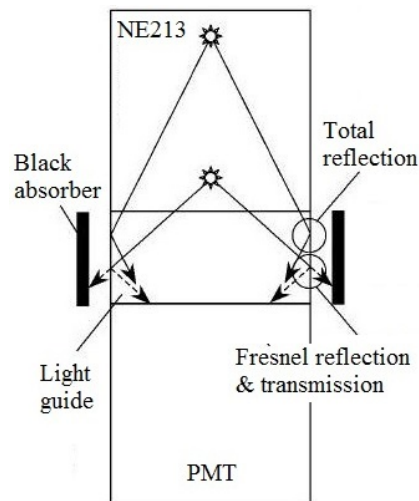


Figure 7.4: The comparison of the scintillation images of the bulk scintillator (left-handed) and the optimized discrete scintillator (right-handed). Note that the dots represent the position of the scintillation photons arrive on the FS, but the realistic image must be observed by the discretely arranged PMT array. The widths of one PMT are represented by the overlaid horizontal lines. The arrows represent the repeating directions of the LG housing.

(arrows in the figure) and resulted in the “ $\times$ ” pattern. Whoever, if the discrete arrangement of PMTs were considered, the observed images should be similar in both cases, i.e.  $\pm 4 \times \pm 4 \text{ cm}^2$  square pattern at the center.

[4](2005) proposed another approach to improve the scintillation image. Considering the distribution of the emission angle of the scintillation photon, the paper suggested the uniformity of the photon acceptance on the PD FS could be improved by reducing the emission generated closer to the PD. The idea was demonstrated by a simulation model shown in Fig. 7.5

Figure 7.5: The schematics of the partially-reflection-partially-absorption LG proposed in [4]. The LG is made of glass or Acrylic wrapped with black absorber. When the NE213 scintillator scintillates from the deeper (top) site, the photons undergo total reflections at the LG/air boundary and are regained; when it emits from the shallow site (bottom), the photons may partially transmit through the LG boundary and be absorbed by the absorber. It is suggested, if the material and the geometry of the LG is chosen properly, the illumination uniformity on the PMT FS may be enhanced.



The transparent LG made with a refractive index of the NE213 scintillator was deployed between the scintillator and the PMT. If the scintillation photons illuminated the LG/air boundary with large incident angles, the total reflection occurred so the scintillation from the deeper site of NE213 was restored. If otherwise, Fresnel transmission took place to reduce the nonuniform scintillation occurred at the shallow site.

The simulated result was presented in a two-fold compensation. It was demonstrated by the simulation the FS uniformity might be improving by thickening the LG. But it was also shown, the LG exhibited the typical thickness-signal reduction relation. The paper eventually designated a specific thickness as the optimal solution for it might enhance the uniformity while tolerably reducing the scintillation strength.

### 7.3 TEST WITH COMMERCIAL LIGHT GUIDES

The tested LGs were categorized by two groups, the mask type and the refraction type. The mask type indicated the samples were expected to reduce the crosstalk by shielding the scintillation; the refraction type indicated the samples achieving so by means of refraction or reflection. Tab. 7.1 and Tab. 7.2 list all the tested samples.

The trial test gave some hints of developing the LG for *UBAT* detection unit:

1. By comparing the thin samples 1–3 to thick ones 4–5, a LG thicker than 1 mm might result in a significant signal reduction.
2. The signal reductions of the thin mask type samples were proportional to the shielding areas.
3. By comparing samples 4 and 5, the reflective LG tunnel gave larger signal and might also suppress the CR.

The functionality and the applicability of the microlens array (MLA) had been discussed in many published studies, e.g. [5, 6, 7] (Fig. 7.6). It's reported to exhibit excellent focusing ability with customized design and fabrication. The signal might be enhanced by  $> 50\%$  in parallel with significant crosstalk reduction. More implications were drawn from the refractive type samples:

### 7.3 Test with commercial light guides

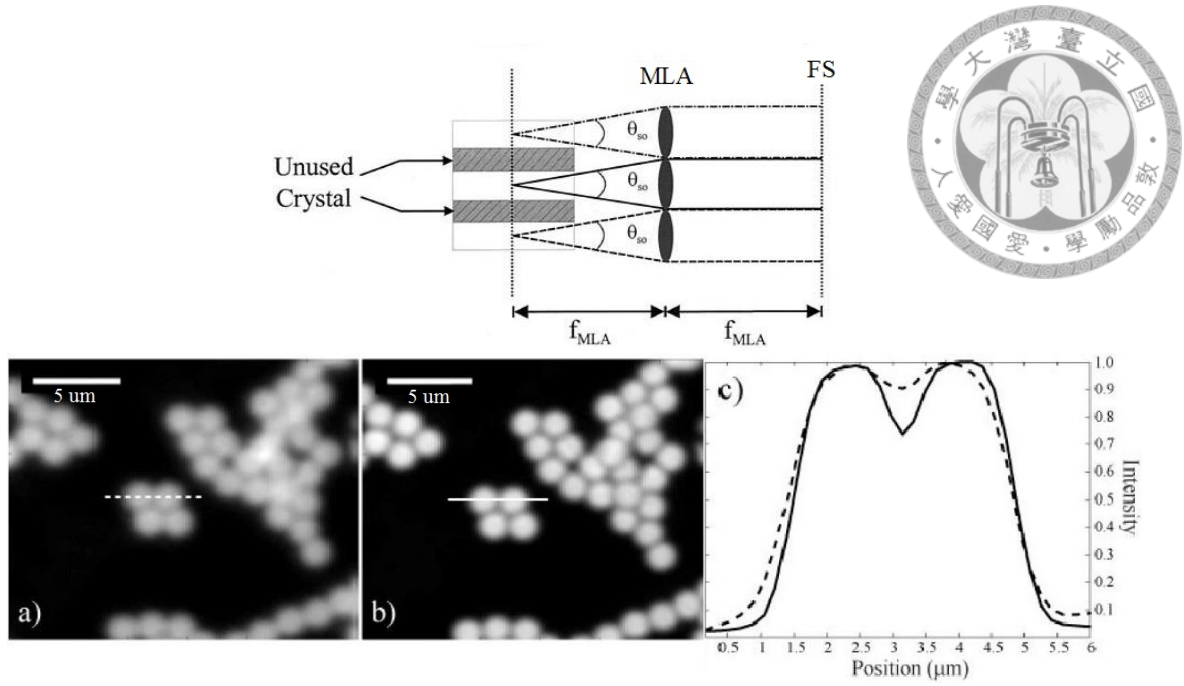


Figure 7.6: The upper panel shows an example of the usage of the microlens array (MLA). With the proper geometrical design, the MLA turns the multiple-point-like diffusive emission from the left-hand side into a parallel light. It is also noted in the figure a significant portion of the scintillator crystal can be saved. The lower three images present the result of applying MLA. The image taken are 2  $\mu m$  beads. a) w/o MLA, b) w/ MLA, c) the intensity distributions of the barred locations in (a) and (b), with the corresponding dashed/solid lines used for both cases.

4. It's indeed observed on the MLA-equipped samples of exhibiting larger signals than the mask type, sample 8 even amplified the original LG-free PE yield by 21%.
5. However, the samples appeared to be very poor to the purpose of crosstalk reduction. I supposed the consequence was due to the direct attaching of the LG and the scintillator. Unlike the illustration in Fig. 7.6 which shows the scintillation from the deep sites with small incident angles to MLA, *UBAT* crystal array was much thinner<sup>1</sup>. When being directly attached, most of the scintillation illuminated with incident angles larger than the total reflection angle from close sites to the MLA. The MLA then served as a diffuser diverting the light.
6. Obviously the mask type LGs were more endurable and cost-friendly.

<sup>1</sup>In the sense of the crystal's thickness-to-width ratio. The crystal cubes of the *UBAT* scintillator had roughly equal width and thickness.



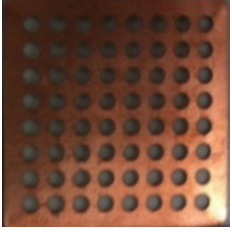
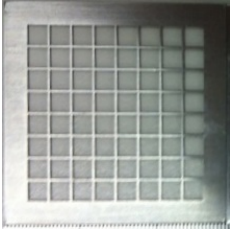
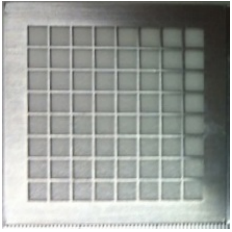


	CR	Relative PE yield	Material	Thickness	Eyelet	Photo
1	19%	54%	Copper	0.04 mm	$\Phi 1.8$ mm	
2	36%	84%	Aluminum	0.3 mm	2.65 mm	
3	36%	54%	Aluminum	0.3 mm	2.5 mm	
4	26%	20%	PVC	1.0 mm	$\Phi 2.0$ mm (blacken inside)	
5	19%	31%	PVC	1.0 mm	$\Phi 2.0$ mm (reflective inside)	

Table 7.1: The list of the mask type samples. The PE yields are normalized by which of the case without a LG, 0.72 PE/keV.



#### 7.4 Inverted-Conical Light Guide

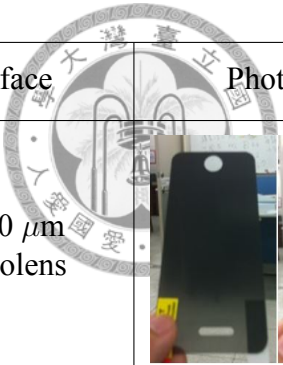
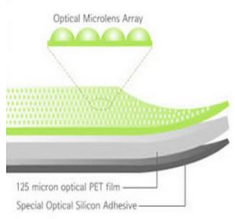
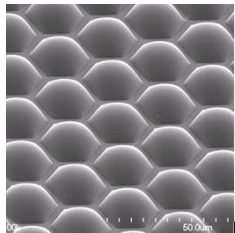
	CR	Relative PE yield	Material	Thickness	Surface	Photo
6	56%	38%	PET	100 $\mu\text{m}$	$\Phi 200 \mu\text{m}$ microlens	
7	$\sim 100\%$	81%	PET	100 $\mu\text{m}$	$\Phi 200 \mu\text{m}$ microlens	
8	$\sim 100\%$	121%	Quartz	1.0 mm	$\Phi 200 \mu\text{m}$ microlens	

Table 7.2: The list of the refraction type samples. The PE yields are normalized by which of the case without a LG, 0.72 PE/keV.

#### 7.4 INVERTED-CONICAL LIGHT GUIDE

According to the inchoate sample test, a possible solution may emerge from several features: sub-mm thickness, wide eyelets, reflective LG channels, light-focusing, and capable to contract large angle scintillations.

I propose the Inverted-Conical Light Guide (IC-LG). Fig. 7.7 illustrates the concept of IC-LG. The traditional LGs usually adopted the straight channels or the conical channels with the wider eyelets facing the scintillators. The idea was similar to the funnels collecting photons and emitting toward the PDs from the narrow eyelets. The drawback of the traditional tapering orientation was it exhibited even more serious signal reduction-thickness relation than the straight channels. The IC-LG was designed to orient the wide eyelet of the conical channel toward the MAPMT pixel and the narrow eyelet toward the YSO cube. The design gave birth to the name Inverted-Conical. I address the traditionally-oriented conical LG as the non-inverted conical LG (NIC-LG) in the following content.

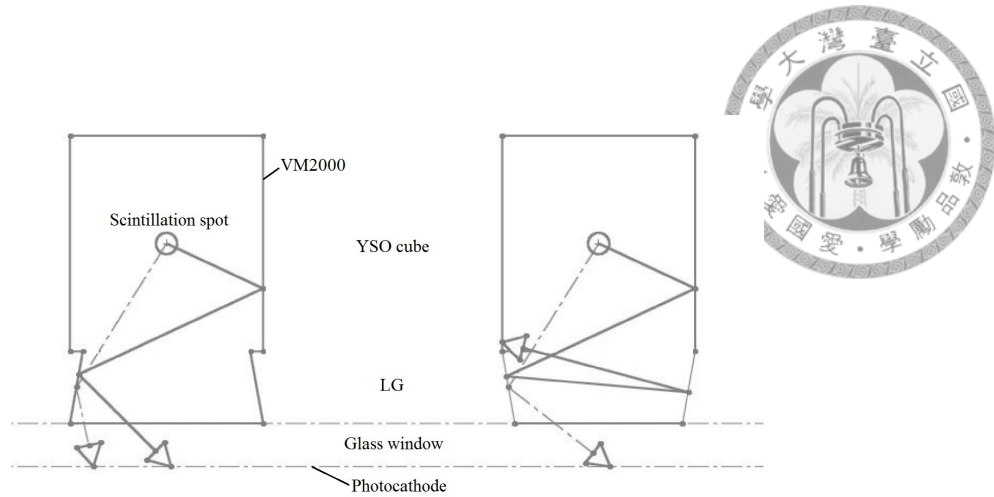


Figure 7.7: The illustration of the concept of inverted-conical. The presented setups includes two YSO cubes connected with one IC-LG channel (left-handed) and one NIC-LG channel (right-handed). The dashed and solid lines represent the small and large angle incidents, respectively.

The design of IC-LG was motivated by the simulation study in 6. The simulation proved more than 70% crosstalk was caused by the total reflection occurred at the glass window/vacuum boundary, i.e. photocathode. To reducing the total reflection, IC-LG was designed to contract large-angle incidents to be small-angle. It can be seen in Fig. 7.7, through reflection, the IC-LG was capable to redirect all the scintillations to have smaller incident angles. Base on the redirection scenario, the crosstalk photons were recovered into the collimated channel. So not only the crosstalk was reduced, it was also expected to exhibit the focusing effect in analogy to MLA. On the contrary, the NIC-LG could only enlarge the incident angles. Even worse, if the emission was fairly large-angle, NIC-LG reflected the light back into the VM2000 coating cell. Since VM2000 was highly specular and strictly obeyed the principle of reflection, the reflected photon could never leave the VM2000 cell. So the NIC-LG was also harmful to the absolute signal strength.

A simulated comparison of the situations without LG, with an IC-LG and with an NIC-LG is shown in Fig. 6.7. It is clear the emission from IC-LG exhibited smaller open angle and the illumination area on the photocathode plane. The reflections traveled into the neighboring crystals were also less. Another advantage shown in Fig. 6.7 is that IC-LG could be made much thinner than the scintillator array but was still effective. The characteristic implied the narrow eyelet was only slightly smaller than the wide eyelet



## 7.5 Design optimization

so the LG could control the shielding area and signal loss. It was also important to the overall design of *UBAT*, since any non-trivial geometrical change, especially to the FS, could significantly affect the prefixed design and performance of the coded-mask aperture camera.



## 7.5 DESIGN OPTIMIZATION

I constructed the IC-LG in the simulation package of *UBAT* inserted it between the scintillator array and MAPMT. The eyelet channels were all filled with optical couplant. Considering the realistic fabrication feasibility, the material condition was assumed to be Aluminum with fine CNC machining and polishing. I set the specularity same as VM2000 ( $\cos\alpha = 0.97$ ) and implemented the reflectance in Fig. 7.8 [8, 9].

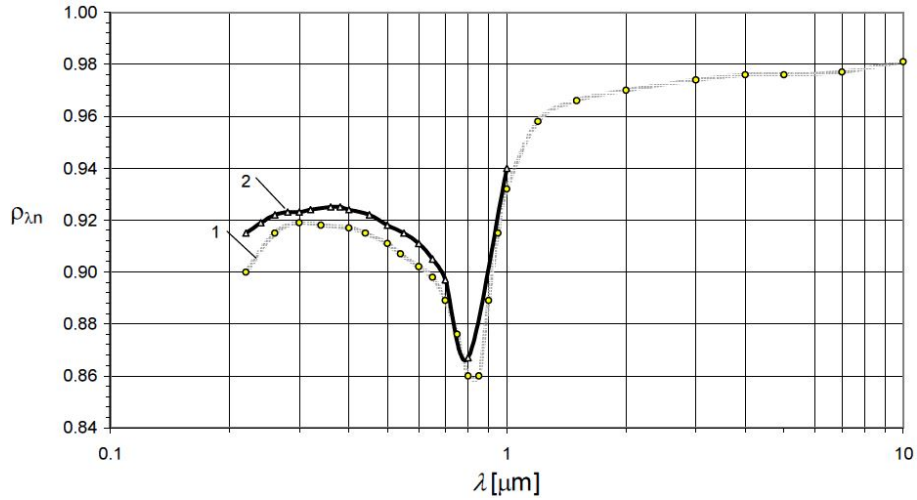


Figure 7.8: The normal-incident reflectance spectrum of polished Aluminum at  $T=295\text{K}$ . The faded line represents the data taken from [8], the solid line represents the data presented in [9]. The value utilized in the simulation was the solid line.

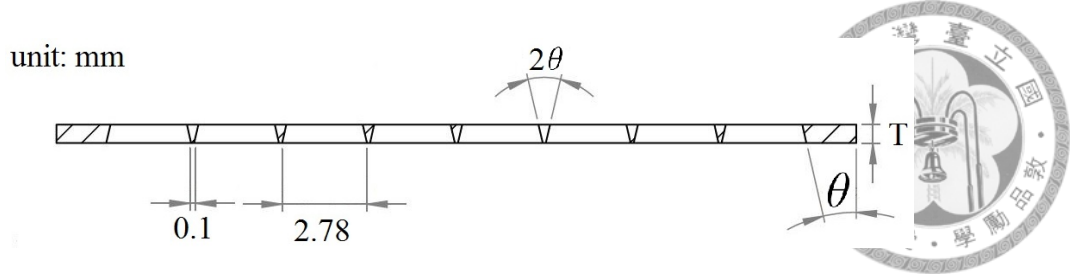


Figure 7.9: The cross section view of the IC-LG. The parameters to be optimized are the thickness (T) and the conical angle ( $\theta$ ). The upper side in this figure is the scintillator, the lower side is MAPMT. The gapping at the MAPMT side is 0.1 mm, so the width of the wide eyelets is 2.78 mm.

I optimized IC-LG in two parameters, the thickness (T) and the conical angle ( $\theta$ ), Fig. 7.9 is the cross section view of the model. The 100  $\mu\text{m}$  grid gapping between the wide eyelets was left for practical engineering. So the width of the wide eyelet was

$$2.88 \text{ (pixel size)} - \frac{0.1}{2} \times 2 \text{ (both side)} = 2.78 \text{ mm} \quad (7.1)$$

And the width of the narrow eyelet could be derived by

$$2.78 - 2T \tan \theta \quad (7.2)$$

Different combinations of T and  $\theta$  were simulated in the ranges 0.6 mm–1.5 mm and  $-5^\circ$ – $20^\circ$ , negative angles represented the NIC orientation. In addition to CR and the signal yield in the collimated channel, Crosstalk Index (CI) was also used as the indicator of optimization.

$$CI \equiv \frac{\Sigma(\text{channel separation} \times \text{local signal yield})}{(\Sigma \text{channel separation}) \times \text{collimated channel signal yield}} \quad (7.3)$$

Eqn. 7.3 summed over all the channels in the same row and column of the collimated channel. For example, ch. 27 was the collimated channel, the equation summed up ch. 4, 11, 20, 36, 43, 52 and ch. 24, 25, 26, 28, 29, 30, 31. The corresponding channel separations were 1 for ch. 20, 26, 28, 36; 2 for ch. 11, 25, 29, 43; 3 for ch. 4, 24, 30, 52; 4 for ch. 59. CI was regarded as the weighted indicator of the overall condition of the crosstalk among all channels.

### 7.5 Design optimization

Fig. 7.10 presents the optimization of the crosstalk to  $\theta$ . When  $\theta < 0^\circ$ , CR was enlarged compared to which when  $\theta > 0^\circ$ . The result coincided with the expectation. IC-LG could reduce the crosstalk while NIC-LG might enlarge it. CR and CI posed similar trends and minimums appeared at  $\theta = 13.50^\circ$  and  $\theta = 15.67^\circ$ , respectively. The result could be interpreted as the steeper angle suppressed more crosstalk, when the crosstalk in the further channels was taken into consideration, a larger angle was favored. Nevertheless, the  $\sim 2^\circ$  difference was actually trivial for the minimal regions were about  $4^\circ$  across.

Fig. 7.11 presents the optimization of the signal yield. The IC-LG enhanced the signal yield by  $\leq 25\%$  when  $T < 12$  mm. The signal yield decreased by  $\sim 3\%$  for every 0.1 mm increase in  $T$ . It was also demonstrated in the simulation NIC-LG suppressed the signal yield and the suppression was severer with steeper NIC angle. The optimal angle of 108.9% signal yield appeared at  $9.67^\circ$ . The result indicated IC-LG had the capability of focusing the photons and enhancing the signal yield identical to MLA.

Because the primary motivation of the LG study was the crosstalk reduction,  $(\theta, T) = (13^\circ, 0.6 \text{ mm})$  was regarded as the optical solution, for it gave the least CR while also enhanced the signal yield. According to the simulation, the optimized IC-LG would enhance the signal yield by 7.2% and reduce CR to 15.8%, i.e. 45% CR reduction from the calibrated CR of the detection unit.

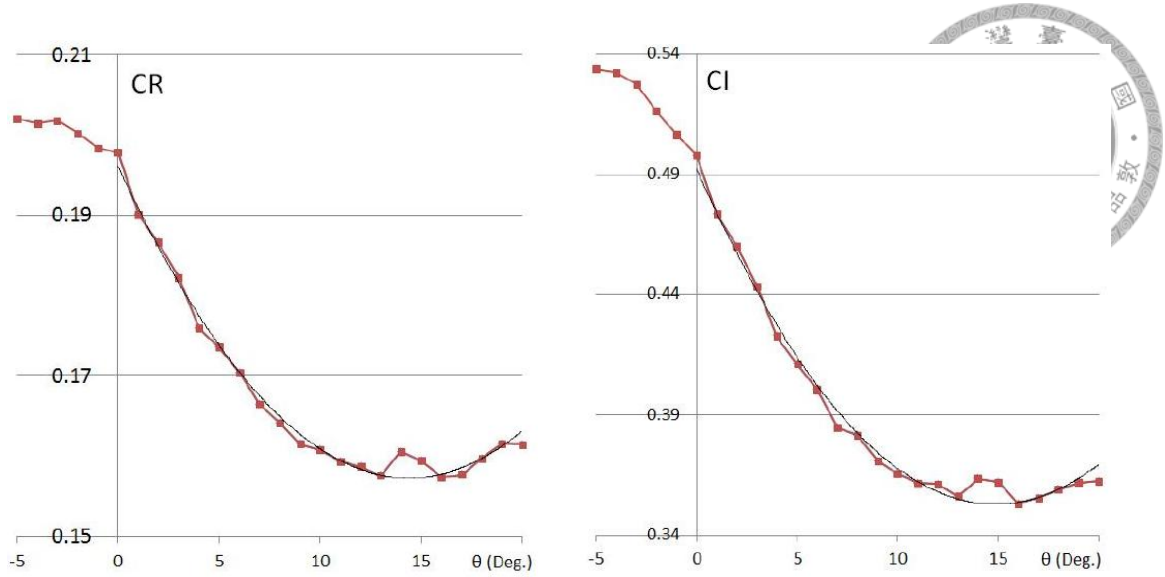


Figure 7.10: The simulated crosstalk versus the conical angle  $\theta$  at  $T = 0.8$  mm. The right- and left-handed panels are the CR and CI, respectively. The overlaid fittings are the 2<sup>nd</sup>-order polynomials. The minimal points of the fitters are at  $13.50^\circ$  and  $16.57^\circ$  for CR and CI, respectively. The NIC-LG is also shown in the figures as the negative angles.

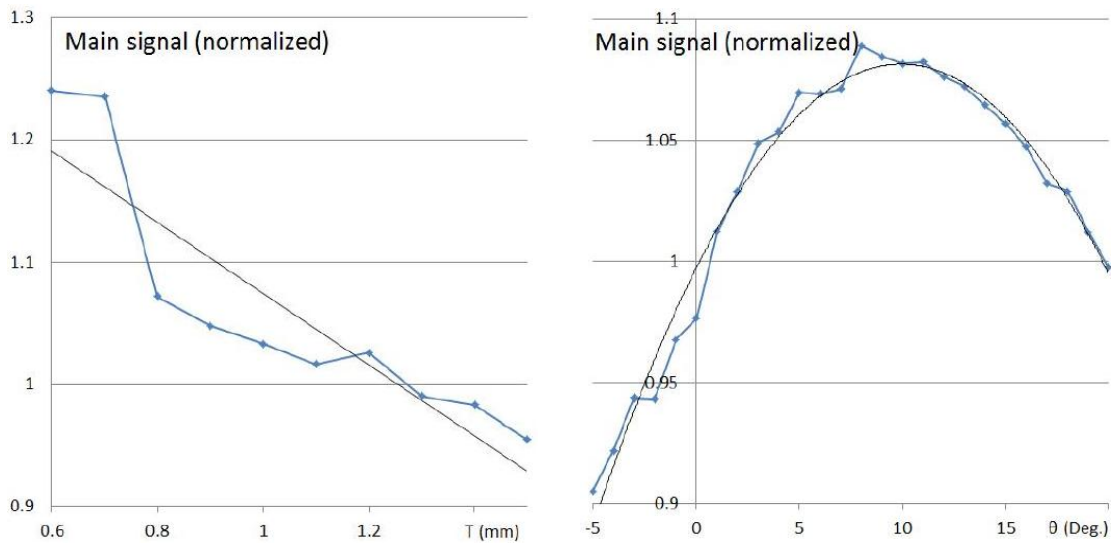


Figure 7.11: The simulated signal yield versus the thickness  $T$  (left panel) and conical angle  $\theta$  (right panel),  $\theta = 13^\circ$  and  $T = 0.8$  mm were assumed in the figures, respectively. The overlaid fittings are the 1<sup>st</sup>- and 2<sup>nd</sup>-order polynomials. The maximal point of the signal-to- $\theta$  fitter is at  $9.67^\circ$  which gives 8.9% signal enhancement. The NIC-LG is also shown in the figures as the negative angles. The signal yield was normalized by which before applying a LG.

## 7.6 Sample test

### 7.6 SAMPLE TEST

Fig. 7.12 presents the photos and the schematics of the sample IC-LG. The sample was made of 6061 Aluminum alloy through CNC machining with  $< 1 \mu\text{m}$  position tolerance then polished through chemical anodic brightening. The fabrication was cost -friendly yet the end product had geometric accuracy  $\sim 0.5 \mu\text{m}$  and the surface roughness  $< 100 \text{ nm}$ . The perimetric frame was designed to support the delicate grid-like LG. The end product was as mechanically durable as the scintillator array and the MAPMT.

The signal comparison of LG-free, IC-LG and NIC-LG cases is presented in Fig. 7.13. Before applying the LG, CR was  $0.293 \pm 0.024$ . The sample IC-LG reduced  $38.86 \pm 3.22\%$  crosstalk but acquired  $6.376 \pm 0.053\%$  PE yield reduction. The resulting CR with IC-LG was  $0.195 \pm 0.016$ . As a comparison, the sample was also inserted under the NIC orientation, i.e.  $180^\circ$  flipped. The NIC orientation gave CR  $0.244 \pm 0.020$  and  $11.47 \pm 0.95\%$  PE yield cutback. To understand Fig. 7.13, the LG-free detection unit observed the largest signal, IC-LG second, and NIC-LG the last in both the collimated and the alongside channels. However, IC-LG exhibited the collimated signal peak close to the LG-free condition but the alongside signal peak close to the NIC-LG condition. The net consequence was an amelioration of reducing CR from 0.29 to 0.20.

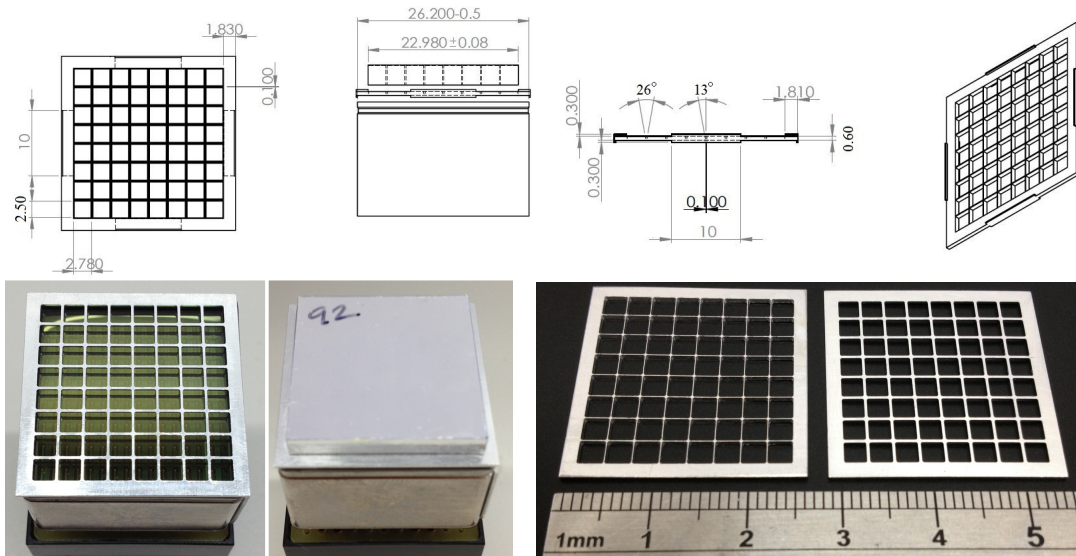


Figure 7.12: The schematics and the photos of the sample IC-LG and its assembly with the scintillator array and MAPMT.

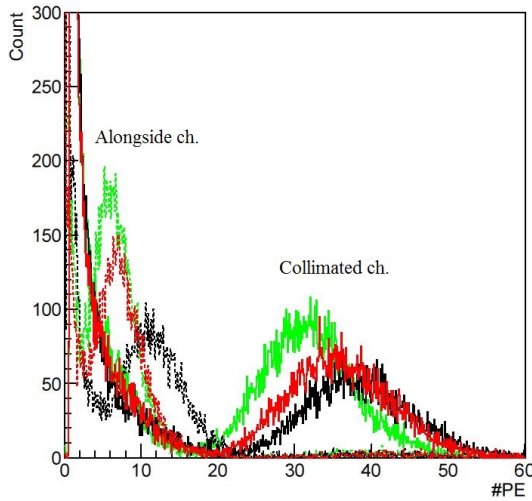


Figure 7.13: The signal histograms of the cases LG-free (black), IC-LG (red) and NIC-LG (green). The signal observed in the collimated and alongside channels are represented by the solid and the dashed lines, respectively. The calibration source was  $\text{Am}^{241}$ .

Before the amelioration, the alongside and the diagonal CRs were 29% and 8%. With the aid of IC-LG, CRs became 20% and  $< 2\%$  in the alongside and diagonal channels, respectively. The simulated coded mask images are shown in Fig. 7.14. I also repeated the energy calibration with IC-LG, all the procedure was identical to 5.2. The result is shown in Fig. 7.15. With IC-LG, *UBAT* FS detection unit had linear signal yield 0.69 PE/keV.

## 7.6 Sample test

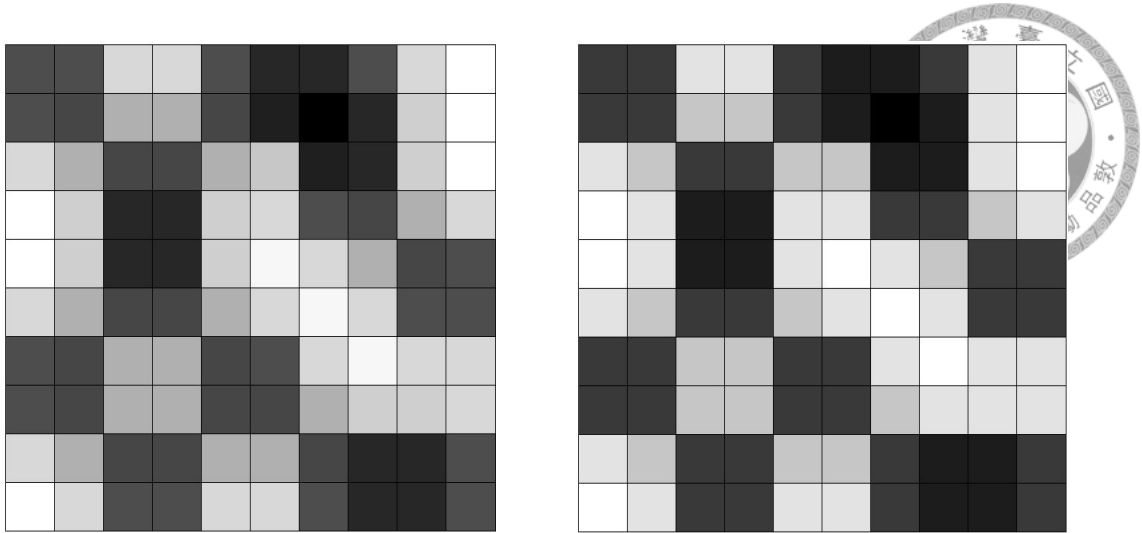


Figure 7.14: The comparison of the simulated scintillation detections of the coded mask image before (left-handed) and after (right-handed) the amelioration with IC-LG. Both figures are normalized by the channels of the highest energy and equally scaled in the gray-scale.

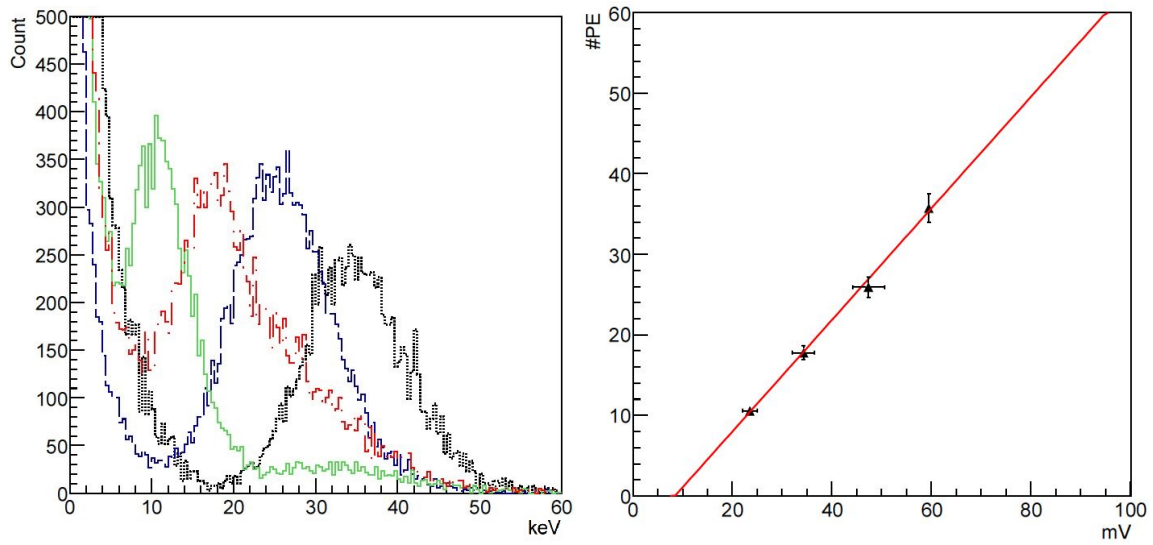


Figure 7.15: left: The IC-LG-ameliorated signal histograms of, peaks from right to left,  $\text{Am}^{241}$ , Tb, Ba and Ag. right: The peak #PEs versus the corresponding X-ray energies. The linear fit shows the slope 0.69 PE/keV. The error bars were taken as  $K_{\alpha}-K_{\beta}$ .



## Bibliography

- [1] Spieler, H. 1999, *Interduction to Radiation Detector and Electronics*, LBNL
- [2] Kilvington, et al. 1970, *Nucl. Inst. and Meth. A*, 80, 177
- [3] Sruti, S., et al. 2000, *textitNucl. Sci., IEEE Trans.*, 47-3, 1030
- [4] Harano, H, et al. 2005, *textitNucl. Sci., IEEE Trans.*, 52-6, 3147
- [5] Brewer, C. D., et al. 2002, *Appl. Opt.*, 41-21, 4411
- [6] Wei, M.-K., et al. 2004, *Opt. Expr.*, 12-23, 5777
- [7] Orth, A., et al. 2012, *Opt. Expr.*, 20-12, 2012
- [8] Latyev, L. N.-P., et al. 1974, *Izlu. svoj. tver. mate.*, Energia, 306
- [9] Bartl, M., et al. 2004, *Meas. Sci. Rev.*, 4-3, 31



## *BIBLIOGRAPHY*





## CHAPTER 8

# CONCLUSION

*UFFO* is design to be the first GRB observatory capable of responding to the UV–visibal signals of GRBs within one minute; *UBAT* is the primary  $\gamma$ –/X-ray trigger telescope in *UFFO* responsible for delivering the event directions. To achieve the rapid direction determination, *UBAT* is designed to operate under the coded mask aperture camera scheme. So it's crucial the focal surface detection units can confidentially discriminate the coded mask pattern.

In this thesis, I firstly demonstrated the energy and the image crosstalk calibrations of the *UBAT* focal surface detection unit. The signal yield was 0.72 PE/keV. A serious crosstalk issue of  $CR \sim 29\%$  was identified. A simulation of the detection unit was then constructed to resolve the issue. Through the simulation study, I pointed out more the 70% of the crosstalk was caused by the total reflections occurred at the photocathode. After identifying the source of the crosstalk, I proposed the Inverted-Conical light guide which utilized the inverted orientation of the traditional focusing LG as a possible solution. The Inverted-Conical light guide was optimized in the simulation and fabricated. The end product reduced the crosstalk and the signal yield by 39% and 6%, which resulted in the reduction of CR from 29% to 20%.

*UFFO*-pathfinder is scheduled to launched in the summer of 2014. Due to the schedule of the R&D phase of *UFFO*, Inverted-Conical light guide was not implemented in *UFFO*-p before it was transported to the launch site. However, I'm still looking forward to the future utilization of Inverted-Conical light guide to *UFFO*-100.